Microanalyses of Ferroelectric Properties of $BaTiO_3$

Xiao Xia Liu

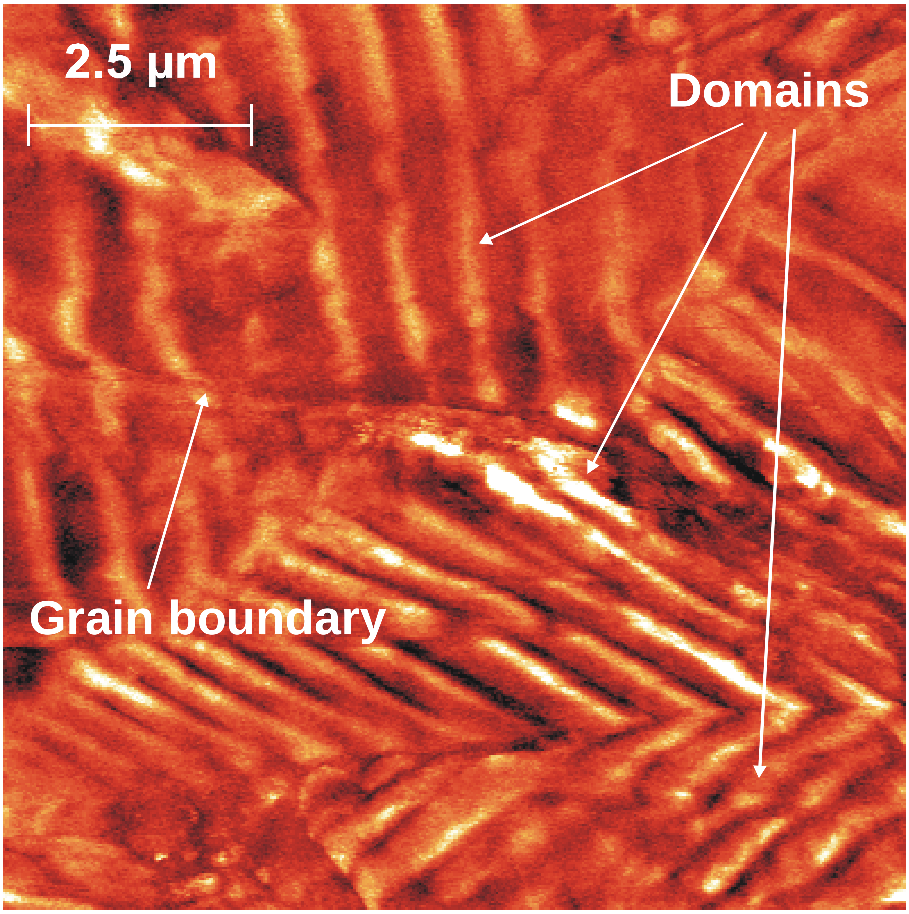

Microanalyses of Ferroelectric Properties of $BaTiO_3$

Im Fachbereich Elektrotechnik und Informationstechnik der
Bergischen Universität-Gesamthochschule Wuppertal

Zur Erlangen des akademischen Grades eines

Doktor-Ingenieurs

eingereichte Dissertation

von

M.Sc. Eng. Xiao Xia Liu
aus
Chengdu, Sichuan
Volksrepublik China

Referent: Prof. Dr. rer. nat. Ludwig Josef Balk
Korreferenten: Prof. Dr.-Ing. Wolfgang Mathis und Prof. Qingrui Yin

Tag der mündlichen Prüfung: 27. 06. 2001

Acknowledgements

I would like to express my gratitude to Professor Dr. rer. nat. Ludwig Josef Balk for the opportunity to carry out this work in Lehrstuhl für Elektronik, Bergische Universität Gesamthochschule Wuppertal under his supervision. His continual interesting in my work, his helpful discussions and encouragement, and his strict scientific point of view have substantially contributed to the success of this work. Through his kindly help, I have obtained the chance to cooperate and discuss with many other scientists in the areas of ferroelectric materials and acoustic near-field imaging. I am very grateful for all the help which he has given me during my stay in his Lehrstuhl.

I like to thank Prof. Dr.-Ing. Wolfgang Mathis and Prof. Qingrui Yin for co-examining this work and much helpful advice. I am also very grateful to Prof. emeritus Dr. Klaus Dransfeld, Fachbereich Physik, Universität Konstanz, who has read all the work carefully and gave me much valuable advice.

The fruitful cooperation between the Lehrstuhl für Elektronik, BUGH Wuppertal and Lab. of function ceramics, Shanghai Institute of Ceramics helps me a great deal to begin present work and I am very grateful for all the help which Prof. Yin has given me.

I would like specially to thank Prof. Dr.-Ing. Volkert Hansen, Lehrstuhl für theoretische Elektrotechnik, BUGH Wuppertal, for the theoretical support of the dissertation.

For the help from Dr. Ralf Heiderhoff, who has helped me to complete the whole work, I would express my special thanks.

Many thanks also to Mrs. Mechthild Knippschild, who has continually help me in all the respects.

I am also very grateful to my dear colleagues from the Lehrstuhl für Elektronik for the active cooperation and support.

This work is partly aided from DFG (Deutsche Forschungsgemeinschaft) project ‘Nanocharakterisierung ferroelektrischer Domänen mittels Nahfeld-akustischer-Rastermikroskopien’. I am grateful for this financial aid.

The encouragement and help from my family and, especially, from my wife Zhang Yuan, have certainly contributed a great deal to the success of this work and I would like to express my thanks wholeheartedly.

Microanalyses of ferroelectric properties of $BaTiO_3$

Abbreviations, variables, symbols and constants

AE	Helmholtz free energy
a^{i+}, a^{i-}	Amplitude of +z and -z transmitted longitudinal acoustic wave at ith medium (i=1, 2, 3, which means near-field in the sample, area in the sample but outside the near-field, and in the PZT transducer)
$\vec{B}, B_i$	Magnetic flux density and its i´th component (i=1,2, 3 or x, y, z)
c_P^{PZT} , c_P	Stiffened stiffness constant of PZT transducer and BaTiO$_3$ single crystal
$\overleftrightarrow{c}, c_{I,J}$	Elastic stiffness tensor, and its component with simplified suffix (I=1 to 6 and J=1 to 6)
d	Depth of near-field
$\overleftrightarrow{d}$, $d_{i,J}$	Piezoelectric strain constant tensor, and its component with simplified suffix (i=1,2, 3 or x, y, z and J=1 to 6)
d_w, $d_w^{\prime}$	The domain width of fine and coarse grains in BaTiO$_3$ ceramics
D_1	Sample thickness
D_2	Thickness of PZT transducer
$\vec{D}$, D, D_i	Electric displacement, its magnitude, and its i´th component (i=1,2, 3 or x, y, z)
e_{z3}^{PZT}	Piezoelectric stress constant of PZT in z-direction.
$\overleftrightarrow{e}$, $e_{i,J}$	Piezoelectric stress constant tensor, and the tensor component with simplified suffix (i=1,2, 3 or x, y, z and J=1 to 6)
$\vec{E}$, E, E_i	Electric field, its magnitude, and its i´th component (i=1,2, 3 or x, y, z)
E_s	Source electric field in near-field
$\vec{F}$	Body force
g	Grain size in ceramics
Gb	Gibbs energy
Gb_1	Elastic Gibbs energy
Gb_2	Electric Gibbs energy
$\overleftrightarrow{G}$, G_i	Body torque and its i´th component,(i=1,2, 3 or x, y, z)
$\vec{H}, H_i$	Magnetic field and its i´th component,(i=1,2, 3 or x, y, z)
HE	Enthalpy

HE_1	Elastic enthalpy
HE_2	Electric enthalpy
$\vec{J}_c$	Conducting current
$\vec{J}_s$	Source currents
k	Stiffened acoustic longitudinal wave number in $BaTiO_3$ material
k_3	Stiffened acoustic longitudinal wave number in PZT transducer
$\vec{P}$, P , P_i	Polarization vector, its magnitude, and its i´th component, (*i*=1,2, 3 or x, y, z)
Q	Heat
Q_{es}	Electrostrictive coefficient
R	Reflection constant at the boundary between the transducer and the back electrode
$\overleftrightarrow{s}$, $s_{I,J}$	Elastic compliance tensor, and its component with simplified suffix (*I*=1 to 6 and J=1 to 6)
S	Entropy
T	Temperature
$\vec{u}(\vec{r},\mathrm{t})$, U_i	Displacement field of a particle and its i´th components (*i*=1,2, 3 or x, y, z)
U	Internal energy
$\vec{v}$, v_i	Velocity of a particle and its i´th components (*i*=1,2, 3 or x, y, z)
V_{output}	Output signal of the PZT transducer in near-field acoustic microscopy system
W_E	Electric work
W_m	Elastic work
$\overleftrightarrow{x}$, x_{ij} , x_I	Strain tensor, its component, and component with simplified suffix (*I*=1 to 6)
$\overleftrightarrow{X}$, X_{ij} , X_I	Stress tensor, its component, and component with simplified suffix (*I*=1 to 6)
Z_0	Characteristic resistance of stiffened acoustic longitudinal wave in $BaTiO_3$ single crystal with a monodomain
Z_3	Characteristic resistance of stiffened acoustic longitudinal wave in PZT transducer
β	Spatial periodical constant in z direction for Bessel´s function.
β_a	The ratio of acoustic characteristic resistances in the sample and in PZT

	transducer ($\frac{Z_0}{Z_3}$).
$\overleftrightarrow{\varepsilon}$, $\varepsilon_{i,j}$	Permitivity tensor, and its component (*i*=1,2, 3 or x, y, z)
ε_0	Permitivity in vacuum (8.85418*10^{-12} As/Vm)
ε_r, ε_{ri}	Relative permittivity and relative permittivity of i´th layer of multilayer devices
ε_{zz}^{PZT}	Permittivity of PZT transducer in z-direction
η_E	Backscattering coefficient
μ_0	Magnetic permeability in vacuum
ρ	Density of a material (Kg/m^3)
σ	Noise of an equipment
ω	Angular frequency of the system
EAI	Electron Acoustic Image
SEM	Scanning Electron Microscopy
SEAM	Scanning Electron Acoustic Microscopy
SEI	Secondary Electron Image
SNAM	Scanning Near-field Acoustic Microscopy based on SPM
SIAM	Scanning Ion Acoustic Microscopy
SPM	Scanning Probe Microscopy
SPAM	Scanning Photo Acoustic Microscopy
TEM	Transmission Electron Microscopy

1 Introduction

1.1 Possible use of $BaTiO_3$ as a high density memory material

As early as 1950s when the demand for high-capacity computer memories came, ferroelectric materials were intensively studied in the world, as they seemed to be prime candidates of new materials for binary memories [1~3]. Later in the period of 1965 to 1975, tremendous efforts were taken to develop ferroelectric-semiconductor memories by the use of a thin film of semiconductors deposited on a bulk ferroelectric single crystal or ceramics materials. Though the basic concept was valid, the instability of semiconductor thin films at that time did not permit a viable memory to be built. In recent years, ferroelectric materials have attracted much more attention because of the combination of their unique properties of spontaneous polarization, i.e. the so-called ferroelectric domains of the materials, to CMOS techniques of microelectronic industry [4, 5]. This combination has led to a large variety of new devices in computer technology and transducing devices in electromechanic, electrochemic, electrooptic, and acoustooptic fields.

Among all the ferroelectrics used during the development of modern memory devices, Barium titanate ($BaTiO_3$) material system is one of the most interesting ferroelectric material systems up to now [2]. $BaTiO_3$ single crystal has ferroelectric structures which are far simpler than those of any other ferroelectrics known and thus provides a good base for the research and understanding of whole ferroelectric phenomena. It is chemically and mechanically stable and has a Curie temperature at about 120°C. Its hysteresis loop has rather sharp corners and a good rectangular appearance. The value of its coercive field, measured at room temperature, varies from a minimum of 5 kV/m to a maximum of 200 kV/m. The dielectric constant in the direction of polarization ($\varepsilon_{rzz} \approx 160$) is much smaller than that perpendicular to it ($\varepsilon_{rxx} \approx 2920$) and they exhibit pronounced anomalies at the transitions from tetragonal to orthorhombic and from orthorhombic to rhombohedral states. $BaTiO_3$ polycrystalline materials, the so-called ceramics, and their modifications offer even more applications in various fields of engineering. It is easy to produce a hard $BaTiO_3$ ceramics body by standard sintering process and its body form can also be easily modified according to the industry applications. The polarization direction of ceramics can be chosen as required. $BaTiO_3$ thin films, and other perovskite-type films such as Lead Zirconate Titanate (PZT), Strontium Bismuth Titanate film (SBT) and so on, are intensively studied recently due to the integration of these kind of films to CMOS circuits to produce various novel devices [4, 5]. In general,

$BaTiO_3$ and other perovskite type ferroelectric materials provide today an intensively active research and application field. Even though its technical and commercial importance is substantial, many breakthrough applications may still lie ahead of us.

1.2 Present research on ferroelectric domains

Although present applications of ferroelectric materials in the modern microelectronic industry provide a great prospect and almost unlimited opportunities, there is much work to be done [5~13]. Under macroscopic view, problems associated with application of $BaTiO_3$ and other current ferroelectrics are that their properties are often controlled by the contributions from the so-called extrinsic effects which are responsible for polarization fatigue, aging, frequency and field dependence of piezoelectric, elastic and dielectric properties. These contributions are generally described as domain-wall effects [11~13]. The theoretical treatment and experimental study on all these contributions present us a big challenge since long time. Although substantial insights into the nature of ferroelectrics have been achieved, all the theoretical models, most of which are phenomenological in nature, and experiment results provide only a global or macroscopic view of the ferroelectrics. The present application of ferroelectric materials combined with CMOS integrated circuits requires that such problems be further studied under micrometer or even in difficult cases in nanometer range. To keep pace with this new technological trend, non-destructive techniques to investigate the ferroelectric domains under such spatial resolution must be developed. Whereas the resolution of conventional optical microscopy is limited by the diffraction limit, a number of non-destructive methods have been developed to study ferroelectric domains [14~17]. Scanning electron microscopy (SEM) [14] is non-destructive but has a disadvantage that contrast and resolution are dependent on time. In combination with acoustics, a non-destructive technique with resolution and contrast independent of time, scanning electron acoustic microscopy (SEAM), is used to visualize ferroelectric domains [15, 16]. Unfortunately, SEAM has only a resolution down to several micrometers due to the interaction area formed by primary electrons injected into the sample. Although transmission electron microscopy (TEM) [17] has a resolution down to nanometer range, this technique needs a difficult sample preparation. Whether the preparation process would affect ferroelectric domains is not clear. With the invention of scanning probe microscopy (SPM) [18], non-destructive methods to image ferroelectric domains with submicrometer or nanometer spatial resolutions have emerged recently [19~31]. F. Saurenbach, et. al. [19] imaged the ferroelectric domain of GMO ($Gd_2(MoO_4)_3$) material system by the use of SPM in non-contact topography mode. R. Lüthi et. al. [20] presented ferroelectric contrast of GASH ($C(NH_2)_3Al(SO_4)_2\cdot 6H_2O$) and M.-K. Bae et. al. [21] of TGS ($(NH_2CH_2COOH)_3\cdot H_2SO_4$) materials by the use of contact topography mode of SPM respectively. By applying an ac voltage and measuring of the first harmonic signal from topography feedback, K. Franke et. al. [22] introduced imaging and modification of domains in PZT film. For $BaTiO_3$ material system, S.-I. Hamazaki et. al. [23] presented results by the use of SPM contact topography mode on ferroelectric $BaTiO_3$ single crystal and suggested that the topography image of SPM is also ferroelectric domain image. L. M. Eng et. al. [24] also showed results of domain contrast of ferroelectric $BaTiO_3$ single crystal by the use of the non-contact mode as well as the friction mode of SPM. Thereafter, there were mainly two kinds of modes of SPM which were used frequently to image ferroelectric domains of $BaTiO_3$ material system in the literatures. One is the so-called topography mode [23] and the other piezoresponse mode [19, 22]. To study the contrast mechanism of both methods, A. Gruverman et. al. [25] explained the contrast of topography mode of SPM on $BaTiO_3$ revealed the difference of a-c domain boundary and piezoelectric response mode imaged the c-c domain boundary.

Based on the principle of topography mode of SPM, some literatures [26-29] presented the comparison of domain contrast from topography mode of SPM with the results from optical microscopy, SEM, and surface potential microscopy based on SPM respectively. As the topography mode of SPM requires an absolutely flat sample surface, this mode is impossible to apply to image ferroelectric domains of samples with rough surface such as ceramics or electronic devices non-destructively. A systematic analysis of contrast mechanism of this mode and the contrast comparison to other techniques are also difficult.

At the base of the piezoelectric response mode of SPM, U. Rabe et. al. studied ferroelectric domains from PZT ceramics [30]. L. Eng. et. al. presented the domain imaging on PZT and $BaTiO_3$ ceramics, writing and switching on a bulk $BaTiO_3$ single crystal [31]. C. Harnagea studied the domain imaging and switching on $BaBi_4Ti_4O_{15}$ thin films [32]. In order to analyze the ferroelectric domains by SPM quantitatively, C. Durkan et. al. presented a theoretical model for the calculation of the electric field in the system of the piezoelectric response mode of SPM [33]. Although the work [31] has made a comparison of the results by piezoelectric response mode of SPM on $BaTiO_3$ ceramics with results by chemical etching method, the chemical etching method is actually a destructive method and an explanation of the contrast difference between these two methods would be difficult. Meanwhile, although the theoretical model [33] for the piezoelectric response mode of SPM on ferroelectric films has been introduced, from our point of view, the theoretical treatment of the model can not be the right theoretical analytic method. Neither can the model be used systematically to analyze electric field distributions in different samples, such as bulk materials, thin films or multilayered films. Electric and mechanic field distributions and the energy exchange between them in the system of piezoelectric response mode of SPM remain unsolved up to today.

1.3 Aim of present work

In this work, a new set-up, Scanning near-field Acoustic Microscopy based on SPM (SNAM), is developed to image ferroelectric domains of both single crystal and ceramics of $BaTiO_3$ material system [34, 35, 36]. The results of ceramics are compared to the results at identical areas of the same ceramics by another established non-destructive acoustic technique, Scanning Electron Acoustic Microscopy (SEAM) [15, 16, 37]. Based on the classic phenomenological theory, a theoretical model for both the SNAM set-up developed and the SEAM on ferroelectric $BaTiO_3$ materials is grounded. The ferroelectric domains are analyzed quantitatively according to the model established. Different modes based on SPM are also compared. The ferroelectric domains of $BaTiO_3$ ceramics are imaged temporally, thermally dynamically, and electrically dynamically [37].

As shown at the end of this work, both SEAM and SNAM techniques are complementary tools for the future research and application of ferroelectric materials and devices. The theoretical and experimental methods presented can further be applied to other near-field acoustic microscopy techniques and other ferroelectric materials.

1.4 Structure

This work is mainly divided into the following chapters: Chapter 2 will mention briefly main theories on electric and ferroelectric properties of $BaTiO_3$ crystal and ceramics. The typical methods and new works to image ferroelectric domains are also discussed. From the discussion, two near-field techniques, SEAM and SNAM, are chosen as examples for the further discussion. Chapter 3 is concentrated to electric and mechanic coupling of near-field acoustic microscopy and a $BaTiO_3$ single crystal with a monodomain structure is chosen as an example to simplify the discussion. The contrast mechanism for both near-field acoustic microscopy techniques is analyzed. Chapter 4 treats the physical background, signal generation, contrast mechanism, and experiment set-up of SEAM on $BaTiO_3$ material system. Chapter 5 discusses the physical background, signal generation, contrast mechanism, and experiment set-up of SNAM developed in this work on $BaTiO_3$ material system. Then the comparison of the contrast of the developed system to that of another mode of SPM, the so-called piezoelectric response mode, is studied. Finally the domain structures of $BaTiO_3$ ceramics are studied dynamically. Chapter 6 discusses the experimental details in this work and Chapter 7 presents some typical experiment results. Chapter 8 discusses the complementary study by both near-field techniques on identical areas and presents an explanation for the study at the base of the theoretical model grounded. A small summary will be given in Chapter 9 and future prospects will be briefly mentioned in Chapter 10. All theoretical calculations will be presented in the Appendix in detail.

2 Theoretic description of electric and ferroelectric properties of $BaTiO_3$

2.1 Definition of ferroelectric domains

Ferroelectric domains are referred to as volumes of spontaneous polarization in ferroelectrics whose polarization can be changed by an electric field [1, 3]. The boundaries separating domains are referred as domain walls. If a ferroelectric crystal is brought to the ferroelectric state from paraelectric phase by decreasing temperature, the electrostatic interaction on the surface and the inhomogeneity of stress in the materials affect the internal energy and thus result in ferroelectric domains in ferroelectric phase. As for the polycrystal materials, the domain equilibrium size [5~7] in any case is determined by the minimum in energy which is necessary to preserve the shape of the grain when passing from the paraelectric to ferroelectric states. As this ferroelectric phase change is related to electric, elastic, and thermal energy changes, it is necessary to discuss energy functions and state equations of materials at first.

2.2 State equations and thermodynamics of materials

2.2.1 The state equations

According to the thermodynamics, it is assumed that the thermal, elastic, and dielectric behavior of a homogeneous dielectric is fully described by six variables: temperature T, entropy S, Strain $\vec{x}$, Stress $\vec{\vec{X}}$, electric field $\vec{E}$, and electric displacement $\vec{D}$.

According to the first law of thermodynamics, the change in internal energy U (per unit volume) when an infinitesimal quantity of heat dQ is received by a unit volume of dielectric is given by:

$$dU = dQ + dW \qquad \text{Eq.2-1}$$

where dW is the work done on this same volume during the resulting quasi-static transformation.

Assuming reversibility, the second law of thermodynamics relates dQ to the absolute temperature and entropy in the form:

$$dQ = TdS \qquad \text{Eq.2-2}$$

If only the mechanic and electric work are related, the first law of thermodynamics is:

$$dU = dQ + dW_E + dW_m \qquad \text{Eq.2-3}$$

Where dW_E and dW_m are electric and elastic works, which can be written as:

$$dW_E = E_i dD_i$$

$$dW_m = X_I dx_I \qquad \text{Eq.2-4}$$

Here the Voigt´s notations (‘I’ means the tensor suffix and is from 1 to 6; ‘i’ means vector suffix and is from 1 to 3.) are used to express tensors and vectors [39]. This method provides some briefness for the expression of tensors and vectors. Some work used the same simplified notation for tensor but different notations for vectors (‘i’ means vector suffix and is x, y, or z.) [53] and this notation method is closer to the custom of electrical engineers. For the discussion of the present work, both notation methods are used interchangeably, as the notation of ‘i’ from both notation methods gives the same physical meaning. The Einstein notation for the summation of vectors and tensors is also used.

To describe a system, eight different thermodynamic potentials are defined:

Helmholtz free energy: $AE = U - TS$

Enthalpy: $HE = U - X_I x_I - E_i D_i$

Elastic enthalpy: $HE_1 = U - X_I x_I$

Electric enthalpy: $HE_2 = U - E_i D_i$

Gibbs free energy: $Gb = U - TS - X_I x_I - E_i D_i$

Elastic Gibbs energy: $Gb_1 = U - TS - X_I x_I$

Electric Gibbs energy: $Gb_2 = U - TS - E_i D_i$ Eq.2-5

The elastic Gibbs energy Gb_1 is frequently used in the literatures on ferroelectric phase transitions. By choosing (T, X_I, D_i) as independent variables, the differential form of elastic Gibbs energy can be written as:

$$dGb_1 = -SdT - x_I dX_I + E_i dD_i \qquad \text{Eq.2-6}$$

The other variables can be calculated as:

$$S = -\left(\frac{\partial Gb_1}{\partial T}\right)_{\overleftrightarrow{X},\vec{D}},\ x_I = -\left(\frac{\partial Gb_1}{\partial X_I}\right)_{T,\vec{D}},\ E_i = \left(\frac{\partial Gb_1}{\partial D_i}\right)_{T,\overleftrightarrow{X}} \qquad \text{Eq.2-7}$$

2.2.2 Linear state equations of materials and Maxwell relations

If only linear forms will be calculated, the other variables of state can be calculated as:

$$dS = \left(\frac{\partial S}{\partial T}\right)_{\vec{D},\overleftrightarrow{X}} dT + \left(\frac{\partial S}{\partial X_I}\right)_{\vec{D},T} dX_I + \left(\frac{\partial S}{\partial D_i}\right)_{\overleftrightarrow{X},T} dD_i \qquad \text{Eq.2-8}$$

$$dx_I = \left(\frac{\partial x_I}{\partial T}\right)_{\vec{D},\overleftrightarrow{X}} dT + \left(\frac{\partial x_I}{\partial X_I}\right)_{\vec{D},T} dX_I + \left(\frac{\partial x_I}{\partial D_i}\right)_{\overleftrightarrow{X},T} dD_i \qquad \text{Eq.2-9}$$

$$dE_i = \left(\frac{\partial E_i}{\partial T}\right)_{\vec{D},\overleftrightarrow{X}} dT + \left(\frac{\partial E_i}{\partial X_I}\right)_{\vec{D},T} dX_I + \left(\frac{\partial E_i}{\partial D_i}\right)_{\overleftrightarrow{X},T} dD_i \qquad \text{Eq.2-10}$$

The coefficients in the above equations are called compliances. In the same way, by choosing different variables, different coefficients can be obtained. For the cases of isothermal (or adiabatic), the equations can be generally described as:

$$dX_I = c_{I,J}^{\overleftrightarrow{D},T}\, dx_J - \widetilde{h}_{I,j}^{T}\, dD_j \qquad \text{Eq.2-11}$$

$$dE_i = -h_{i,J}^{T}\, dx_J + k_{i,j}^{\overleftrightarrow{x},T}\, dD_j \qquad \text{Eq.2-12}$$

$$dx_I = s_{I,J}^{\overleftrightarrow{D},T}\, dX_J + \widetilde{g}_{I,j}^{T}\, dD_j \qquad \text{Eq.2-13}$$

$$dE_i = -g_{i,J}^{T}\, dX_J + k_{i,j}^{\overleftrightarrow{X},T}\, dD_j \qquad \text{Eq.2-14}$$

$$dx_I = s_{I,J}^{\vec{E},T}\, dX_J + \widetilde{d}_{I,j}^{T}\, dE_j \qquad \text{Eq.2-15}$$

$$dD_i = d_{i,J}^{T}\, dX_J + \varepsilon_{i,j}^{\overleftrightarrow{X},T}\, dE_j \qquad \text{Eq.2-16}$$

$$dX_I = c_{I,J}^{\vec{E},T}\, dx_J - \widetilde{e}_{I,j}^{T}\, dE_j \qquad \text{Eq.2-17}$$

$$dD_i = e^{T}_{i,J}\ dx_J + \varepsilon^{\overleftrightarrow{X},T}_{i,j}\ dE_j \qquad \text{Eq.2-18}$$

The last four equations are called piezoelectric stain and stress equations. As the isothermal (or adiabatic process) will be usually discussed, the sign of constant T in the expression above is omitted in the following discussion.

2.2.3 Non-linear state and approximations

The linear state equations above are described by the linear differential equations. But some of the most important characteristics of ferroelectrics such as hysteresis loop, electrostriction, polarization reverse and so on are fundamentally non-linear effects and hence require an extension of the theory to higher orders. Generally the nonlinear state of materials can be described by expansion of the state equations to arbitrarily high orders to define the non-linear compliances, but the practical difficulties of tensor mathematics at high orders make it almost impossible. In order to show the physical meanings more clearly, some approximations have to be added:

- The prototype state is $D_i = X_I$=0, which means the original state has neither polarization nor stress;
- The state with polarization has its polarization along one of the crystallographic axes;
- Non-polar state is centrosymmetric.

Under the assumption above, the elastic free energy can be expanded as Taylor series [5, 40]:

$$Gb_1 = Gb_{10}(T) + \frac{1}{2}\alpha_1 D^2 + \frac{1}{4}\alpha_2 D^4 + \frac{1}{6}\alpha_3 D^6 + \frac{1}{2}sX^2 + Q_{es}XD^2 + \cdots \qquad \text{Eq.2-19}$$

Here, for the sake of simplicity, the suffixes of vectors and tensors are omitted as it will not change the physical meaning of the expression. In the following discussion, the same simplicity is also used until it is necessary to analyze the components of vectors and tensors.

2.3 Theoretical description of $BaTiO_3$ materials

2.3.1 Crystal symmetry and ferroelectric phases of $BaTiO_3$ single crystal

Two kinds of structures of $BaTiO_3$ are known. One belongs to the hexagonal system, and the other is perovskite. The first one does not show ferroelectricity and hence only the perovskite structures will be further discussed in this work. The perovskite-type structure, which is the

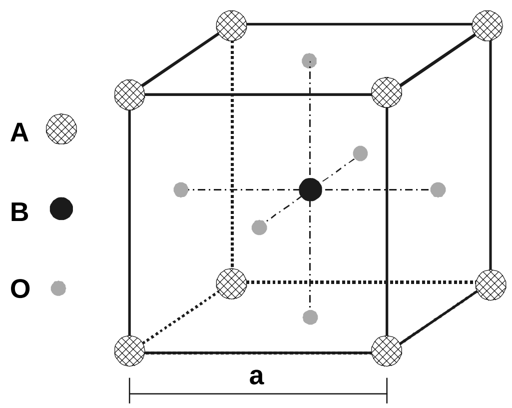

Fig.2-1: Perovskite-type structure ABO_3

large family of compounds with the general formula ABO_3, has the cubic non-polar phase (centrosymmetrical) and the spatial lattice is shown in Fig.2-1. The ‘a’ is the lattice constant. The perovskite $BaTiO_3$ belongs to this kind of materials and is cubic and nonpiezoelectric above the Curie point (about 130 °C). It is the tetragonal lattice system from Curie point to 0 °C, orthorhombic from 0 °C to –90 °C, and rhombohedral below –90 °C. The different ferroelectric polarization directions (shown as arrows) at different phases observed by experiments are illustrated in Fig.2-2.

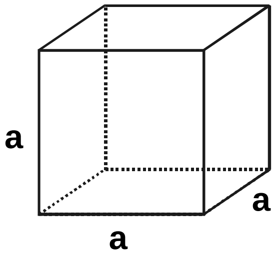

Fig.2-2a: Cubic
T > 130 °C

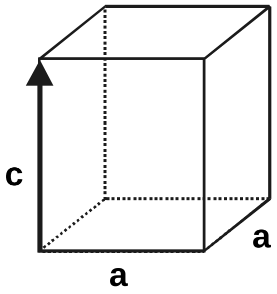

Fig.2-2b: Tetragonal
130°C > T > 0 °C

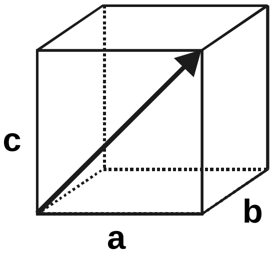

Fig.2-2c:
Orthorhombic
0 °C >T> –90 °C

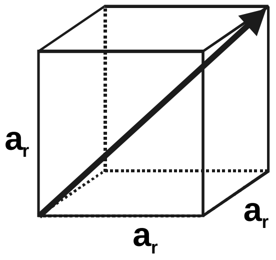

Fig.2-2d:
Rhombohedral
-90 °C >T

Under the assumption that phase change is small and the crystal has only a monodomain at ferroelectric phases, a phenomenological theory [40] was presented to explain the polarization in $BaTiO_3$ materials. The principle is to minimize the elastic Gibbs energy when the material goes through the phase changing point. From the equation Eq.2-19, by neglecting the terms higher than D^6, the electric field can be written as:

$$E = \frac{\partial Gb_1}{\partial D} = \alpha_1 D + \alpha_2 D^3 + \alpha_3 D^5 = 0 \qquad \text{Eq.2-20}$$

here D is equal to P, if electric field does not exist. During the phase change, $\vec{P}$ has three components:

$$\vec{D} = \vec{P} = P_x\,\vec{a}_x + P_y\,\vec{a}_y + P_z\,\vec{a}_z \qquad \text{Eq.2-21}$$

According to the Eq.2-20, the (P_x, P_y, P_z) can be solved for four possibilities:

a) (P_x, P_y, P_z)=0, Gb_a =0

b) $P_x = P_y$ =0, $P_z \neq 0$, $Gb_b \neq 0$ Tetragonal state, 130°>T>0°

c) P_x =0, $P_y = P_z \neq 0$, $Gb_c \neq 0$ Orthorhombic state, 0°>T>-90°

d) $P_x = P_y = P_z \neq 0$, $Gb_d \neq 0$ Rhombohedral state, -90°>T

Here Gb_a, Gb_b, Gb_c, and Gb_d are the Gibbs energy at the corresponding states. These four states before and after spontaneous polarization describe the facts which have been observed in experiments, as shown above in Fig.2-2.

To the same approximation, if X and E do not exist during the phase change, according to Eq.2-7 and Eq.2-19, it must be noted that the spontaneous strain:

$$x = \frac{\partial Gb_1}{\partial X} = Q_{es} P^2 \qquad \text{Eq.2-22}$$

Here Q_{es} is the electrostrictive coefficient. Because the electrostrictive effect exists in all materials, it means that spontaneous strain always accompanies spontaneous polarization.

The piezoelectric voltage coefficient is:

$$g = \frac{\partial^2 Gb_1}{\partial X\,\partial D} = 2\,Q_{es}\,\mathrm{P} \qquad \text{Eq.2-23}$$

The piezoelectric strain constant in the direction of polarization can be written as [5]:

$$d_{z3} = 2\varepsilon Q_{es} P \qquad \text{Eq.2-24}$$

That means that piezoelectric effect of ferroelectric materials at monodomain state is proportional to spontaneous polarization through electrostrictive constant.

2.3.2 The general domain structures of BaTiO3 single crystal in tetragonal phase

In reality, the monodomain state of material at ferroelectric phase, which is assumed above for the simplicity of discussion, does not exist [1~3]. Ferroelectric domain structures at ferroelectric phases are always formed by the electrostatic interaction on the surface and the inhomogeneity of stress in the materials, when $BaTiO_3$ single crystal goes through the phase change. At tetragonal phase, there are totally four structures of ferroelectric domains of $BaTiO_3$ single crystal material. The domain with a spontaneous polarization perpendicular to the surface of the material is called ‘c-domain’ and that with a spontaneous polarization on the surface of the material ‘a-domain’. There are totally four possibilities of domain boundaries, that is, if the surface is assumed as the [001] plane, the 90° a-a [110], 90° a-c [011], 180° a-a [010], and 180° c-c domain boundaries (domain walls). The last one has an arbitrary boundary form which is vertical to the surface. It should also be emphasized here that the domain walls exist possibly in any equivalent planes. On the surface of the c-domains, there are surface screen charges. Fig.2-3 shows the domain structures on a thin plate of $BaTiO_3$ single crystal.

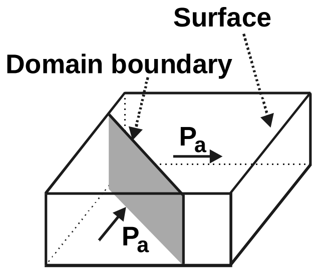

Fig.2-3a: 90° a-a domain wall [110]

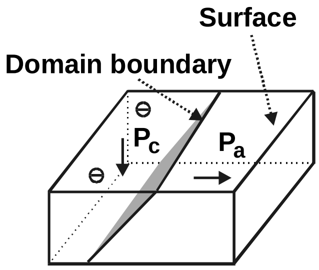

Fig.2-3b: 90° a-c domain wall [101]

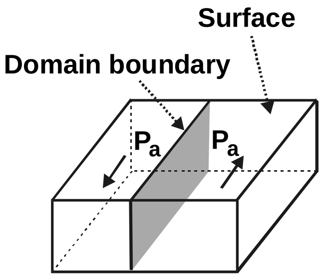

Fig.2-3c: 180° a-a domain wall[010]

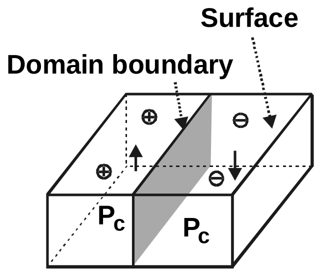

Fig.2-3d: 180° c-c domain wall

For the structures above, the domain wall width after the phase transition can be described by the minimizing the total free energy [3, 40~42]. The Gibbs free energy under the assumption above can be written as:

$$Gb = Gb_0 + W_E + W_{dip} + W_m + \int_V \left(\frac{1}{2}\alpha_1 D^2 + \frac{1}{4}\alpha_2 D^4\right) dV \qquad \text{Eq.2-25}$$

Here W_E, W_{dip}, and W_m are electric energy, energy by the dipolar interaction, and the elastic energy. The high order term of D^6 is further neglected for the simplicity. According to the theory above and by minimizing the total free energy, some work [41, 42] have analyzed the domain walls and leads to an estimation of wall thickness and wall energy of some materials. The typical values of $BaTiO_3$ single crystal are shown in table 1.

This prediction is naturally under the assumption that all the parameters and dimensions of domain walls can be described macroscopically. The results of the wall width calculated above are naturally not of a macroscopic dimension. There is also a microscopic approach which gives the same value of wall energy [43]. The methods and values here will be therefore accepted in this work, as other work do.

Materials	Wall thickness (nanometer)	Wall energy (mJ/m^2)
$BaTiO_3$ 180° walls	0.5~2	10
$BaTiO_3$ 90° walls	5~10	2~4

Table 1: The typical properties of domain walls of $BaTiO_3$ single crystal

2.3.3 The general domain structures of $BaTiO_3$ ceramics

The formation of domains in ceramics is different from that in single crystals because domain structures of a grain are formed under clamped conditions, whereas a single crystals is free. The domain size at equilibrium state in any case is determined by the minimum of the intern energy which is necessary to preserve the shape of the grain when passing from the paraelectric to ferroelectric state. Although there has been a lot of efforts to explain the relationship among grain sizes, domain widths, elastic, piezoelectric, dielectric properties and so on, a generally accepted theory to describe and explain all the relations needs also to be established [5~13]. Furthermore, how many kinds of structures of ferroelectric domains at the tetragonal phase of $BaTiO_3$ ceramics exist generally is still not clear. The following is the most widely accepted description of ferroelectric domain structures of $BaTiO_3$ ceramics at tetragonal phase in recent literatures [6~10].

It is found that there are different structures of domains in $BaTiO_3$ ceramics but two kinds of domain structures in $BaTiO_3$ ceramics are typically observed by chemical etching method. One exists mainly in the grains with sizes smaller than 10 μm and have simple laminated 90° domain structures. The other kind composes mainly of banded 90° domains if grain sizes are larger than 20 µm [6, 7].

For the first kind of domains in $BaTiO_3$ ceramics, according to the same phenomenological theory above, some work to calculate the relationship between the domain width and the grain size is presented. The domain width (d_w) with respect to the grain size g is calculated as [7]:

$$d_w \propto (g)^{1/2} \qquad \text{Eq.2-26}$$

The typical width of 90° domains is several hundred nanometers.

Another kind of ferroelectric domains exists whose domain structures are typically 90° banded domains and shown in Fig.2-4 [6, 8, 9, 10]. This kind of structures of $BaTiO_3$ ceramics was observed mostly if the grain size is larger than 20 µm. The two 90° domain structures of this kind of domains are shown in Fig.2-4. The α structure has a one-to-one correspondence of conjugated domain areas whereas the γ structure without any correspondence. The domain width $d_w^{'}$ can be calculated as [10]:

$$d_w^{'}(\mu m) \approx 0.104 g^{1/3} (1 + \frac{0.004}{g^{1/3} - 0.34}) \qquad \text{Eq.2-27}$$

If a coarse grain of $BaTiO_3$ ceramics has a dimension of 50 µm, the domain width is about 300 nm.

It is clear that the domain widths whose structures are known today are in the range of several hundred nanometer in $BaTiO_3$ ceramics.

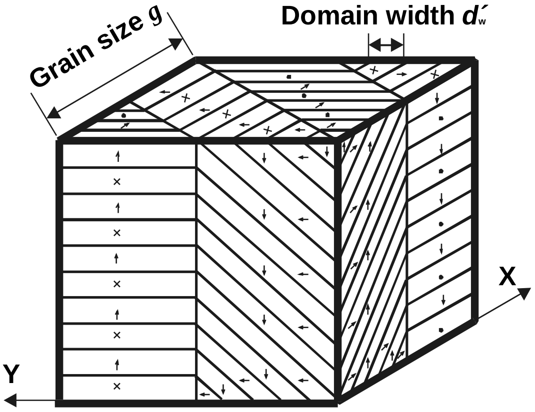

Fig.2-4a: α structure of 90° domain laminated structures

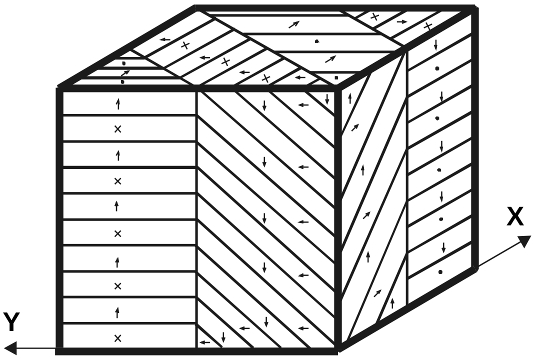

Fig.2-4b: γ structure of 90° domain laminated structures

Other types of domains of ferroelectric $BaTiO_3$ ceramics, such as those with no relationship to grain sizes, because of their complex natures and $\nabla \cdot \vec{P} \neq 0$ in the bulk materials, are less studied and little documented. The complicated relationships among domain structures, temperatures, electric and ferroelectric properties, and grain sizes are usually studied experimentally.

In recent literatures, domains and their effects on macroscopic properties of ferroelectric ceramics are studied experimentally. The dielectric, elastic, piezoelectric properties of ferroelectric ceramics are described by recent studies as the sum of intrinsic and extrinsic properties [11~13]. The intrinsic property of ferroelectric materials is defined as properties of the material with a monodomain and the extrinsic property the contribution from other parts of the material, such as domain wall movements. The dielectric constant ε, piezoelectric constant d, and elastic compliance s, are therefore written as follows:

$$\overleftrightarrow{\varepsilon} = \overleftrightarrow{\varepsilon}_{in} + \overleftrightarrow{\varepsilon}_{ex}$$

$$\overleftrightarrow{d} = \overleftrightarrow{d}_{in} + \overleftrightarrow{d}_{ex}$$

$$\overleftrightarrow{s} = \overleftrightarrow{s}_{in} + \overleftrightarrow{s}_{ex} \qquad \text{Eq.2-28}$$

The subscripts ‘in’ and ‘ex’ denote the intrinsic and extrinsic contributions.

Although a model for ferroelectric ceramics to describe the relationship between the intrinsic and extrinsic contributions under weak fields has only been presented recently, a generally accepted theory even by phenomenological methods is still not well developed [13]. The piezoelectric relation of Rayleigh model for ferroelectric ceramics will be accepted in this work [12]:

$$d_{z3} = 2\varepsilon_0\varepsilon_{rzz}Q_{11}P_z + 11.7\,X_{\max} \qquad \text{Eq.2-29}$$

where d_{z3} is the actual piezoelectric constant for ferroelectric ceramics; Q_{11}, P_z, and $X_{\max}$ are the electrostrictive constant, spontaneous polarization, and the maximum value of periodical stress by external fields. The first term is the so-called intrinsic piezoelectric effect. The detailed discussion of Rayleigh model and the dielectric and elastic relations will not be mentioned here for the simplicity of our discussion of the near-field acoustic imaging in this work.

2.4 Standard methods to image ferroelectric domains

The microscopic characterization of ferroelectric domains is always a challenge for scientists in this area. The classic work will be shortly mentioned here.

2.4.1 Chemical etching

This is the earliest way to visualize ferroelectric domains in ferroelectrics. Concentrated HCl etches the a- and c-domains of $BaTiO_3$ at different rates, and also +c and –c ends of the domains, so that a different texture or shade appears when the etched specimen is examined under a microscope [3]. It is a destructive method and how such an etching process influences subsequent domains is also not documented.

2.4.2 Powder methods

This method uses colloidal suspensions of charged particles, which deposit preferentially on either positive or negative ends of domains. It is a nondestructive method, but the difficult choice of powders and the limited resolution and contrast makes it not feasible for industry. Furthermore it is also very difficult to use it on materials with rough surfaces because the surface topography will add to the contrast of powder contrast.

2.4.3 Optical polarising microscopy

To observe ferroelectric domians, the usual method is the optical microscopy with a polariser and an analyzer. When the polariser and analyzer of the optical microscope are crossed at 90° orientations, no light is transmitted through microscope unless the specimen inserted produces a phase change between two differently polarized light rays passing through it. If it is assumed that the optical axis is also polar axis, for $BaTiO_3$, the c-domains will not change the phase of the light and appear dark. The a-domains will change the phase of the light and appear bright. It is also shown that one can image +c and –c domains by studying the strain-induced biaxial material along each domain wall [44]. Unfortunately, the optical method is limited by the diffraction limit of the focused light beam and the resolution is only about half of the light wavelength used. It will be difficult to obtain the resolution in submicrometer or nanometer range. Moreover, although this technique is the most common method to image ferroelectric domains of single crystals, it is very difficult to image ferroelectric domains of ceramics non-destructively, as the surface has to be polished to get sufficient contrast. To what extend the polishing process changes the domain structures is still not well studied.

2.4.4 X-ray diffraction and topography

Both methods require the polishing of the surface to increase the image contrast. The X-ray diffraction method is a typical method for the research of single crystals and films. It is an indirect method and by analyzing the diffraction angle, the surface polarization can be indirectly shown [44].

The contrast mechanism of X-ray topography [3, 45, 46] is that the anomalous dispersion of X-rays causes a difference between the X-ray intensity reflected from the positive and negative ends of domains. By using wavelengths close to an absorption edge of a constituent element this difference can be maximized. The domains in $BaTiO_3$ have been successfully observed by this methods. Although it is a classic method to analyze ferroelectric domains, its resolution and requirement of surface roughness limit its application.

2.4.5 SEM

Methods using SEM to observe domains are also presented [14]. The principle is based on changes of surface electric potential from domains to domains which will be imaged in secondary electron image. It has only a resolution of about several µm. The stability of the contrast of this method and its comparison with other techniques needs to be studied.

2.4.6 TEM

This method is the most powerful method to observe ferroelectric domains [15, 47, 48]. It presents a good resolution down to several nanometers or lower. But the sample preparation of this method is difficult and destructive, and whether the sample preparation would change the domains on the sample surface requires further investigation.

2.5 New methods and works to image ferroelectric domains

There are a large amount of literature which reported new techniques to image ferroelectric domains. It is but impossible to mention all the techniques here. Only some typical techniques will be briefly discussed in the followings.

2.5.1 Optical methods based on the second-harmonic generation

This technique can be used in principle for any crystal which can be matched in phase for second-harmonic generation with light propagation close to the polar axis [3, 49, 50]. Some work have also combined this technique with near-field optical methods [51]. Although some results on single crystals are presented, this method has no advantages for the analyses of

$BaTiO_3$ ceramics which are usually very rough at the surface and opaque.

2.5.2 Scanning Electron Environment Microscopy

This is a relatively new methods [52] and the principle is almost similar as that of SEM to image ferroelectric domains. But, because it uses a special environment in the vacuum chamber in SEM, the image contrast can be held for several hours. For crystal materials, some results have been obtained but those on ceramics have not been presented up to now. Its resolution is also in the range of several micrometer.

2.5.3 SEAM

This method uses a very thin gold film on the surface of the material to avoid surface charging effects and the results of both single crystal and ceramics are shown [16, 17, 37, 38]. The detailed description of the method will be discussed later in Chapter 4.

2.5.4 Scanning near-field acoustic microscopy based on SPM techniques

The name, Scanning near-field acoustic microscopy (SNAM), was introduced in 1989 [64] and there are a lot of developments with this technique up to today. For the sake of simplicity of the present work, the name SNAM would be used to mean all the systems based on SPM techniques to image acoustic properties. These methods are new and there is still a lot of discussion on it. To characterize the contrast of SNAM techniques on $BaTiO_3$ materials, although different set-ups and different results have been presented as discussed in Chapter 1, a new nondestructive method with nanometer resolution based on the combination of SPM and acoustic microscopy is introduced in this work [34~37]. This method provides a possibility to compare contrast of SEAM and SNAM techniques both theoretically and experimentally. A detailed description of this set-up of SNAM to image ferroelectric domain structures of $BaTiO_3$ will be presented later in Chapter 5.

2.6 Limitation: quasi-static

For all the discussion above, one of the most fundamental assumption is used. The discussion and imaging of ferroelectric domains are only discussed quasi-statically. The high frequency properties of ferroelectric domains will not be discussed here because the imaging mechanism of SEAM and SNAM will be mainly concerned in this work.

3 Electric and acoustic coupling in Scanning Near-field Acoustic Microscopy

3.1 General equations of electric and acoustic couplings in solids

Electrical and acoustic coupling equations are briefly discussed in Chapter 2. Their application combined with the classic electromagnetic and acoustic theories in actual near-field acoustic microscopy systems is discussed here. From Eq.2-15 to Eq.2-18, the piezoelectric strain and stress equations can be obtained by integration under the assumption of zero values of all the field components at equilibrium state:

$$x_I = s^{\vec{E}}_{I,J}\ X_J + \tilde{d}_{I,j}\ E_j \qquad \text{Eq.3-1}$$

$$D_i = d_{i,J}\ X_J + \varepsilon^{\vec{X}}_{i,j}\ E_j \qquad \text{Eq.3-2}$$

$$X_I = c^{\vec{E}}_{I,J}\ x_J - \tilde{e}_{I,j}\ E_j \qquad \text{Eq.3-3}$$

$$D_i = e_{i,J}\ x_J + \varepsilon^{\vec{X}}_{i,j}\ E_j \qquad \text{Eq.3-4}$$

Eq.3-1 and Eq.3-2 are piezoelectric strain equations and Eq.3-3 and Eq.3-4 stress equation. The constant $d_{i,J}$ ($\tilde{d}_{I,j}$ constants of the transposed matrix) is piezoelectric strain constant and $e_{i,J}$ ($\tilde{e}_{I,j}$ constants of the transposed matrix) piezoelectric stress constant.

The Maxwell equations to describe general electric and magnetic phenomena are [53]:

$$\nabla \times \vec{E} = -\frac{\partial \vec{B}}{\partial t} \qquad \text{Eq.3-5}$$

$$\nabla \times \vec{H} = \frac{\partial \vec{E}}{\partial t} + \vec{J}_c + \vec{J}_s \qquad \text{Eq.3-6}$$

where $\vec{E}$ and $\vec{H}$ are electric and magnetic field; $\vec{D}$ and $\vec{B}$ are electric displacement and magnetic flux density; $\vec{J}_c$ and $\vec{J}_s$ are conducting and source currents.

Acoustic vibrations or waves in solid materials are governed by the Newton´s law for dynamic motion under the classic view. Motions can be classified into two kinds: translational and rotational motions.

For translational motions, the Newton´s law can be written as:

$$\nabla \cdot \vec{X} = \rho \frac{\partial^2 \vec{u}}{\partial t^2} - \vec{F} \qquad \text{Eq.3-7}$$

where $\vec{u}$ is the displacement field of particles in materials and $\vec{F}$ is an external body force.

For the simplicity of discussion below, the velocity of particles ($\vec{v} = \frac{\partial \vec{u}}{\partial t}$) is used and Eq.3-7 can be written as:

$$\nabla \cdot \overleftrightarrow{X} = \rho \frac{\partial \vec{v}}{\partial \mathrm{t}} - \vec{F} \qquad \text{Eq.3-8}$$

For rotational motions, the Newton´s law can be written as:

$$X_{ji} - X_{ij} + G_k = 0 \qquad \text{Eq.3-9}$$

X_{ij} and X_{ij} are stress components and G_k is body torque.

Under the small signal and weak piezoelectric coupling approximations, the body torque can be neglected even if most of the materials of piezoelectric transducers are frequently ferroelectric, so that the stress tensor is always a symmetric tensor. Combining the electromagnetic and acoustic equations with the piezoelectric equations, one can obtain the general coupled equations for fields and waves in piezoelectric materials as [53]:

$$\rho \frac{\partial^2 \vec{v}}{\partial t^2} = \nabla \cdot \left(\overleftrightarrow{c} : \nabla_s \cdot \vec{v} \right) - \nabla \cdot \left(\overleftrightarrow{e} \cdot \frac{\partial \vec{E}}{\partial t} \right) + \frac{\partial \vec{F}}{\partial t} \qquad \text{Eq.3-9}$$

$$\mu_0 \overleftrightarrow{\varepsilon}_s \cdot \frac{\partial^2 \vec{E}}{\partial t^2} = -\nabla \times \nabla \times \vec{E} - \mu_0 \overleftrightarrow{e} : \nabla_s \frac{\partial \vec{v}}{\partial t} - \mu_0 \frac{\partial \vec{J}_s}{\partial t} - \mu_0 \frac{\partial \vec{J}_c}{\partial t} \qquad \text{Eq.3-10}$$

The equations above are theoretically brief but physical meanings are not easy to see directly. In order to study the contrast mechanism in near-field acoustic systems clearly, it is easier to analyze the coupling by separating Eq.3-9 and Eq.3-10 to different coupled groups. It is also necessary that the system be simplified so that analytical methods can be used.

3.2 Direct imaging of the coupling by a transducer

A general set-up of near-field acoustic microscopy is shown in Fig.3-1. In near-field area, if there is a certain stimulation which produces acoustic vibrations, the vibrations will transmit to a transducer which is in solid contact with the sample and will change the acoustic vibrations into electric signals. To understand the system systematically, we must study how the stimulation produces acoustic vibrations, how the vibrations transmit to the transducer, and how the transducer changes the acoustic waves into electric signals in the typical set-up. At first, the electric and acoustic signal change in the transducer will be discussed. The acoustic waves in near-field and their transmission in the sample, as they are more complicated, will be discussed in the next section.

Some typical data about this set-up are: the thickness of the sample is usually 2~5 mm and the

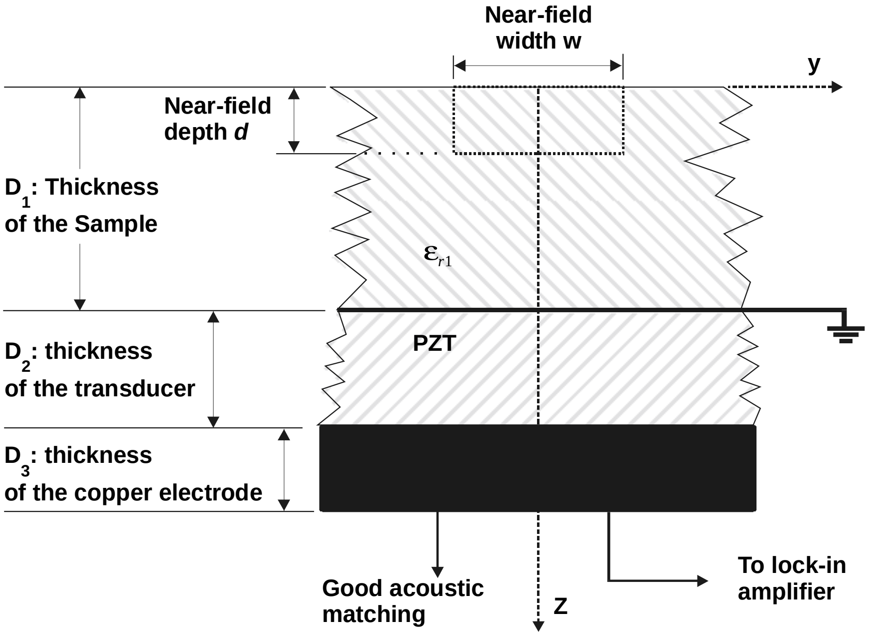

Fig. 3-1: Typical set-up of near-field acoustic microscopy

lateral dimension of the sample several 1~2 centimeter. The transducer has normally a thickness of 1~2 mm and a lateral dimension of 1~2 centimeter. The width of the near-field in lateral direction is dependent on the system and the material properties of the sample. Typical value of SEAM techniques on dielectric materials is several micrometers [57, 73]. As for SNAM discussed later in Chapter 5, the near-field width is several tens of nanometer.

Because the lateral dimension of the sample and the transducer is much larger than their thickness, the sample and PZT transducer can be approximately treated as thin plates with unlimited dimension in the lateral direction. Under such an approximation, the coupling in both kinds of material can be analyzed as the electric and acoustic coupling in one dimension.

Principally, the coupling in one dimension can be solved by the general coupling equation Eq.3-9 and Eq.3-10, but it is clearer to see the physical meanings by separating the basic equations to find different kinds of couplings. For a typical use of a transducer as the acoustic detector, electric signals, which are changed from acoustic signals, are always in the range of µV and can be treated as a small signal. The so-called small signal and weak piezoelectric coupling can be used. Under such approximations, a detailed calculation of electric and acoustic couplings in one dimension for $BaTiO_3$ crystal and PZT is presented in Appendix A1.

If the z direction is chosen as the transmission direction, there are three kinds of couplings in both materials. The first is the coupling between a quasi-static electric field E_z [53] and an acoustic longitudinal plane wave (v_z, X_3) which can be described by the coupling equation:

$$\frac{\partial^2 v_z}{\partial z^2} - \frac{\rho}{c_p}\frac{\partial^2 v_z}{\partial t^2} = 0, \text{ and } E_z = -\left(\frac{e_{z3}}{\varepsilon^s_{zz}}\right)x_3, \qquad \text{Eq.3-11}$$

(v_z, X_3) are the velocity of particles and the stress in z direction; x_3 is the strain in z direction. The quasi-static electric field E_z is coupled to acoustic wave (v_z, X_3) through strain component x_3.

The other two types of couplings are coupling between two electromagnetic plane waves (E_x, H_y) and (E_y, H_x) and two shear acoustic plane waves (v_x, X_5) and (v_y, X_4):

$$\frac{\partial^2 E_x}{\partial z^2} - \mu_0\varepsilon^s_{xx}\frac{\partial^2 E_x}{\partial t^2} = \mu_0 e_{x5}\frac{\partial^2 v_x}{\partial t \partial z} \qquad \text{Eq.3-12}$$

$$\frac{\partial^2 E_y}{\partial z^2} - \mu_0\varepsilon^s_{yy}\frac{\partial^2 E_y}{\partial t^2} = \mu_0 e_{x5}\frac{\partial^2 v_y}{\partial t \partial z} \ (\varepsilon^s_{yy} = \varepsilon^s_{xx} \text{ for BaTiO}_3) \qquad \text{Eq.3-13}$$

The physical meaning of Eq.3-11 is that, if a quasi-static electric field in a certain material is given, the electric and acoustic stiffened coupling can be detected by measuring the acoustic longitudinal plane wave produced by the electric field in that material; Or, if an acoustic longitudinal plane wave is given, there exists certainly a quasi-static electric field in z direction and by measuring this electric field, the coupling can be detected as well. Because a longitudinal transducer of the developed system is used to detect the longitudinal waves produced in the system in z direction, only the first coupling of Eq.3-11 will be further discussed in this work.

In the transducer, the harmonic acoustic longitudinal plane wave (v^3_z, X^3_3) can be written by the use of normal mode as [53]:

$$X^3_3 = -(a^{3+} + a^{3-})e^{j\omega t}/2 \qquad \text{Eq.3-14}$$

$$v^3_z = (a^{3+} - a^{3-})e^{j\omega t}/2Z_3 \qquad \text{Eq.3-15}$$

$$a^{3+} = a^{3+}(D_1)\ e^{-jk_3(z-D_1)} \qquad \text{Eq.3-16}$$

$$a^{3-} = a^{3-}(D_1)\ e^{jk_3(z-D_1)} \qquad \text{Eq.3-17}$$

in which $a^{3+}(D_1)$ and $a^{3-}(D_1)$ are amplitudes, Z_3 the characteristic resistance, and k_3 the wave number of the acoustic longitudinal wave in z direction in the transducer. The suffix '3' at the right top corner means waves in the transducer, and '+' and '-' indicate the wave transmission directions.

At the interface between the PZT transducer and the copper electrode, if the acoustic reflect constant at the boundary between the transducer and the back electrode is R, the wave forms a^{3+} and a^{3-} must satisfy the condition:

$$R = \frac{a^{3-}(D_1)e^{jk_3D_2}}{a^{3+}(D_1)e^{-jk_3D_2}} \qquad \text{Eq.3-18}$$

$$a^{3-}(D_1) = Ra^{3+}(D_1)e^{-2jk_3D_2} \qquad \text{Eq.3-19}$$

The electric field in the transducer in z direction under the open circuit condition can be expressed as [Appendix A1]:

$$E_z = -\left(\frac{e_{z3}^{PZT}}{\varepsilon_{zz}^{PZT}}\right)x_3 \qquad \text{Eq.3-20}$$

Here c_P^{PZT}, ε_{zz}^{PZT}, and e_{z3}^{PZT} are stiffened stiffness, dielectric, and piezoelectric constants of PZT in z-direction; x_3 is the strain in z-direction of longitudinal waves and has the form:

$$x_3 = \frac{1}{j\omega}\frac{\partial v_z^3}{\partial z} = -\frac{1}{2Z_3}\frac{1}{V_p}\,(a^{3+}+a^{3-})\,e^{-jk_3(z-D_1)} \qquad \text{Eq.3-21}$$

From Eq.3-19 and Eq.3-20, the quasi-static electric field in the transducer is:

$$E_z = -\left(\frac{e_{z3}^{PZT}}{\varepsilon_{zz}^{PZT}}\right)x_3$$

$$= \left(\frac{e_{z3}^{PZT}}{\varepsilon_{zz}^{PZT}}\right)\frac{1}{2Z_3}\frac{1}{V_p}\,(1+\mathrm{Re}^{-2jk_3D_2})\,a^{3+}(D_1)\,e^{-jk_3(z-D_1)} \qquad \text{Eq.3-22}$$

The voltage between two electrodes of the transducer under the open circuit condition is:

$$V_{output} = \int_{D_1}^{D_1+D_2} E_z dz$$

$$= \frac{1}{2jk_3}\left(\frac{e_{z3}^{PZT}}{c_P^{PZT}\varepsilon_{zz}^{PZT}}\right)a^{3+}(D_1)\,(1+\mathrm{Re}^{-2jk_3D_2})\,(1\text{-}e^{-jk_3D_2}) \qquad \text{Eq.3-23}$$

In all the equations above, $a^{3+}(D_1)$ is a constant determined by both the system boundary condition and the stimulation in near-field.

If the acoustic wave amplitude $a^{3+}(D_1)$ equals to one unit, which means that a homogenous acoustic longitudinal plane wave with unit amplitude transmits to the transducer, the amplitude and phase response of the transducer output signal to the frequency of the typical set-up shown in Fig.3-1 can be obtained. The amplitude and phase signal responses of the output to frequency are shown in Fig.3-2a and Fig. 3-2b.

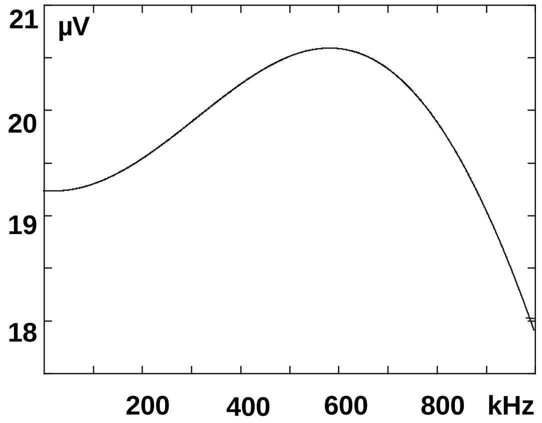

Fig. 3-2a: Amplitude response of the transducer to a unit longitudinal plane wave

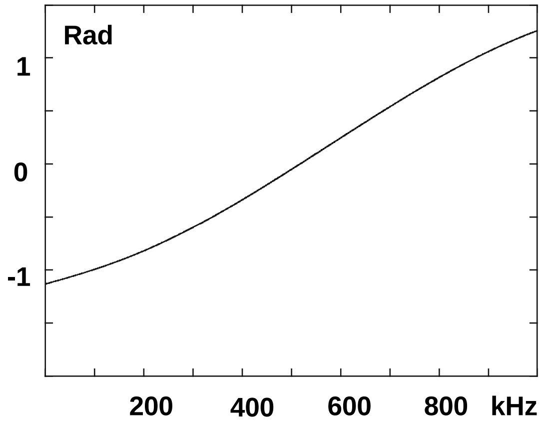

Fig. 3-2b: Phase response of the transducer to a unit longitudinal plane wave

Although Eq.3-23 describes the quantitative relationship between the acoustic longitudinal waves and the output signal of the transducer at open circuit condition, in the actual case of a scanning near-field acoustic microscopy system, the constant $a^{3+}(D_1)$ is dependent not only on the boundary conditions but also on the coupling source in the near-field. Therefore, it is necessary to analyze the coupling mechanism in the near-field and the whole transmission property of the system.

3.3 Piezoelectric coupling in near-field of the scanning near-field acoustic microscopy

To couple acoustic waves in a sample, different methods are used in non-destructive testing industry [59]. Conventional scanning acoustic microscope (CSAM) uses an acoustic lens to focus and inject the acoustic waves into the sample and therefore the resolution depends on the acoustic wave length according to the Rayleigh´s criterion. Although technologically usable acoustic waves in solids can reach to several GHz up to now, the required coupled liquid in CSAM system has such a high attenuation at this frequency range that the CSAM can only use the frequency below this range and the resolution can only reach several micrometers at most.

There is another kind of techniques whose resolution has no such a limitation, the so-called near-field acoustic methods [55~62]. A typical set-up is shown in Fig.3-1. The principle of this kind of microscopy is to produce acoustic waves by various interaction effects within a tiny volume at the direct vicinity of the sample surface. This volume is frequently defined as acoustic near-field and its dimension is much smaller than the wave length of acoustic waves used. Both lateral and depth profiling of these methods are generally dependent on this dimension [57~63]. The main interactions between the external stimulation and the material in near-field are photo, ion, electron, and, recently, probe acoustic coupling interactions. The acoustic waves generated in near-field by a certain interaction or several interactions will further transmit through the sample, be detected by a transducer, and finally be imaged by the system. Generally, the main interaction by different methods can be generalized as thermal coupling, generation of internal electric field, change of lattice constant and so on. The main types of microscope systems which use the near-field interaction can be generalized in the following.

Scanning photo acoustic microscopy (SPAM) uses a focused laser beam to produce acoustic waves in near-field [61]. The laser beam used has a wavelength typically in the visible range and a power from several mW to several hundred mW. According to the samples tested, the contrast mechanisms are mainly thermal and optoacoustic couplings. The former can be explained as that the chopped laser beam warms the sample in the near-field periodically, and, because of this periodical thermal energy change, the tiny piece of material in the near-field expands and contracts periodically. These periodical expansion and contraction produce acoustic waves which are related to thermal and acoustic properties. In the special case of optoacoustic samples, the direct optoacoustic coupling is used to produce acoustic waves. As the dimension of near-field area depends on the beam width of the injecting laser beam, which is formed by a focusing system, the resolution of this method is also dependent on factors such as the wavelength of the laser beam and the material properties of the sample. Except for the optoacoustic structures, the limited laser power presents a main drawback to the electric and acoustic coupling in near-field.

Scanning ion acoustic microscopy (SIAM) has a modulated microprobe with either a low [62] or a high [63] ion energetic (200 keV) beam implanter. The coupling mechanism is thermal acoustic coupling and the generation of excess carriers which form an internal electric field. This field can produce acoustic waves when the sample is piezoelectric. Although a low energy ion beam can be directly concentrated on the illuminated surface and obtain a good axial resolution, it presents a great risk of sample damage. Conversely, fast ions can penetrate further into the specimen, but the penetrating depth is so large that the axial resolution becomes worse. To characterize ferroelectric domains with high resolution and non-destructively, this kind of microscopy will not be convenient enough for the purpose.

Scanning electron acoustic microscopy (SEAM) has been developed considerably since its introduction in 1980 [55, 56] and different coupling mechanisms are discussed thoroughly

[16, 55~60]. It is principally a near-field technique which uses a tiny volume at the injecting point to generate acoustic waves. The acoustic coupling mechanisms are mainly classified as thermal acoustic coupling, piezoelectric acoustic coupling, and excess carrier acoustic coupling. Which contrast mechanism plays the most important role during the imaging is naturally dependent on the materials imaged [16]. For most metals, thermal coupling is the dominant effect [55~59]. If semiconductor materials concerned, the excess carrier coupling plays a main role by SEAM [16]. When piezoelectric materials are imaged, the piezoelectric coupling in the near-field has main effects on sound generation [16, 60]. During the last twenty years, different theories for the calculation of diffusion depth and lateral resolution of this technique have been developed [57, 58] and different results on different materials have also been presented. However, although much effort has also been given to image ferroelectric materials by SEAM [16, 60], the contrast mechanism of SEAM on ferroelectric materials is still not well understood because of the complexity of ferroelectric materials and SEAM technique. It is therefore necessary to analyze the contrast mechanism of SEAM on ferroelectric materials further. Moreover, as SEAM is a non-destructive acoustic method with a resolution in micrometer range, it presents itself as a perfect tool for a complementary analysis and an experimental basis for the development of new kinds of near-field microscopy with a resolution of submicrometer or nanometer range.

With the invention of Scanning probe microscope (SPM) in 1986 [18], different principles and experimental set-ups of Scanning near-field acoustic microscopy (SNAM) based on SPM have been developed recently [19~37, 64~70]. The principle of all the SNAM bases on coupling acoustic waves in near-field and detecting them by various methods. According to the set-ups developed, the main work can be roughly classified into two classes. One class uses a tunnel fork as an acoustic coupling source [64, 67, 68]. The other uses a common tip to couple or detect acoustic waves [19, 30~37]. According to the operation modes, SNAM can then be classified as SNAM with direct acoustic vibration coupling [64, 67, 68], direct contact force coupling [30, 34~35, 65, 66, 69, 70], or piezoelectric coupling [19, 22, 30, 31~33, 36, 37]. A detailed discussion on all the work is beyond the range of this work. Only the technique which is developed by the use of a transducer to detect the acoustic longitudinal waves produced in near-field for the analysis of ferroelectric materials [36, 37] will be discussed in detail in this work. The resolution of this mode of SNAM is basically dependent on the dimension of the near-field which is formed just beneath the contact point of a scanning probe by an applied ac voltage. Because the scanning probe has a very sharp form and a diameter down to 10 nm at the very tip, the lateral dimension of the near-field under the probe has also a lateral resolution with almost the same order. This provides an ideal condition to study ferroelectric domains and material properties at submicrometer or nanometer resolution. Furthermore, the use of an acoustic transducer at the backside of the sample for the detection of acoustic vibrations produced in near-field provides a solid base for the comparison of contrast among different near-field acoustic microscopy systems both experimentally and theoretically.

For the comparison of the contrast in this work, two typical near-field techniques which have the highest resolution among all the near-field acoustic microscopy techniques, the developed SNAM set-up and SEAM, will be chosen and discussed. For the analysis of ferroelectric properties of $BaTiO_3$ materials by both techniques, only the mechanism of the generation of internal electric field in near-field will be discussed here, as both techniques rely on this mechanism to generate acoustic vibrations in near-field. For SEAM, the electric field in near-field is produced by the trapped charges in the sample. For SNAM system developed, the electric field is concentrated just under the tip because of the very sharp form of the tip and will be discussed in Chapter 5 in detail. Naturally, for the reliability of complementary analyses, both techniques use the same experiment set-up, such as the same transducer and sample holder, to investigate the same sample at identical areas.

Although it is necessary to make a thin gold film (about several nanometer thick) on the sample for SEAM study, this film is so thin that it will not change the acoustic boundary conditions and therefore has no effect on the harmonic acoustic wave solutions. In the same way, although the tip of SNAM is in contact with the sample surface, the contact force between the tip and the sample surface is kept constant during the scanning by the topographical feedback control unit of SPM. For the harmonic acoustic waves, this constant force has no effect on the harmonic acoustic wave solutions either.

Based on the discussion above and from the point view of acoustic transmission, we can generalize both systems on ferroelectric $BaTiO_3$ materials as one typical set-up shown in Fig.3-1 with an electric field stimulation in near-field.

In this typical near-field acoustic system with an electric field stimulation in near-field, some basic assumptions have to be introduced in order to analyze the system quantitatively:

- The working frequency is usually in the range from several kHz to several hundred kHz. The wave length of electromagnetic waves is several kilometers and that of acoustic waves several centimeters. The set-up has a typical dimension of several centimeters. Because the wavelength of electromagnetic wave (several km) in the system is much greater than the dimension of the set-up and the wavelength of an acoustic waves (several centimeter) has the same dimension as the set-up, the electric problem can be treated as a quasi-stationary problem and the acoustic problem a wave transmission problem;

- Based on the theory of acoustic plate wave guide [53], the acoustic waves produced by the electric field in near-field are very complicated and there are different modes. According to the orthogonality of acoustic wave modes, all the wave modes can be expanded as a sum of plane waves with different spatial transmission directions. Because a longitudinal transducer is used in the system to change acoustic longitudinal waves into electric signals, only the longitudinal waves transmitted in z direction will be changed into electric signals by the transducer. As the lock-in technique is used to amplify the changed electric signal with the same frequency as the electric field source, we need only to consider the acoustic plane wave with the same frequency as that of the source. For the acoustic plane waves transmitted only in z direction with the frequency of the source field, we can use the transmission line mode to calculate only these longitudinal plane waves in the near-field approximately. A detailed calculation of electric and acoustic coupling of plane waves in $BaTiO_3$ is shown in Appendix A2;
- Because the field is concentrated in the middle of the sample and transducer, the boundary effects in the transactional plane is neglected for wave transmission. It means the plane wave approximation for both electric and acoustic fields can be used in the sample and in the transducer;
- The signal is so weak that the small signal approximation in acoustics can be used;
- The coordinate axes are chosen to coincide with the crystal axes in the sample and transducer;
- The contact between the sample and the electrode of the transducer and between the transducer and the copper electrode, and both electrodes of the transducer are so thin that their effects are neglected;
- The backside of the copper electrode is acoustically matched so well that there is no reflected acoustic waves back to electrode;
- The impedance of the lock-in amplifier is so large that the transducer can be assumed to work under open circuit condition approximately.

Under the assumptions above, if an electric field source $\vec{E} = E_s\, \vec{a}_z$ in near-field is given, the harmonic acoustic longitudinal plane wave (v_z^1, X_3^1) produced in the near-field by this source is governed by the equation (Appendix A1):

$$\frac{\partial X_3^1}{\partial z} = \rho \frac{\partial v_z^1}{\partial t} \qquad \text{Eq.3-24}$$

$$\frac{\partial v_z^1}{\partial z} = \frac{1}{c_p}\frac{\partial X_3^1}{\partial t} + \frac{e_{z3}}{c_p}\frac{\partial E_s}{\partial t} \qquad \text{Eq.3-25}$$

The suffix ‘1’ at the right top corner in the expression (v_z^1, X_3^1) means the area in near-field of the sample.

The stable harmonic solutions of the longitudinal plane wave in near-field can be solved by the one-dimensional transmission line mode as (A2, Appendix):

$$X_3^1 = -(a^{1+} + a^{1-})e^{j\omega t}/2 \qquad \text{Eq.3-26}$$

$$v_z^1 = (a^{1+} - a^{1-})e^{j\omega t}/2Z_0 \qquad \text{Eq.3-27}$$

$$a^{1+} = a_s^{1+}(z)e^{-jkz} + a^{1+}(0)e^{-jkz},$$

in which a_s^{1+} (z)= $\int_0^z (Z_0 \frac{e_{z3}}{c_p}\frac{\partial E_s}{\partial t})e^{jk\zeta}d\zeta$ $(0 \le z \le d)$ Eq.3-28

$$a^{1-} = a_s^{1-}(z)e^{jkz} + a^{1-}(d)e^{jk(z-d)},$$

in which a_s^{1-} (z)= $\int_z^d (Z_0 \frac{e_{z3}}{c_p}\frac{\partial E_s}{\partial t})e^{-jk\zeta}d\zeta$ $(0 \le z \le d)$ Eq.3-29

Here $Z_0 = \sqrt{\rho c_p}$ is the characteristic resistance of wave (v_z^1, X_3^1) in near-field. $a_s^{1+}(z)$ and $a_s^{1-}(z)$ are wave amplitude terms resulting from the source electric field in near-field. $a^{1+}(0)$ and $a^{1-}(d)$ are constants which are determined by boundary conditions as shown in the set-up of Fig.3-1, if the source is given.

The waves outside the near-field but still in the sample are governed only by the wave equations without source (Eq.3-11) and can be written as (v^2, X_3^2):

$$X_3^2 = -(a^{2+} + a_2^{2-})e^{j\omega t}/2 \qquad \text{Eq.3-30}$$

$$v_z^2 = (a^{2+} - a^{2-})e^{j\omega t}/2Z_0 \qquad \text{Eq.3-31}$$

$$a^{2+} = a^{2+}(d)e^{-jk_2(z-d)} \qquad \text{Eq.3-32}$$

$$a^{2-} = a^{2-}(d)e^{jk_2(z-d)} \qquad \text{Eq.3-33}$$

Here $a^{2+}(d)$ and $a^{2-}(d)$ are constants which can be determined by boundary conditions of the system and the source, ω the angular frequency, and k_2 acoustic longitudinal wave number in the z direction in the sample outside the near-field. The suffix ‘2’ at the right top corner indicates the area outside the near-field but still in the sample.

It is clear that the wave number inside and outside the near-field is the same, as all the longitudinal waves transmit inside and outside the near-field with the same material constants. That means $k = k_1 = k_2$.

The acoustic boundary conditions of the model shown in Fig.3-1 are generally the same:

$$X_3^1=0 \qquad \text{if } z = 0; \tag{Eq.3-34}$$

$$X_3^2 = X_3^1 \qquad \text{if } z = d; \tag{Eq.3-35}$$

$$v_3^2 = v_3^1 \qquad \text{if } z = d; \tag{Eq.3-36}$$

$$X_3^3 = X_3^2 \qquad \text{if } z = D_1 \tag{Eq.3-37}$$

$$v_3^3 = v_3^2 \qquad \text{if } z = D_1 \tag{Eq.3-38}$$

$$a^{3-}(D_1) = Ra^{3+}(D_1)e^{-2jk_3D_2} \qquad \text{if } z = D_1 + D_2 \tag{Eq.3-39}$$

here R is the acoustic reflection constant of the copper electrode to the longitudinal wave. The backside of copper electrode is well matched acoustically.

From the set-up shown in Fig.3-1, the acoustic waves in near-field are described by Eq.3-26 to Eq.3-29, waves in the sample but outside the near-field area by Eq.3-30 to Eq.3-33, and waves in the transducer by Eq.3-14 to Eq.3-17. If the source field in near-field is given, $a_s^{1+}(d)$ and $a_s^{1-}(0)$ are two terms of source integration in near-field and are also given. There are six constants $a^{1+}(0)$, $a^{1-}(d)$, $a^{2+}(d)$, $a^{2-}(d)$, $a^{3+}(D_1)$, and $a^{3-}(D_1)$. There are also six independent linear boundary equations from Eq.3-33 to Eq.3-39. There is only one single solution for all the constants. A detailed solution of all the constants can be found in Appendix A2. The acoustic longitudinal wave amplitude in the transducer under the open circuit and weak coupling conditions can be written as:

$$a^{3+}(D_1) = \frac{e^{-jkD_1}}{(1+e^{-2jkD_1})(1+\mathrm{Re}^{-2jk_3D_2})} \frac{4jZ_0 \dfrac{e_{z3}}{c_p} \int_0^d \dfrac{\partial E_s}{\partial t} \sin(k\zeta)d\zeta}{1+\alpha_1\alpha_2\beta_a} \tag{Eq.3-40}$$

in which $\alpha_1 = \dfrac{1-e^{-2jkD_1}}{1+e^{-2jkD_1}}$, $\alpha_2 = \dfrac{1-\mathrm{Re}^{-2jk_3D_2}}{1+\mathrm{Re}^{-2jk_3D_2}}$, and $\beta_a = \dfrac{Z_0}{Z_3}$.

The expression is very complicated but the physical meaning is very clear. The term $\int_0^d \frac{\partial E_s}{\partial t}\sin(k\zeta)d\zeta$ at the right side of Eq.3-40 is the source coupling in near-field. The rest at the right side of Eq.3-40 is the system transmission function which is determined by the boundary conditions of the system. The acoustic wave amplitude $a^{3+}(D_1)$ is dependent on both the coupling source in near-field and the transmission function of the system. From Eq.3-40, the output signal of the transducer under the open circuit and weak coupling conditions can be easily found from Eq.3-23:

$$V_{output} = \frac{1}{2jk_3}\left(\frac{e_{z3}^{PZT}}{c_P^{PZT}\varepsilon_{zz}^{PZT}}\right)a^{3+}(D_1)\ (1+\mathrm{Re}^{-2jk_3D_2})(1\text{-}e^{-jk_3D_2})$$

The final output signal of the transducer is:

$$V_{output} = 2(\frac{e_{z3}}{c_p})(\int_0^d \frac{\partial E_s}{\partial t}\sin(k\zeta)d\zeta)\left(\frac{e_{z3}^{PZT}}{\varepsilon_{zz}^{PZT}}\right)(\frac{1}{\omega})(\frac{1-e^{-jk_3D_2}}{1+e^{-2jkD_1}})(\frac{\beta_a}{1+\alpha_1\alpha_2\beta_a})e^{-jkD_1}$$

Eq.3-41

The first term at the right side of Eq.3-41 is only related to the material properties in near-field; the second term is the term determined by source electric field in near-field; the third term is the parameter of PZT transducer; The rest is dependent on the detecting system shown in Fig.3-1.

Eq.3-41 means that if the source $\vec{E} = E_s\,\vec{a}_z$ in near-field is given, the output signal of the transducer at the open circuit condition for set-up shown in Fig.3-1 can be obtained. For a given system, if the source field E_s is kept constant during the scanning, the change of V_{output} is only related to material properties $(\frac{e_{e3}}{c_p})$ in near-field. As it is shown in Eq.2-24, the piezoelectric constant d_{z3} (i.e. e_{z3} in Eq.3-41) is dependent on polarization. Therefore, if the coupled source electric field in near-field can be kept constant during the scanning and there is difference of polarization in near-field of every scanning point, the final acoustic image of experiment set-up Fig.3-1 is an image of the change of ferroelectric polarization in near-field. This is the contrast mechanism of near-field set-up shown in Fig.3-1 to image ferroelectric domains in $BaTiO_3$ material systems. It can be seen later that this is also the theoretical background for the complementary study on ferroelectric domains of $BaTiO_3$ materials by SEAM and SNAM techniques, as the contrast mechanism of both techniques is the same. If, however, the coupled source electric field distribution is scattered by a defect in near-field, the output signal of the transducer will be naturally dependent on the scattering source and the average piezoelectric effect in near-field. This is also the contrast origin of defects in near-field which can be imaged by SEAM and SNAM.

Furthermore, for the development of experimental set-ups of both near-field techniques based on the theory above, it is also necessary to estimate the value of output signal from the transducer. From the Eq.3-41, the value of piezoelectric constants e_{z3} of piezoelectric $BaTiO_3$ and PTZ transducer have almost the same value. The stiffened piezoelectric constant in near-field is about 10^{11} for $BaTiO_3$ and dielectric constant of PZT ε_{zz}^{PZT} is about 10^{-12}. The near-field depth is usually in the range of µm. The thickness of the sample and transducer is also in millimeter range. If it is assumed that the typical electric field in the near-field is smaller than 10 kV/m, which is small enough not to change the domain structures in near-field, the output signal of the transducer is in the range of µV. This signal is naturally in the background of white noise. We have to use the lock-in amplifier to detect such a small signal submerged in the white noise background.

How these two kinds of near-field microscopy techniques couple the source electric field in near-field, how the detailed experiment set-ups for both systems are established based on the theory above, and how large is the near-field depth of both systems will be discussed in a parallel way in the following chapter 4 and 5.

4 Scanning Electron Acoustic Microscopy

4.1 Physical background, signal generation, and contrast mechanism

The physical processes by injecting electrons in Scanning electron microscopy (SEM) are discussed thoroughly by some work [55~60, 71~73]. The Scanning electron acoustic microscopy (SEAM) was developed from the commercial SEM to analyze the acoustic properties of materials [55, 56]. According to different applications, the mechanisms can be generally classified into thermal acoustic coupling, piezoelectric coupling, and excess carrier coupling [16]. For the thermal acoustic coupling, some authors introduced a detailed discussion of coupling equation and output signal of the transducer in SEAM [58, 75] which will not be discussed in this work.

For the piezoelectric coupling mechanism, although some work has been done to analyze the coupling mechanism [16], a detailed explanation of this kind of mechanism for the imaging of ferroelectric domains in SEAM has not been introduced until recently [60]. In that work, the authors have discussed the piezoelectric coupling effect in the ferroelectric $BaTiO_3$ material by SEAM, but the acoustic solutions were assumed the same inside and outside the near-field. It was an assumption which did not satisfy the acoustic wave equation Eq.3-11 in the area outside the near-field but still in the sample.

For the future analysis of ferroelectric materials by near-field acoustic microscopy techniques, it is obligatory to study this mechanism further. As this kind of mechanism concerns the coupling of mechanic and electric phenomena in near-field, a detailed analysis of physical process of electron injection in near-field by primary electrons (PE) is also necessary.

If only the insulating materials are concerned, some authors introduced some models to describe field distributions in the insulating materials bombarded by PE [71~74]. Most of the models have assumed that the electric field in electron injecting area is uniform in the injection direction. This is naturally against Gauss´s theorem. A more accurate model to calculate electric field formed by injection electrons was introduced [74]. Although this model is impossible to explain all the actual phenomena of bombardment on insulating materials by PE, it is the most accepted model in this aspect today. Therefore this model is chosen as the base for the analyses of the contrast mechanism of SEAM on ferroelectric $BaTiO_3$ materials.

According to the model, the PE injects into a sample and forms a trapped charge distribution. For a typical set-up of SEAM system, the charge distribution in an insulator by a bombardment of primary electrons is shown in Fig. 4-1. The charge accumulating area has two parts. The first is the positive charged area ρ^+, which is caused by the emission of secondary electrons (SE) with a quantum yield δ. The depth d^+ of this area is less than several nm for metals and from 10 to 50 nm for insulators. The rest of PE inject through this area and further into the sample until they come to rest. A fraction of electrons will be back scattered (with a backscattering coefficient η_E) and the rest of electrons form a negative charged layer with density of ρ^- and depth d^-. The depth of penetration d is $d^+ + d^-$ which is dependent on accelerating voltage and the material properties [57, 60].

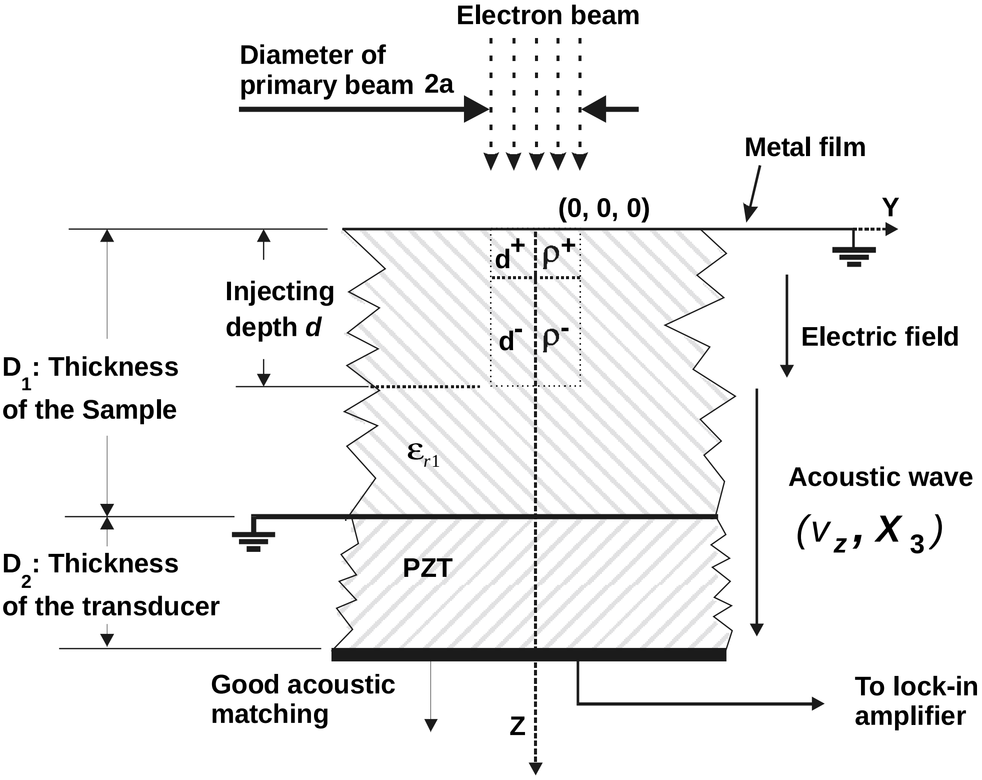

Fig.4-1: Process of electron bombardment on a ferroelectric material

If the PE keeps on injecting the area, the charge will be accumulated. The conductivity of the sample will discharge this charge distribution. At the same time, the electric field which is formed by the accumulated charge will force the electrons to migrate up to the surface. If the sample surface is grounded by a thin metal layer, the injecting electrons and the electrons discharged and migrated will have an equilibrium state after a time τ_e. In this state, a stable electric field will be produced in the injected area in the sample. Unfortunately, this time constant τ_e is very difficult to evaluate, because it depends on both material properties and experiment arrangement and currently can only be decided by experiment.

If the intensity of PE is modulated with an angular frequency ω, the electric field distribution can also be established after a delay time factor longer than τ_e. In this case, the electric field formed has also an angular frequency of ω. To study the problem further, some approximations have to be made. As it can be seen later, even under such approximations, the solution of piezoelectric mechanism in SEAM has a very complicated form.

Besides the fundamental approximations to analyze near-field microscopy systems in Chapter 3, some special approximations for SEAM must be assumed here:

- The dimension of near-field of SEAM is so small compared to sample and wavelength, that the anisotropic properties for the calculation of electric field in near-field can be neglected;
- The emission of SE takes place mainly at the surface of the metallic layer, so that there is only a negatively charged area in the sample with a density of ρ^- ;
- The penetration charge will be assumed that it is a charge cylinder (diameter 2a and length d) in the sample with defocus condition, so that the electric field component in radial direction is neglected and the electric field component E_z is uniform and equals the electric field in the middle of the near-field;
- The illumination time of PE at every scan point is greater than the discharge delay time τ_e of the materials, so that a stable harmonic field distribution is established.

From Fig. 4-1, if the sample has a thin layer of metal on the surface, the stable electric field distribution can be calculated by the use of an image charge distribution. With the approximations above, the electric field along the z axis is [74]:

$$E_s = A'(z-d)e^{j\omega t} \quad (\, 0 < z < d\,,\ x^2 + y^2 \le a^2)$$

$$E_s = 0 \qquad (\, z > d \text{ and } z < 0,\ x^2 + y^2 \ge a^2\,) \qquad \text{Eq.4-1}$$

where ρ^- is the density of stable charge distribution in near-field and ε_{zz} is the dielectric constant in z direction of $BaTiO_3$ materials. The x, and y components of electric field are neglected as they are small compared to z component. The electric field distribution of Eq.4-1 is the source field E_s in near-field of SEAM.

The electric field source in near-field with harmonic time variation is:

$$E_s = A'(z-d)e^{j\omega t} = e^{-\tau_e} \frac{(1-\eta_E)I_0}{\pi a^2 \varepsilon_{zz} d}(z-d)e^{j\omega t} \qquad \text{Eq.4-2}$$

The acoustic source in near-field for $BaTiO_3$:

$$\frac{e_{z3}}{c_p}\frac{\partial E_s}{\partial t} = A(z-d)\ e^{j\omega t}$$

in which $A = j\omega\,\frac{e_{z3}}{c_p}\,\frac{(1-\eta_E)I_0}{\pi a^2 \varepsilon_{zz} d}\,e^{-\tau_e}$ Eq.4-3

The output signal of a PZT transducer under the open circuit condition is [A3, appendix]:

$$V_{output} = 2\,j\,(\frac{e_{z3}}{\rho\varepsilon_{zz}^{s}})(\frac{(1-\eta_E)I_0}{\pi a^2 d}e^{-\tau_e})\left(\frac{e_{z3}^{PZT}}{\varepsilon_{zz}^{PZT}}\right).$$

$$(\frac{\sin(kd)-kd}{\omega^2})(\frac{1-e^{-jk_3D_2}}{1+e^{-2jkD_1}})(\frac{\beta_a}{1+\alpha_1\alpha_2\beta_a})\,e^{-jkD_1} \qquad \text{Eq.4-4}$$

In Eq.4-4, $\alpha_1 = \frac{1-e^{-2jkD_1}}{1+e^{-2jkD_1}}$, $\alpha_2 = \frac{1-\mathrm{Re}^{-2jk_3D_2}}{1+\mathrm{Re}^{-2jk_3D_2}}$, and $\beta_a = \frac{Z_0}{Z_3}$.

The term in the first bracket of Eq.4-4 is directly related to the material properties in near-field; The term in the second bracket is about the charge distribution in near-field; The term in the third bracket is related to the properties of the PZT transducer; The remaining four terms are related to detecting set-up and have a very complicated frequency dependence.

As it is explained in chapter 2, if the extrinsic contribution of the domain walls to the piezoelectric effect in ferroelectric materials is neglected, the constant of e_{z3} (or d_{z3}) is directly related to ferroelectric polarization [see Eq.2-24]. If there are c- and a- domains on the two areas on the surface of $BaTiO_3$ materials, the area of c-domains has polarization parallel to the z direction and has a non-zero value of e_{z3} in near-field. Whereas the area of a-domains, which has a polarization perpendicular to the z direction, will have zero value of e_{z3}. This is the contrast mechanism of SEAM on the ferroelectric $BaTiO_3$ single crystal.

Eq.4-4 has a very complicated frequency dependence, which is proved by SEAM experiments [34, 38]. This dependence results from the frequency term in Eq.4-4 and can only be analyzed by computer simulation. The computer simulation is completed by the use of the free Linux software Octave Ver. 2.0.13 and the result is shown in Fig.4-2. As the typical frequency range of most lock-in amplifier is from several Hz to 200 kHz, the amplitude and phase response of the output signal of the transducer in this frequency range has a dependence of frequency shown in Fig.4-2. Early experimental work [38] revealed the same tendency of the acoustic output signal in SEAM in this frequency range.

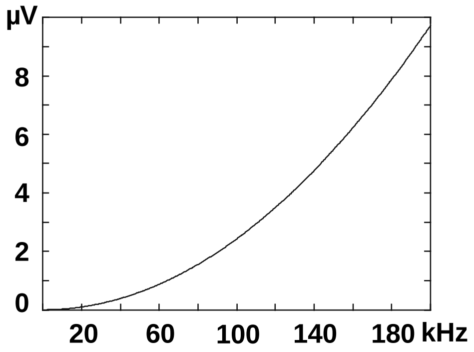

Fig.4-2a: Amplitude of the output signal of the transducer in SEAM

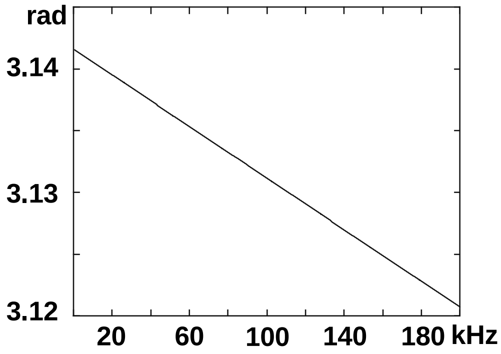

Fig.4-2b: Phase of the output signal of the transducer in SEAM

If there is domain contrast, the output signal is directly proportional to primary beam current. It is proved by experiment that the domain contrast of SEAM is better with large beam current [38]. However, the dependence of domain contrast with respect to injecting depth is relatively difficult. Up to now, most of the models to describe SEAM contrast have only mentioned the thermal mechanism whose contrast is originated from the periodical thermal diffusion by the injection of modulated PE. For the contrast originated from ferroelectric domains, as it is shown by the model discussed above, the near-field area is actually the whole injecting depth of primary electrons. Detailed discussion about this injecting depth has been presented [57, 73] and the injection depth will be used directly here.

4.2 Experiment set-up

The experimental set-up of SEAM is shown in Fig.4-3. It can be developed from a commercial SEM. The SEM used in this work is Model S150 and CS2 from Cambridge Microscope Ltd. The software from Triple-O Microscopy Company Ltd. is used to control the simultaneous imaging of secondary electron image (SEI) and electron acoustic image (EAI). The function generator HP8801 is used as the signal source and the lock-in amplifier Itaho3053 is used to amplify the electron acoustic signal. The system acquires both SEI and EAI simultaneously, so that the occasional noise will be minimized. The beam current is measured by a normal Faraday cup.

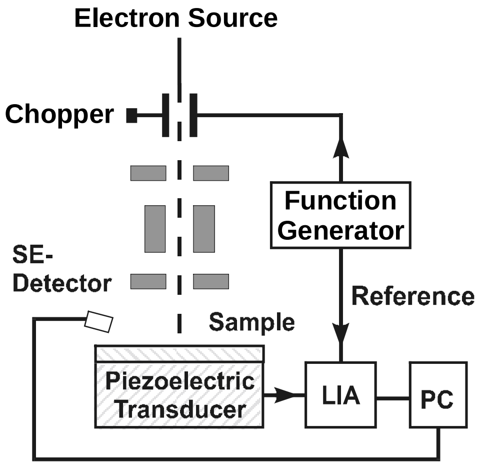

Fig.4-3: Setup of SEAM

The piezoelectric transducer is PX5 piezoelectric ceramics from Company Valvo [76]. Some of the typical results are presented [34, 36, 37, 38].

4.3 Discussion of the signal and noise

To evaluate an imaging system, it is always to analyze some important parameters, such as time resolution and bandwidth, lateral and depth resolution, sensitivity and signal-noise ratio, stability, and the test time.

As discussed above, The illumination time of PE at every scan point is greater than the discharge delay time τ_e of the materials, so that a stable harmonic field distribution is established. This discharge delay time τ_e is dependent on both the injecting beam and the sample studied. A typical value for insulating materials under the bombardment of the PE with current density of 1μA/mm^2 is 0.1 ms [74]. For a typical image of 400*400 resolution scanned by a computer controlled SEM, the scanning beam can stay for 10 ms at every pixel. That means this delay time has no significant effect on the typical SEAM imaging process.

As presented by other work [55~61], the lateral and depth resolution of SEAM are mainly dependent on the interaction volume of PE penetration, which is defined as the volume of near-field for SEAM in this work. Whereas the near-field volume has the dimension of the thermal diffusion volume in case of thermal mechanism, the near-field volume by piezoelectric mechanism has a depth resolution of the whole PE penetration depth. Typical value of penetration depth of SEAM image with 20 keV primary electrons is about 2~3 μm [55] which is dependent on the materials studied.

The lateral resolution is also dependent on the dimension of the near-field. For the imaging of ferroelectric material, if there is a surface polarization in near-field, this polarization will naturally affect the lateral distribution of electrons of injecting PE. As a result, the dimension of the near-field is changed. Because the piezoelectric vibration mode change and lateral electric field distribution in near-field are very complicated and little documented in the literatures up till today, it can only be estimated experimentally. Unfortunately, from the experiment results this effect is little documented too.

The signal to noise ratio can also be estimated. If the noise from function generator, SEM, and the measuring circuit and lock-in amplifier are σ_G, σ_{SEM}, and σ_m, it is necessary to add the noise of acoustic detecting system σ_A which is composed of thermal noise in near-field, the acoustic transmission noise, and the thermal noise of transducer. The total noise σ_{total} is:

$$\sigma_{total} = \sqrt{\sigma_G^2 + \sigma_{SEM}^2 + \sigma_m^2 + \sigma_A^2} \qquad \text{Eq.4-6}$$

The σ_{SEM} , σ_G , σ_m are known for a certain SEM system, a certain function generator, and a given lock-in amplifier. But σ_A is very difficult to evaluate and could only be decided experimentally up to now. A typical value of signal to noise ratio at frequency of 100kHz after the lock-in amplifier is 3~5 for SEAM.

There are two factors which affect the stability of SEAM by piezoelectric imaging mechanism. One is the stability of field distribution in near-field. The other is the stability of SEM. Usually the stability of SEM is given for a certain system. According to the experiment, the stability of field distribution in near-field is very sensitive to the beam current, as the thermal effect by the injecting PE has a considerable effect on the stability. Under normal conditions, if the beam current is less than 100~500 nA, there is no problem of stability caused by thermal effect.

5 Scanning Near-field Acoustic Microscopy based on SPM (SNAM)

5.1 Physical background, signal generation, and contrast mechanism

To analyze the ferroelectric properties by SPM, much work has been done and different experiment SNAM set-ups based on SPM have been developed [19~37]. Only recently, a model for the study of ferroelectric thin films by piezoelectric response mode of SNAM is presented [33, 77]. Even in that model, the electric field solutions could not satisfy the electric boundary conditions of the presented model. Neither could the introduced theoretical method be used as a systematic theoretical technique even only to analyze the quasi-stationary electric field for different samples such as bulk materials or thin films. For a systematic analysis of the electric and acoustic coupling fields in ferroelectric samples studied by SNAM systems, no other work has been documented because of the complexity. The first difficulty is that the electric and mechanical fields in the near-field in the sample is very difficult to calculate in SNAM systems [77, 78]. The second difficulty results from surfaces of ferroelectric materials which are also unknown to us. Although experiment results are presented from both piezoelectric response mode [19,33] and the system developed in this work [34, 37], an explanation of contrast of SNAM can only be qualitative, as the electric and mechanical coupling in near-field is still under study. Although there have been a lot of numerical solutions of the electric field distribution under the tip, it would be difficult to use the numerical solutions to study the contrast mechanism of SNAM systems. Therefore, a simple analytical solution of electric and mechanical coupling will be important for both the analysis of contrast mechanism and the estimation of properties of ferroelectric materials studied by SNAM systems.

As briefly discussed in the introduction, a new set-up of SNAM based on SPM for the characterization of $BaTiO_3$ material system is developed in this work. To characterize the system developed, a systematic theoretical model based on classical electromagnetic and acoustic theories for the set-up is presented in this chapter. Detailed theoretical calculations can be found in Appendix A4.

The SNAM system to be introduced in the following is developed from a commercial SPM system. The SPM works in contact mode and an alternating voltage is applied between the tip and the backside of the sample. A transducer is used to detected acoustic vibrations produced by the converse piezoelectric effect of the sample [34~37]. As briefly discussed in Chapter 3, the use of the transducer provides a solid base for a theoretical and experimental comparison of the contrast of SNAM system developed in this work to other established near-field acoustic methods, such as SEAM. Some work [19, 22, 25, 30~33] introduced the so-called piezoelectric response mode of SNAM which uses the laser signal to detect the acoustic vibrations in near-field. A comparison of results of the developed system with the results of the piezoelectric response mode is also presented later. To analyze the developed set-up systematically, some important parameters of the system should be introduced at first.

By the contact mode of SPM, the distance between the tip and the sample surface is smaller than 10 nanometer. The tip used in the SNAM has a spherical form with a curvature radius of 10 nm at the pinnacle. The ac voltage between the tip and the back electrode is usually fixed at a certain value at which the ferroelectric domains would not be affected. The transducer and sample holder are exactly the same as those used in SEAM, so that the same acoustic boundary conditions for both near-field techniques can be ensured for the complementary study discussed in Chapter 8.

The sample studied is usually anisotropic and the SNAM has complicated boundary conditions because of the conductive tip. It is impossible to obtain a simple analytic solution without certain approximations. Usually, the near-field under the tip in SNAM is usually small, and, for the analysis of quasi-stationary electric field problems, the electric anisotropic properties of the sample can be neglected. Only for the analysis of acoustic problems, the anisotropic properties must be taken into account, as the dimension of the acoustic transmission is much larger than the dimension of near-field.

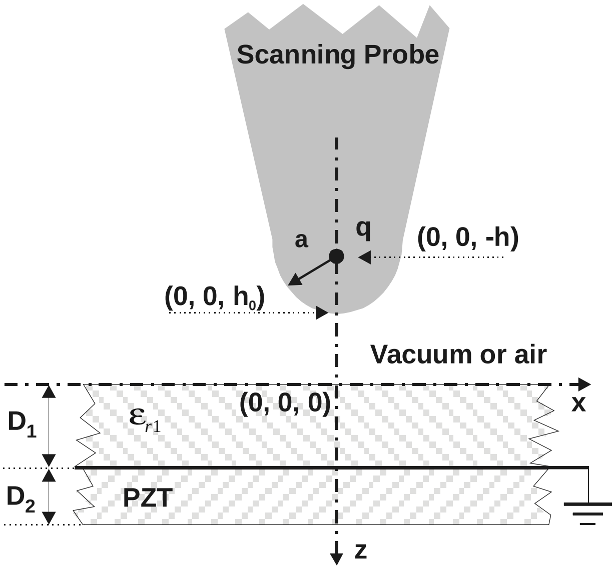

Fig.5-1: Simplified model for the set-up

The form of the tip presents another problem for the analytic solution of the electric field in SNAM. Under the microscopic view, the form of the tip is different from one another. Theoretically, the surface of the conductive tip can be equated by an infinite series of point charges, but it would be too complicated to see main physical meanings in SNAM system. As discussed in Chapter 4, the sample and the transducer in near-field microscopy system have usually a lateral dimension of 1-2 centimeter. The thickness of the bulk ceramics or crystal samples is normally 2 millimeter and a typical thin film sample 1000 nm. The scanning tip has only a diameter of 10 nm at the pinnacle. Because of this difference of the geometrical dimension between the sample and the tip, the tip can be normally simplified as a point charge which is at the curvature center of the pinnacle of the tip [33, 77, 79]. The sample and transducer, as discussed in chapter 3 for a typical near-field acoustic system, are simplified as plates with an unlimited lateral dimension. The simplified model to characterize the electric field distribution of the set-up developed in this work is shown in Fig.5-1. The approximations for SNAM system developed, as in the case of SEAM, are generalized as:

- For the calculation of quasi-stationary electric field in near-field, the anisotropic of electric property of the sample is neglected; Only by the treatment of acoustic transmission problem, the anisotropic properties of materials will be taken into account;
- The tip will be equivalent as a point charge at the curvature center of the pinnacle of the tip;
- At the pinnacle point of the tip $(0,0,\mathrm{h}_0)$, the potential will be given as the voltage of the tip, because it is the nearest point to the sample and has the strongest effect on the field distribution [77, 79].

According to the model and under the approximations above, the electric and mechanic coupling in the system can be analyzed. The analytic solution of the quasi-stationary electric field in the SNAM system developed should be a solution of the Poisson´s equation with a point source under the given boundary condition shown in Fig.5-1. The most effective way to solve this quasi-stationary field is the solution of the Green´s function of the system.

5.1.1 Green´s function of the model

The electric field distribution can be analyzed by the use of Green´s function. The field distribution of a point charge q at (0,0,-h) in cylindrical coordinate system can be obtained by separating variables as [80~82]:

$$\mathrm{V}=\frac{q}{4\pi\varepsilon_0}\int_0^\infty J_0(\beta r)e^{-\beta|z+h|}d\beta \qquad \text{Eq.5-1}$$

The Green´s function for the model shown in Fig.5-1 can be written as:

In the region $-\infty<z<0$;

$$\mathrm{V0}=\frac{q}{4\pi\varepsilon_0}\left[\int_0^\infty J_0(\beta r)e^{-\beta|z+h|}d\beta+\int_0^\infty A(\beta)J_0(\beta r)e^{\beta z}d\beta\right] \qquad \text{Eq.5-2}$$

In the region 0<z<D$_1$;

$$V1=\frac{q}{4\pi\varepsilon_0}\left[\int_0^\infty B(\beta)J_0(\beta r)e^{-\beta z}d\beta+\int_0^\infty C(\beta)J_0(\beta r)e^{\beta z}d\beta\right] \qquad \text{Eq.5-3}$$

At z = D$_1$, the metal interface is earthed, so the voltage at the interface:

$$V1=0 \qquad \text{Eq.5-4}$$

As the interface between the sample and PZT transducer is earthed, it is only necessary to characterize the electric field distribution in two regions above. By solving the boundary conditions of the system, the constants can be decided [Appendix A4.2].

The Green´s function V0 in the region of -∞<z<0 is divided into three terms:

The first term:

$$\frac{q}{4\pi\varepsilon_0}\int_0^\infty J_0(\beta r)e^{-\beta|z+h|}d\beta \qquad \text{Eq.5-4}$$

It can be treated as a point charge at (0, 0, -h)

The second term:

$$\frac{q}{4\pi\varepsilon_0}\int_0^\infty (-\eta_1)e^{-2\beta h}\frac{1}{1+\eta_1 e^{-2\beta D_1}}J_0(\beta r)e^{\beta z}d\beta$$

$$=\frac{q}{4\pi\varepsilon_0}\int_0^\infty (-\eta_1)J_0(\beta r)e^{\beta(z-h)}d\beta+\frac{q}{4\pi\varepsilon_0}\int_0^\infty \eta_1^2 J_0(\beta r)e^{\beta[z-(2D_1+h)]}d\beta$$

$$+\frac{q}{4\pi\varepsilon_0}\int_0^\infty (\eta_1^3 e^{-\beta(4D_1+h)}+...)J_0(\beta r)e^{\beta z}d\beta \qquad \text{Eq.5-5}$$

Here $\eta_1=\frac{\varepsilon_{r1}-1}{\varepsilon_{r1}+1}$.

The terms at the right side of Eq.5-5 can be treated as image charges $Q_{m0}=-\eta_1$q, $Q_{m1}=\eta_1^2$ q , ... at the position of (h, 2D$_1$+h, 4D$_1$+h,...) at z axis.

The third term:

$$\frac{q}{4\pi\varepsilon_0}\int_0^\infty (-1)e^{-\beta(2D_1+h)}\frac{1}{1+\eta_1 e^{-2\beta D_1}}J_0(\beta r)e^{\beta z}d\beta$$

$$=\frac{q}{4\pi\varepsilon_0}\int_0^\infty (-1)J_0(\beta r)e^{\beta[z-(2D_1+h)]}d\beta+\frac{q}{4\pi\varepsilon_0}\int_0^\infty \eta_1 J_0(\beta r)e^{\beta[z-(4D_1+h)]}d\beta$$

$$+\frac{q}{4\pi\varepsilon_0}\int_0^\infty [\eta_1^2\, e^{-\beta(6D_1+h)}+\ldots]\, J_0(\beta r)e^{\beta z}d\beta \qquad \text{Eq.5-6}$$

In the same way, terms at the right side of Eq.5-6 can be treated as the image charges Q_{n0} = -q, $Q_{n1}=\eta_1$ q , ... at the position of (2D$_1$+h, 4D$_1$+h,...) at z axis.

The physical meaning of the calculation above is that the Green´s function for the area above the sample in SNAM can be equivalent as the sum of potentials which are produced by a series of point image charges. The final image charge distribution for Green´s function V0 is shown in Fig.5-2.

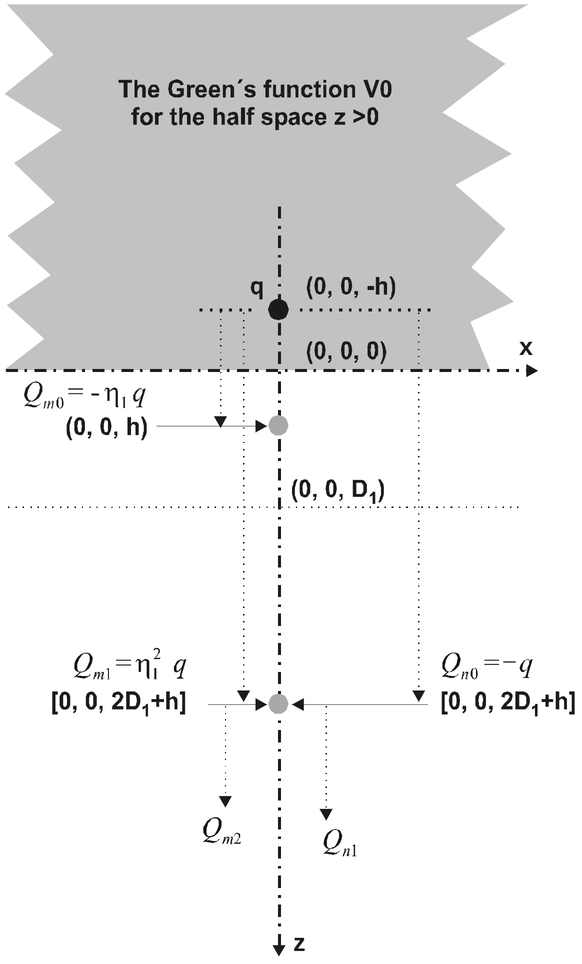

Fig.5-2: Equivalent point charges for the Green´s function in the half space z < 0

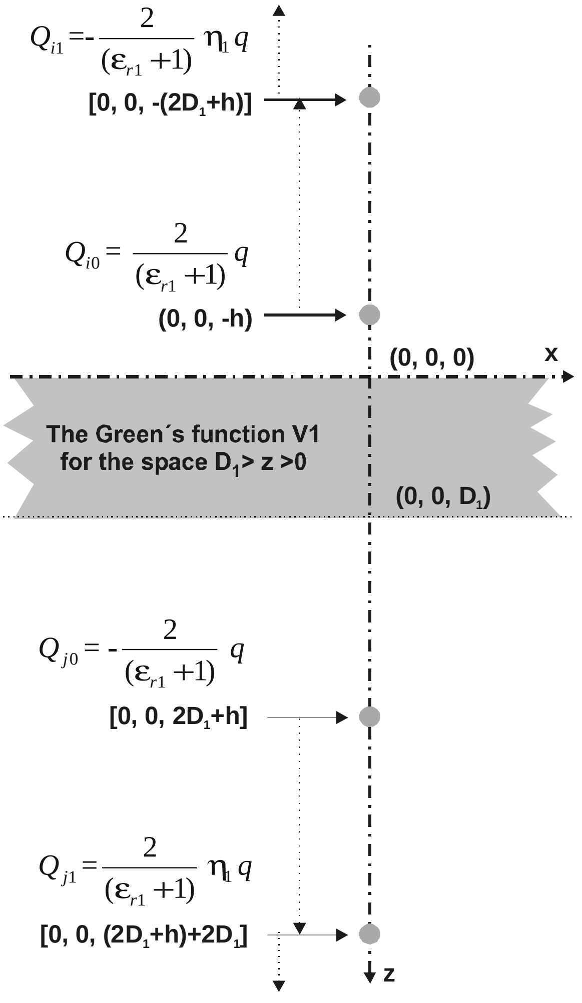

Fig.5-3: Equivalent point charges for the Green´s function in the space (D$_1$>z>0).

The Green´s function V1 in the region of D$_1$>z>0 is obtained in the same way and divided into two terms (Appendix A4.2):

The first term of V1:

$$\frac{q}{4\pi\varepsilon_0}\int_0^\infty B(\beta)J_0(\beta r)e^{-\beta z}d\beta$$

$$=\frac{q}{4\pi\varepsilon_0}\frac{2}{(\varepsilon_{r1}+1)}\int_0^\infty J_0(\beta r)e^{-\beta(z+h)}d\beta$$

$$-\frac{q}{4\pi\varepsilon_0}\frac{2}{(\varepsilon_{r1}+1)}\eta_1\int_0^\infty J_0(\beta r)e^{-\beta[z+(2D_1+h)]}d\beta$$

$$-\frac{q}{4\pi\varepsilon_0}\frac{2}{(\varepsilon_{r1}+1)}\int_0^\infty [e^{-2\beta h}\,(\eta_1\,e^{-2\beta D_1})^2 \text{-}...]\,J_0(\beta r)e^{-\beta z}d\beta \qquad \text{Eq.5-7}$$

The term at the right side of Eq.5-7 can be equivalent as image charges $Q_{i0}=\frac{2}{(\varepsilon_{r1}+1)}$ q, $Q_{i1}=-\frac{2}{(\varepsilon_{r1}+1)}\eta_1$ q, ... at the position of (-h, -(2D$_1$+h), ...) at z axis.

The second term of V1:

$$\frac{q}{4\pi\varepsilon_0}\int_0^\infty C(k)J_0(kr)e^{kz}dk$$

$$=\frac{q}{4\pi\varepsilon_0}(\text{-}1)\frac{2}{(\varepsilon_{r1}+1)}\int_0^\infty J_0(kr)e^{k[z-(h+2D_1)]}dk$$

$$+\frac{q}{4\pi\varepsilon_0}\frac{2}{(\varepsilon_{r1}+1)}\eta_1\int_0^\infty J_0(kr)e^{k[z-(h+4D_1)}dk$$

$$+\frac{q}{4\pi\varepsilon_0}\int_0^\infty [e^{-k(h+2D_1)}(\eta_1\,e^{-2kD_1})^2+...]\,J_0(kr)e^{kz}dk \qquad \text{Eq.5-8}$$

The terms at the right side of Eq.5-8 can be equivalent as image charges $Q_{j0}=-\frac{2}{(\varepsilon_{r1}+1)}$ q, $Q_{j1}=\frac{2}{(\varepsilon_{r1}+1)}\eta_1$ q, ... at the position of (2D$_1$+h, 4D$_1$+h, ...) at z axis. The image charge distribution of Green´s function V1 is shown in Fig.5-3.

5.1.2 Modeling of thick samples

The near-field area of SNAM is just beneath the sample surface. If the sample is very thick compared to the distance h (D$_1$>>h), the charge at (0,0,-h) and the image charge at (0,0,h) with charge $Q_{m0} = -\eta_1 q$ have the greatest contribution to the Green´s function of V0 in the vicinity of the tip contact area and the contribution of other image charges can be further neglected (see Fig.5-2). In the same way and under the same approximation above, the field distribution in near-field in the sample can also be calculated by the image charge at (0, 0, -h) with a charge of $Q_{i0} = \frac{2}{\varepsilon_r + 1} q$ (see Fig.5-3). The physical meaning of the approximation is that the sample is treated as an infinite half space with dielectric constant ε_r approximately.

Under the approximation above and from the Green´s function, if the rectangular Cartesian coordinate system is used for the sake of further analyses of acoustic problems, the electric potential under the approximation above can be written as:

$$\mathrm{V0} = \frac{1}{4\pi\varepsilon_0}\left(\frac{q}{\sqrt{x^2+y^2+(z+h)^2}} + \frac{Q_{m0}}{\sqrt{x^2+y^2+(z-h)^2}}\right), \text{ for } z<0 \qquad \text{Eq.5-9}$$

in which $Q_{m0} = -\eta_1$ q; Eq.5-10

$$\mathrm{V1} = \frac{1}{4\pi\varepsilon_0}\frac{Q_{i0}}{\sqrt{x^2+y^2+(z+h)^2}}, \text{ for } z>0 \qquad \text{Eq.5-11}$$

in which $Q_{i0} = \frac{2}{\varepsilon_r + 1} q$. Eq.5-12

The system capacitance can be calculated by the Green´s function above. To make the best approximation for the tip, the point $(0, 0, \mathrm{h}_0)$ at the pinnacle point of the tip will be given the voltage of Vs. The equivalent charge, as mentioned above, is at the curvature center at the pinnacle point with a curvature radius of 10 nm. The equivalent charge q:

$$q = C_{eq}\mathrm{Vs} = 4\pi\varepsilon_0 \frac{1}{(h-h_0)^{-1} - \eta_1(h+h_0)^{-1}}\mathrm{Vs} \qquad \text{Eq.5-13}$$

From Eq.5-73, the source field distribution in the sample can be written as:

$$\vec{E}_s = -\left(\frac{\partial \mathrm{V1}}{\partial x}\vec{a}_x + \frac{\partial \mathrm{V1}}{\partial y}\vec{a}_y + \frac{\partial \mathrm{V1}}{\partial z}\vec{a}_z\right)$$

The x and y and z components of $\vec{E}_s$ have the forms:

$$E_{sx} = \frac{1}{4\pi\varepsilon_0}\frac{x}{(\sqrt{x^2+y^2+(z+h)^2})^3} Q_{i0} \qquad \text{Eq.5-14}$$

$$E_{sy} = \frac{1}{4\pi\varepsilon_0} \frac{y}{(\sqrt{x^2 + y^2 + (z+h)^2})^3} Q_{i0} \qquad \text{Eq.5-15}$$

$$E_{sz} = \frac{1}{4\pi\varepsilon_0} \frac{(z+h)}{(\sqrt{x^2 + y^2 + (z+h)^2})^3} Q_{i0} \qquad \text{Eq.5-16}$$

To understand the near-field effect of the SNAM system, an estimation of electric field under the tip is necessary. The x and y components are zero in the middle of the near-field area and small in the vicinity compared to z component, so that they can be neglected for further analysis. The $BaTiO_3$ crystal has a typical value of $\varepsilon_{rzz} = 112$. In the contact mode of SPM, the distance h_0 in the model is usually smaller than 5 nm. The curvature radius at the pinnacle point is about 5 nm. From Fig.5-4, h =10 nm. With the help of free mathematical simulation program Octave 1.2, the electric field in the sample of E_{sz} for typical $BaTiO_3$ single crystal material is simulated. The simulation shows clearly that the field is concentrated itself on several h under the surface. At the depth of the material about 9h, the field is decreased to 1% of the value at the surface. Under the model above, the field is naturally proportional to the voltage if the capacitance is calculated as Eq.5-13 which is generally accepted [33, 77, 79].

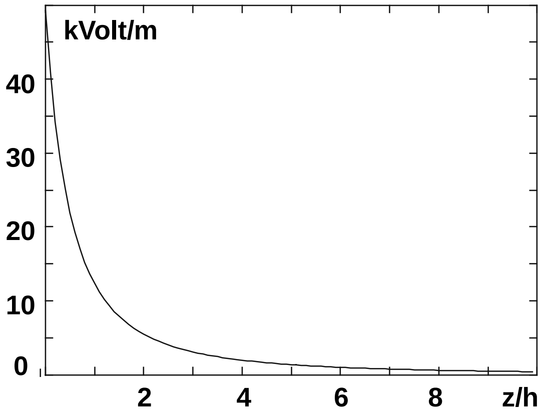

Fig.5-4a: The change of E_{sz} with depth (z/h) at the tip voltage of 1 Volt

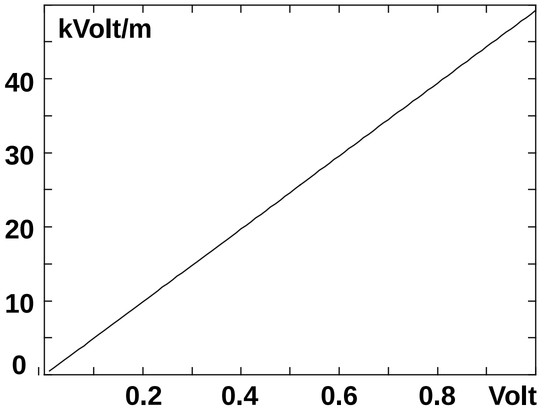

Fig.5-4b: The change of E_{sz} with the tip voltage at sample surface (z = 0)

The electric field in z direction for SNAM is:

$$E_{sz} = \frac{1}{4\pi\varepsilon_0} \frac{(z+h)}{(\sqrt{x^2 + y^2 + (z+h)^2})^3} Q_{i0} \qquad \text{Eq.5-17}$$

If the near-field approximation like that for SEAM is also made here:

- The near-field dimension in lateral direction is defined as the area where the value of the

E_{sz} at the boundary is decreased to 1/e of the value in the middle;

- Within the lateral dimension of the near-field defined above, the electric field E_{sz} is homogeneous in lateral direction and equals the field in the middle of the near-field;

Then the electric field E_s in the whole near-field area can be approximately written as:

$$E_s = E_{sz} = \frac{1}{4\pi\varepsilon_0}\frac{1}{(z+h)^2}Q_{i0} \qquad \text{Eq.5-18}$$

If the source voltage is time harmonious function with a highest frequency of several hundred kHz, it will produce a quasi-stationary electric field in the z direction. The amplitude of this quasi-stationary field is also expressed by Eq.5-18 with only a time variable $e^{j\omega t}$. By the use of transmission line mode and by solving the system acoustic equations shown in Chapter 3, the amplitude of acoustic waves in transducer in SNAM can be obtained in the same way as:

$$a^{3+}(D_1) = \frac{4jZ_0\frac{e_{z3}}{c_p}e^{-jkD_1}\int_0^{D_1}\frac{\partial E_s}{\partial t}\sin(k\zeta)d\zeta}{[1+Re^{-2jk_3D_2}][1+e^{-2jk_3D_2}]+\beta[1-Re^{-2jk_3D_2}][1-e^{-2jk_3D_2}]} \qquad \text{Eq.5-19}$$

The output signal of transducer is from Eq.3-23:

$$V_{output} = \frac{1}{2jk_3}\left(\frac{e_{z3}^{PZT}}{c_P^{PZT}\varepsilon_{zz}^{PZT}}\right)(1+\mathrm{Re}^{-2jk_3D_2})(1\text{-}e^{-jk_3D_2})\,a^{3+}(D_1) \qquad \text{Eq.5-20}$$

If the system boundary is given and the source field is kept constant during scanning, the output signal is only proportional to material constants $\frac{e_{z3}}{c_p}$ and $\int_0^{D_1}E_s\sin(k\zeta)d\zeta$. Here the term $\int_0^{D_1}E_s\sin(k\zeta)d\zeta$ must be discussed in detail to see the physical meaning of the near-field effect in SNAM. At a given point, the material properties at the point are given, the output signal of the transducer in SNAM is only proportional to $\int_0^{D_1}E_s\sin(k\zeta)d\zeta$. Because this integration has no simple form, we can only calculate the output signal of the transducer

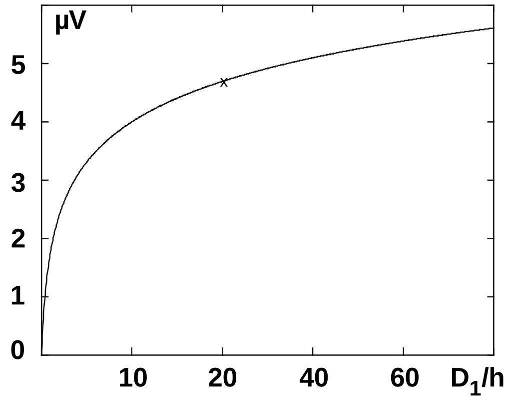

Fig.5-5: The change of output signal of the transducer with sample thickness D_1

through the Octave mathematical program. The output signal of the transducer at a certain frequency (f=100kHz) with the change of thickness of the sample is shown in Fig.5-5. It is clear that, after $D_1 = 20h$, the signal changes very slowly and reaches almost the final value. That means that the contrast of SNAM comes from the surface layer in the range from the surface to several hundred nanometer deep. The reason is that most of the source electric field in the model is concentrated in this area because of the form of the tip, as shown in Fig.5-4a.

After the discussion of near-field area in the thick sample, the contrast of ferroelectric domains can be explained in the same way as in the case of SEAM. If the extrinsic contribution of the domain walls to the piezoelectric effect in ferroelectric materials is neglected, the constants of e_{z3} (or d_{z3}) is directly related to ferroelectric polarization [see Eq.2-24]. If there are two areas of c- and a-domains on the surface of $BaTiO_3$ materials, the area of c-domains has polarization in the z direction and has a non-zero value of e_{z3} in near-field. When the scanning tip is on this area, the output signal of the transducer has a certain value. Whereas the area of a-domains, which has a polarization perpendicular to the z direction, will have zero value of e_{z3}. When the tip is on this a-domain area, the output signal of the transducer, will have a zero value (or more accurately, very small value). As the amplitude signal is used as the imaging signal, the c-domain will appear bright and a-domain will appear black in acoustic image of SNAM system. This is the contrast mechanism of SNAM on ferroelectric $BaTiO_3$ single crystals. Here we must notice that the near-field dimension is much smaller than that of SEAM.

5.1.3 Modeling of thin samples or films

If the sample is not so thick compared to the distance h ($D_1 \cong h$), or the sample is a ferroelectric thin film which usually has a thickness of several hundreds to several thousands nanometers, the condition $D_1 >> h$ is not satisfied in this case. According to the Green´s function of Eq.5-4 to Eq.5-8, the electric fields above the sample and in the sample are dependent on series of image charges. The final field distribution is the sum of field contributions from every single image point charge. How many image charges should be used to decide the Green´s function of the system, is naturally dependent on the thickness of the sample and the accuracy of the calculation. The typical thin film studied in this work has a thickness of 1 μm and the distance of h is 10 nm. For this typical thin film system with the first order of approximation, only the field contribution of the image point charges at the distance to the surface in the range of $(2D_1+h)$ will be considered. The contribution of other image charges at the distance outside this range is assumed so small that the contribution can be neglected.

Under the approximation above and according to the Green´s function discussed above, the Green´s function V0 is constructed by q at position of (0, 0, -h), $Q_{m0}=-\eta_1 q$ at (0, 0, h), $Q_{m1}=-\eta_1^2 q$ and $Q_{n0}=-q$ at $(0,0,2\mathrm{D}_1+\mathrm{h})$. The Green´s function V1 (see. Fig. A3) can be constructed by charges of $Q_{i0}=\frac{2}{\varepsilon_{r1}+1}q$ at position of $(0,0,\mathrm{h})$, $Q_{i1}=\frac{2}{\varepsilon_{r1}+1}\eta_1 q$ at position $[0,0,-(2\mathrm{D}_1+\mathrm{h})]$, and $Q_{j0}=-\frac{2}{\varepsilon_{r1}+1}q$ at $[0,0,(2\mathrm{D}_1+\mathrm{h})]$.

If the rectangular Cartesian coordinate system is used for the sake of simplicity of further analyses of acoustic problems, the Green´s functions for thin film under the condition above can be written as:

$$\mathrm{V0}=\frac{1}{4\pi\varepsilon_0}\left(\frac{q}{\sqrt{x^2+y^2+(z+h)^2}}+\frac{Q_{m0}}{\sqrt{x^2+y^2+(z-h)^2}}+\right.$$

$$\left.\frac{Q_{m1}}{\sqrt{x^2+y^2+[z-(2D_1+h)]^2}}+\frac{Q_{n0}}{\sqrt{x^2+y^2+[z-(2D_1+h)]^2}}\right),\ \text{for } z<0$$

Eq.5-21

$$\mathrm{V1}=\frac{1}{4\pi\varepsilon_0}\left(\frac{Q_{i0}}{\sqrt{x^2+y^2+(z+h)^2}}+\frac{Q_{i1}}{\sqrt{x^2+y^2+[z+(2D_1+h)]^2}}\right.$$

$$\left.+\frac{Q_{j0}}{\sqrt{x^2+y^2+[z-(2D_1+h)]^2}}\right),\ \text{for } 0<\mathrm{z}<\mathrm{D}_1$$

Eq.5-22

The system capacitance can be calculated in the same way. With the source Vs, the equivalent charge q is:

$$q=C_{eq}\mathrm{Vs}=4\pi\varepsilon_0\frac{1}{(h-h_0)^{-1}-\eta_1(h+h_0)^{-1}-(1-\eta_1^2)[2D_1+h+h_0]^{-1}}\mathrm{Vs}$$

Eq.5-23

The field distribution in the sample can be obtained as:

$$\vec{E}_s=-\left(\frac{\partial\,\mathrm{V1}}{\partial x}\vec{a}_x+\frac{\partial\,\mathrm{V1}}{\partial x}\vec{a}_y+\frac{\partial\,\mathrm{V1}}{\partial x}\vec{a}_z\right)$$

$$E_{sx}=\frac{1}{4\pi\varepsilon_0}\left(\frac{x}{(\sqrt{x^2+y^2+(z+h)^2})^3}Q_{i0}+\frac{x}{(\sqrt{x^2+y^2+[z+(2D_1+h)]^2})^3}Q_{i1}\right.$$

$$+\frac{x}{(\sqrt{x^2+y^2+[z-(2D_1+h)]^2})^3}Q_{j0} \qquad \text{Eq.5-24}$$

$$E_{sy}=\frac{1}{4\pi\varepsilon_0}(\frac{y}{(\sqrt{x^2+y^2+(z+h)^2})^3}Q_{i0}+\frac{y}{(\sqrt{x^2+y^2+[z+(2D_1+h)]^2})^3}Q_{i1}$$

$$+\frac{y}{(\sqrt{x^2+y^2+[z-(2D_1+h)]^2})^3}Q_{j0} \qquad \text{Eq.5-25}$$

$$E_{sz}=\frac{1}{4\pi\varepsilon_0}(\frac{(z+h)}{(\sqrt{x^2+y^2+(z+h)^2})^3}Q_{i0}+\frac{z+(2D_1+h)}{(\sqrt{x^2+y^2+[z+(2D_1+h)]^2})^3}Q_{i1}$$

$$+\frac{z-(2D_1+h)}{(\sqrt{x^2+y^2+[z-(2D_1+h)]^2})^3}Q_{j0} \qquad \text{Eq.5-26}$$

If the near-field approximation like that of SEAM is also made here:

- The near-field dimension in lateral direction is defined as the area where the value of the E_z at the boundary is decreased to 1/e of the value in the middle;
- Within the lateral dimension of the near-field defined above, the electric field E_z is homogeneous in lateral direction and equals the field in the middle of the near-field;

Then the electric field in the whole near-field can be approximately written as:

$$E_s=E_{sz}=\frac{1}{4\pi\varepsilon_0}(\frac{1}{(z+h)^2}Q_{i0}+\frac{1}{[z+(2D_1+h)]^2}Q_{i1}-\frac{1}{[z-(2D_1+h)]^2}Q_{j0})$$

Eq.5-27

in which $Q_{i0}=\frac{2}{\varepsilon_{r1}+1}q$, $Q_{i1}=\frac{2}{\varepsilon_{r1}+1}\eta_1 q$, and $Q_{j0}=-\frac{2}{\varepsilon_{r1}+1}q$.

The output signal of the transducer can also be obtained by Eq.5-19 and Eq.5-20. It must be noted that, if the thickness of the film is D_1=1 µm, the electric field in z direction in near-field has little change according to Eq.5-27 as the last two terms in Eq.5-27 are much smaller than the first one. That means that the two image charges Q_{i1} and Q_{j0} have so small an effect to the electric field distribution in the near-field that the effect can be neglected as well. Only if the thickness of the film is comparable to the parameter h, the field distribution should be estimated according to different order of approximation to the Green´s function Eq.5-4 and Eq.5-8, and finally the equivalent image charges can be decided.

5.2 Experiment set-up

The developed SNAM system is shown in Fig.5-6 if the switch is turned to position (a). The SPM system is a topometrix Explorer. The tip used is the electric conductive tip of the Company Nanosensors [83]. The transducer and sample holder are the same as those used in SEAM discussed in Chapter 4.

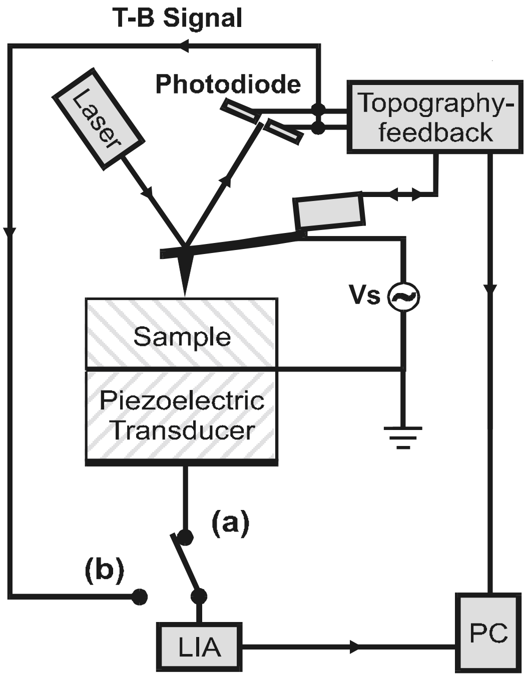

Fig.5-6: Set-up of SNAM with a transducer (a) and of piezoelectric response mode (b)

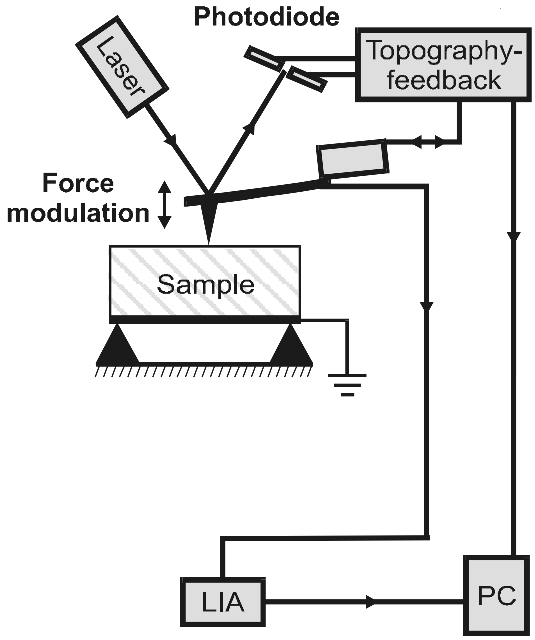

Fig.5-7: Set-up of SNAM with force modulation

By the use of a transducer, it is also possible to compare the direct and converse piezoelectric effect in near-field. The set-up to check the direct piezoelectric effect is shown in Fig.5-7. The tip is modulated and the contact force between the tip and the surface of the sample is modulated as well. This modulated force will act as a point stress source on the sample surface and produce different acoustic waves in the sample among which there are acoustic longitudinal waves transmitted in z direction. According to the discussion of the electric and acoustic coupling presented in Chapter 3, because the sample of $BaTiO_3$ is piezoelectric, the acoustic longitudinal plane waves will produce a coupled quasi-stationary electric field in the sample. This coupled field can be imaged by measuring the voltage between the conductive tip and the bottom side of the sample, if the tip and the sample can be well shielded from other disturbance signals, such as the disturbance signal from the PZT actuator in SPM. It means that it is theoretically possible to image the direct piezoelectric effect in this way. The set-up of Fig.5-6 at the switch position (a) can measure the converse piezoelectric effect. By comparison of the set-up of Fig.5-7 with the set-up of Fig.5-6 at the switch position (a), it is theoretically possible to compare direct and converse piezoelectric effect in near-field. One of the results is shown in Fig.7-5.

The so-called piezoresponse mode of SPM [19,22,25,30~33] is based on such a principle: An ac voltage is also applied between the conductive tip and the backside of the sample to produce the vibration in near-field of ferroelectric samples. As the tip is in contact with the sample surface, the near-field vibrations transmit also to the cantilever and the laser beam is modulated by the vibration. The photodiodes in SPM demodulate the laser signal and form the so-called T-B-signal, which is the difference of signals obtained from top and bottom diode sections of a quadrant detector. It carries the information of vibrations in near-field. By detecting the T-B signal, the information in near-field can be detected indirectly, as shown in Fig.5-6 with switch to (b). The tip used is a commercial electrical conducting tip. The ac voltage V_s used must be so small that the ferroelectric domains will not be affected.

In order to compare contrast between the set-up developed in this work and the piezoelectric response mode, the same sample at the same environment is also imaged by both techniques and the results are shown in Fig.7-8. Both of the two methods are proved to be able to image ferroelectric domains in $BaTiO_3$ materials [37]. Theoretically, for the study of ferroelectric domains, both methods can be used principally. For the contrast comparison among different near-field acoustic microscopy techniques, as it is done in this work, the system developed in this work is advantageous, as the use of the transducer provide a unique base of the same acoustic boundary condition so that the same acoustic treatment can be used. Because the piezoelectric response mode of SPM uses laser signal to detect the acoustic vibrations on the cantilever of the tip and the cantilever has a very complicated vibration transmission function [84], it would be very difficult to compare the contrast of this technique with other established near-field techniques quantitatively. However, the piezoelectric response mode would be very advantageous to study the thermal dynamic behavior of ferroelectric domains, as the thermal drift of acoustic properties of the transducer can be avoided. In this work, for the dynamic study of ferroelectric domains in $BaTiO_3$, both methods are used to image the ferroelectric domains at given areas at first, and then the second method is used at the same areas to study the same ferroelectric domains dynamically.

The principle of dynamic study is shown in Fig.5-8. For thermal dynamic study, a thermal element is used to raise the temperature of the sample and a temperature sensor is used to check the temperature of the sample surface. At different temperature points, the ferroelectric domain are imaged. For electric dynamic study, a bias dc voltage V is added to the source ac

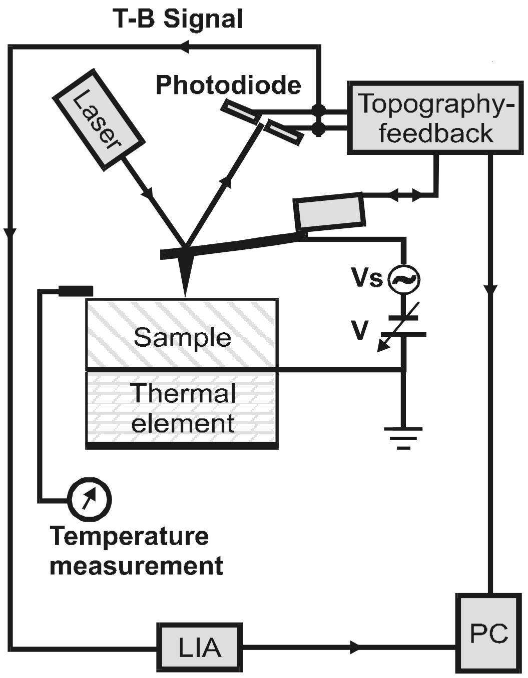

Fig.5-8: Set-up of SNAM for dynamic study

voltage V_s. This bias dc voltage will add a bias static electric field in near-field besides the quasi-stationary field. By changing the bias dc voltage, the change of domains at different bias field can be imaged dynamically [37].

5.3 Discussion of the signal and noise in SNAM developed

As the SNAM is mainly used as an imaging technique, spatial resolutions play an important role. As discussed above, both the lateral resolution and depth penetration of SNAM are decided by the parameter h which is the distance of the equivalent charge of the tip to the surface. From the approximation in this work, this distance is about 10 nm. According to the assumption of near-field for SNAM above, the lateral dimension of the defined near-field can be calculated theoretically according to the field distribution Eq. 5-17. At the surface $z = 0$, the dimension of near-field in lateral direction has a radius of $h\sqrt{e^3 - 1} \approx 4.3$h nm. That means the lateral resolution of the SNAM developed can reach 86 nm, which is verified by the experiment results very well [36, 37]. The depth of imaging would be the integration of the electric field in z direction in near-field for thick samples and, according to Eq.5-20 and Fig.5-5, the depth of imaging by SNAM on thick bulk $BaTiO_3$ sample is about 200 nm.

The imaging time of the system is mainly dependent on the scanning speed of SPM. In order to get a good topography, the scanning speed is usually slow, smaller than 1200 pixel/second. For an image of 400X400 pixel, it takes about 1~2 minutes to take a picture.

The signal to noise ratio can also be estimated. Like in the case of SEAM, If the noise from function generator, SPM, and the measuring circuit and lock-in amplifier are σ_G, σ_{SPM}, and σ_m, it is necessary to add the signal to noise ratio of acoustic detecting system σ_A which is composed of the acoustic transmission noise and the thermal noise of transducer. The total noise σ_{total} is:

$$\sigma_{total} = \sqrt{\sigma_G^2 + \sigma_{SPM}^2 + \sigma_m^2 + \sigma_A^2} \qquad \text{Eq.5-28}$$

The σ_G, σ_{SEM}, σ_m are given for a certain SEM system. Principally, because there is no thermal noise in the near-field of σ_A compared to SEAM, the signal to noise ratio of SNAM would be much better than that SEAM. But σ_A is also very difficult to evaluate and can only be decided experimentally. According to our experiments, typical values of signal to noise ratio of the acoustic signal imaged after the lock-in amplifier can be measured by the line measurement of the software of SPM. At 100 kHz, a typical value is in the range of 7~10 [36]. It can be expected that the contrast of SNAM acoustic images would be better than that of SEAM under the same experiment condition.

6 Experiment procedure

6.1 Description of Specimen

As it is explained in chapter 2, ferroelectric $BaTiO_3$ materials has the typical a- and c- domain structures. $BaTiO_3$ ceramics samples AC0 was fabricated by the Institut für Anorganische Chemie, Martin-Luther-Universität Halle-Wittenberg. One of a sample of single crystal for SEAM study was provided by Lab. of function ceramics, Shanghai Institute of ceramics. The single crystal sample for SNAM study was provided by Department of Applied Physics, University of Electronic Science and Technology of China. The film sample for the SEAM study was provided by Institut für Schicht- und Ionentechnik (ISI), Forschungszentrum Jülich, Germany. The other $BaTiO_3$ film was provided by Max-Planck-Institut für Mikrostruktur-physik, Germany. All the samples had crude surface and no treatment was required for both SEAM and SNAM studies. The ceramics sample AC0 was sintered with excess 1 % mol of TiO_2 and had an average grain size from 10 to 50 micrometer [86].

6.2 Specimen preparation and treatment

As both techniques, SEAM and SNAM, are nondestructive techniques, the surface of a sample needs no handling and treatment. In order to study the same area of a sample with two kinds of microscopy techniques, it is necessary that the surface topography and the other properties of the sample be kept unchanged during the study. Furthermore, to make the comparison study of two microscopes, the same sample must be studied in one of the microscope, then be moved to the other microscope. As the area studied is usually smaller than 100 micrometer and the samples have almost no peculiar surface characters, it results in a very difficult task to find the same area after the change of microscopes. For SEAM, in order to avoid the charge effect, a thin gold layer of about 10 to 50 nanometer is usually coated on the surface of the sample.

To solve the problems above, the SEAM experiment is arranged at first. There are two advantages to do so. Firstly, the SEAM is a relative stable and established technique. Although it has a resolution of micrometers, its large scan range, which can reach several hundred micrometers, provides a useful way to image the ferroelectric domains broadly. Secondly, by the use of the strong interaction between the sample and electron beam, it is possible to make some surface characters, such as orientation lines outside the studied area, so that the same area can be located precisely for the later SNAM experiment.

There is but one problem with this procedure. For SEAM, to avoid the surface charge effect and thermal energy accumulation at every scan point, it is usually better to make a thin gold layer on the surface of the sample. For the later SNAM experiment, the surface must be kept as clean as possible. To solve this problem, the sample surface is exposed to wax vapor for several seconds before it is coated with gold for SEAM study. The accurate thickness of wax layer is difficult to estimate but SPM study on the sample surface showed there is no obvious topography change before and after the wax layer. In this way, it is effective to make the surface free from gold layer after SEAM study.

6.3 Schemes of measurements

6.3.1 Choice of frequency

As theoretically shown in Chapter 3, the acoustic near-field techniques have usually a strong frequency dependence. It is always important for both techniques to select a right frequency to get the contrast which resulted from the interaction in near-field. The usual experiment procedure is to adjust other experiment parameters to the best state at first. With the line scanning of the control software for SEAM and SNAM, the output signal can be analyzed line by line. By changing working frequency of the signal generator, one can get the best contrast at a certain frequency and the images can finally be recorded. This is the most effective way to find the right acoustic contrast from near-field.

6.3.2 Amplitude and phase imaging

In most modern lock-in amplifiers, it is possible to obtain the amplitude and phase signal. Both amplitude and phase signal, as shown in Chapter 3, are theoretically dependent on the near-field interaction and detecting system. If a right frequency is chosen, the output signal of the transducer is solely dependent on the interaction of the material with the stimulation source in near-field.

6.3.3 Variation of parameters

If the system is optimized, the dependence of the output signal can be recorded with different parameters, such as the frequency dependence, change of the signal with the source, and so on [38]. Whereas the change of parameters is relative easy in SNAM based on SPM, the change of parameters in SEAM is relatively difficult, as the SEM is relative complicated and the change of one parameter will sometimes affects other parameters slightly. This change will result in contrast deterioration and should therefore be avoided during experiments.

6.3.4 Dynamic imaging

For dynamic experiments, it is also necessary to carry out an experiment until all the experimental parameters are stable. It is especially difficult for thermal experiments, because ferroelectric samples usually have a poor thermal conductivity. Whereas the thermal effect from the environment can be neglected in the vacuum chamber of SEAM, the thermal effect from the air environment of SNAM is an important factor for thermal dynamic experiments. One effective way to solve this problem is to wait so long a time until experimental parameters such as the temperatures of the sample and the environment near the sample are stabilized. A thermal isolation of SPM system in a vacuum chamber is also an effective way to keep the results from external thermal disturbances.

7 Results

This chapter shows some typical results by SEAM and SNAM and some explanation respectively. The results of complementary study of ferroelectric domains by both techniques as well as the discussion will be presented in Chapter 8.

7.1 Single crystal

A single crystal of $BaTiO_3$ (from Shanghai Institute of Ceramics, P. R. of China) is imaged by the SEAM [38]. Another single crystal of $BaTiO_3$ (from University of Electric Science and Technology of China) imaged by SNAM technique and shown in Fig.7-2. The ferroelectric domain contrast, which is totally different from topography, exists only in acoustic images.

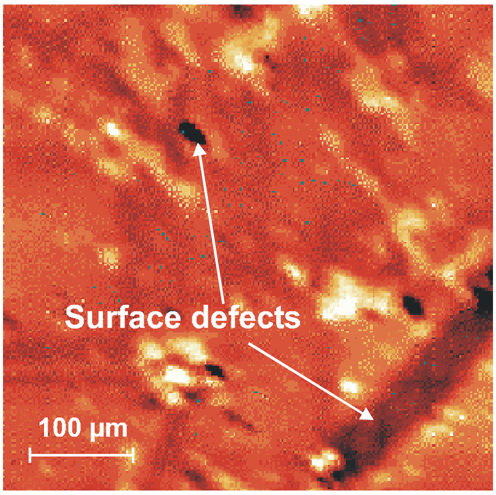

Fig. 7-1a: SEI of one single $BaTiO_3$ crystal

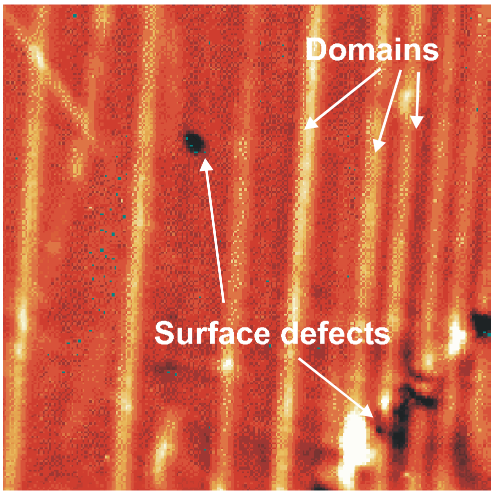

Fig.7-1b: The *in situ* EAI of the crystal

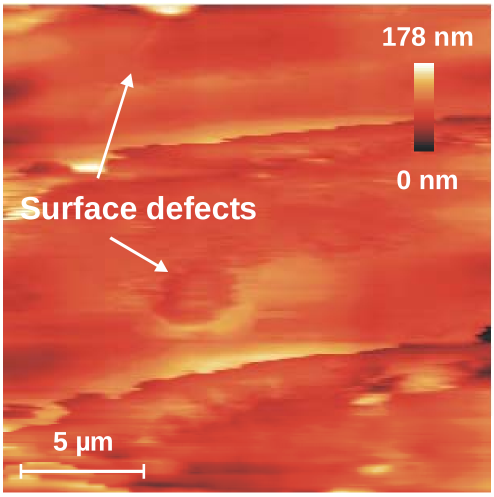

Fig. 7-2a: Topography of one single $BaTiO_3$ crystal by SPM

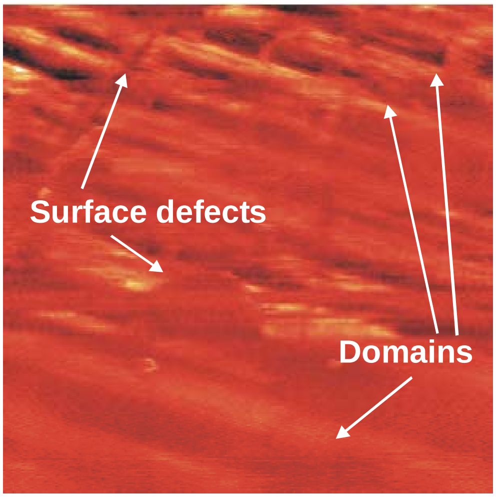

Fig.7-2b: The *in situ* acoustic image by SNAM

7.2 Ceramics

Ferroelectric $BaTiO_3$ ceramics are also imaged by both kind of techniques. One kind of ferroelectric domains structure of $BaTiO_3$ ceramics (from Martin-Luther-Uiversität Halle-Wittenberg, Germany) are imaged by SEAM and results shown in Fig.7-3 [35, 36, 37]. The same sample is also imaged by SNAM and results shown in Fig.7-4 [36, 37].

From Fig.7-3, the surface defects are visible in both SE image and EA image. Domain structures are imaged only in acoustic image. From Fig.7-4, there are only domain structures of the ceramics in acoustic image by SNAM as well. By comparison of both acoustic images on the same ceramics, it can be seen that the domain structures of the ceramics are imaged principally the same by both techniques. The contrasts have the typical stripe structures of laminated ferroelectric domains of $BaTiO_3$. But there is a difference between the acoustic

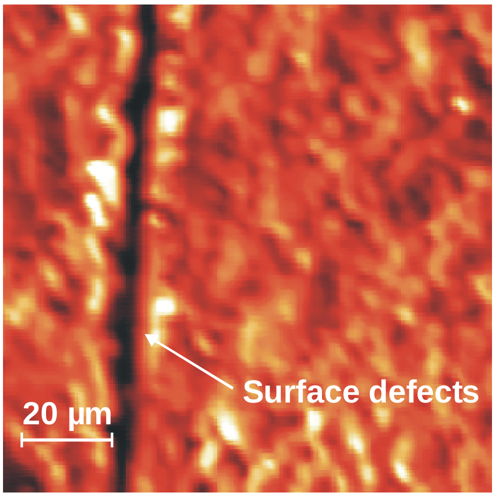

Fig. 7-3a: SEI of one $BaTiO_3$ ceramics

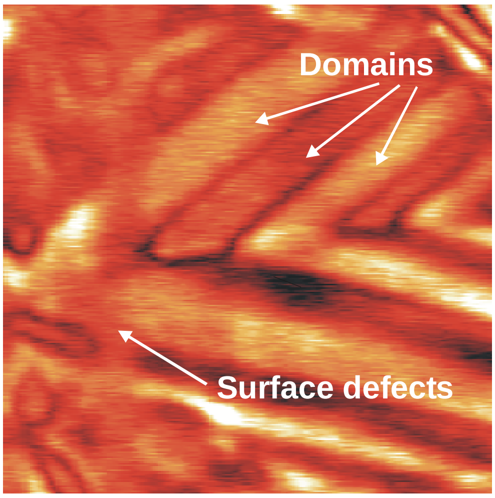

Fig.7-3b: The *in situ* EAI of the ceramics

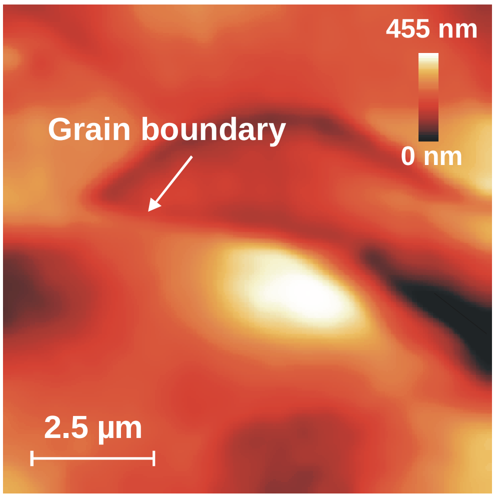

Fig. 7-4a: Topography of the same $BaTiO_3$ ceramics by SPM

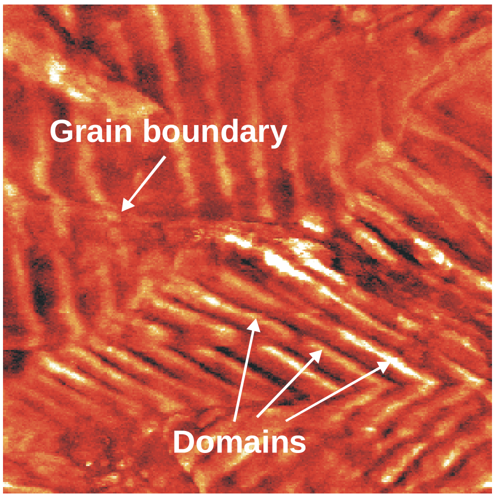

Fig.7-4b: The in situ acoustic image of the ceramics by SNAM

contrasts of both techniques. At first, the acoustic contrasts from both techniques have different widths. The SEAM show the bright stripes of about 10 µm wide. The SNAM shows the bright stripes with widths of several hundred nanometer. Further, the contrast of black stripes in SEAM acoustic image is very narrow and the boundaries between the bright and dark contrast is not clear. In acoustic image obtained by SNAM, there are clear periods between the good periodical arrayed bright or dark structures at the area studied. The boundaries between the bright and dark stripes are also clear.

Furthermore, as discussed in ‘Experimental set-up’ of SNAM in Chapter 5, if the electric field distribution in near-field is scattered by defects, the main contrast of SNAM will be dominated by the defects. As shown in Fig.7-5, the defects at subsurface of one kind of ceramics (from Shanghai Institute of Ceramics) can be shown by the check of direct and converse piezoelectric response by SNAM [34, 35]. It must be noted that two kinds of ceramics are imaged with the same SNAM technique but the acoustic images have a totally different contrast (Fig.7-4b and Fig.7-5a). The same phenomena are also observed from other ceramics. Why is there such a great difference between the acoustic images with the same SNAM technique? It is still a question which requires further study. According to the model presented in Chapter 3, the domain contrast can be explained only under two conditions: One is that the external piezoelectric effect resulted from domain wall movements are neglected (see Eq.2-28 and Eq.2-29); The other is that the source electric field is concentrated in near-field and the materials in near-field is homogenous (see chapter 3). Only under such conditions can the 90° domain structures be imaged clearly by SNAM and explained by the model of near-field acoustics. If there are defects in the sample, such as air bubbles, structure fractures, and mismatches of crystal lattice, which exist frequently in ceramics, these defects will scatter the field distribution of source electric field as well as change electric and piezoelectric properties in near-field in the sample. As a result, the contrast of acoustic images will be affected by these defects and will be the sum of all the effects, such as field scattering, inhomogeneity of piezoelectric effect, and inhomogeneity of elastic and electric properties. A clear domain contrast by SNAM could not be possible in this case, as shown in Fig.7-5a. It is classified roughly as inhomogeneity [34]. Some similar results are also reported by SEAM techniques [89]. If, however, a ceramics is highly homogeneous and has a very good ferroelectric properties, the ferroelectric domains can be imaged by SNAM clearly, as shown in Fig.5-4b. Because there are few literatures for the discussion of all these defects of ceramics in micro- or nanometer range, a complete explanation for the defects imaged could not be reached yet.

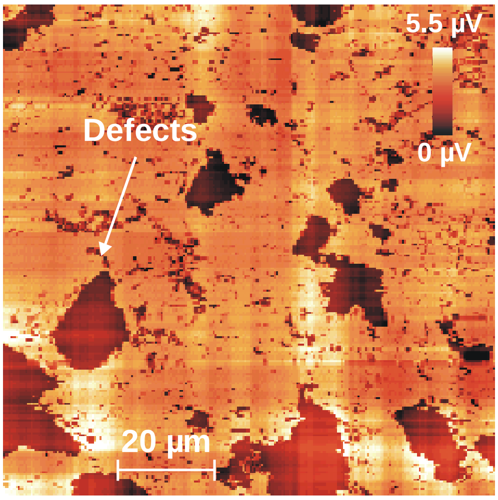

Fig.7-5a: The acoustic image by an ac voltage between the tip and the bottom of the sample.

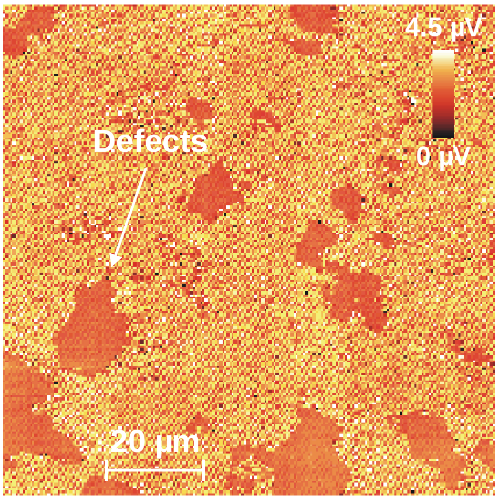

Fig.7-5b: The voltage image by an modulated force between the tip and the sample surface.

7.3 Films

Ferroelectric films (Forschungszentrum Julich, Germany) are also studied by SEAM. The thickness of the film was about 1 µm and the substrate material was MgO_2 which is not ferroelectric. The substrate had a thickness of 1 millimeter. The accelerating voltage of the primary electrons used was 20 kV. The typical results are shown in Fig.7-6 [35]. The defects exist in both SEI and EAI, but there is some acoustic contrast which is not the same as the secondary electron contrast. As the 20 keV for PE was used and the thermal diffusion depth is about 2~3 µm in the sample, the acoustic contrast could contain both the information of ferroelectric polarization and the thermal diffusion. As little work on ferroelectric thin films is documented in present literatures, there is no concrete evidence about the contrast mechanism up to now. By comparison of the $BaTiO_3$ film thickness and the thermal diffusion depth, it could be possible that the thermal mechanism could play a main role for this acoustic contrast. Therefore the contrast would be simply referred to the inhomogeneity of stress in this work. A clear explanation of the contrast mechanism needs to be studied further.

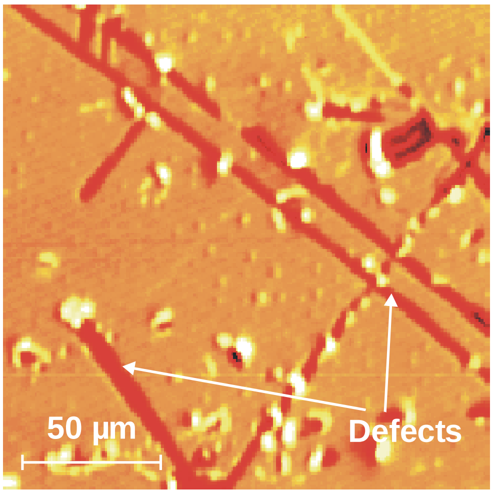

Fig.7-6a: SEI of one BaTiO$_3$ film

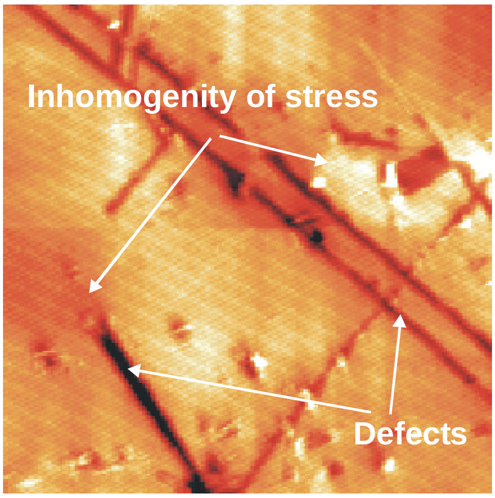

Fig.7-6b:The in situ EAI of the film at f=127 kHz

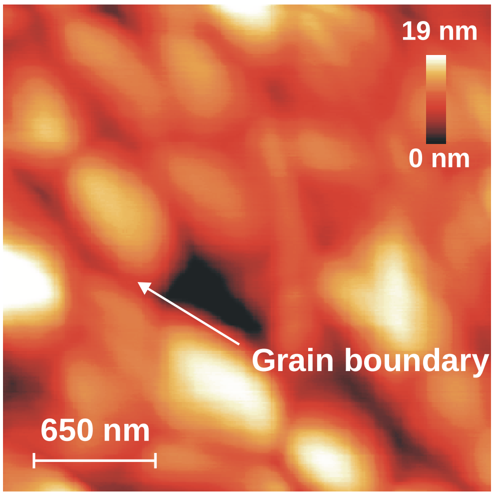

Fig.7-7a: Topography of one BaTiO$_3$ film by SPM

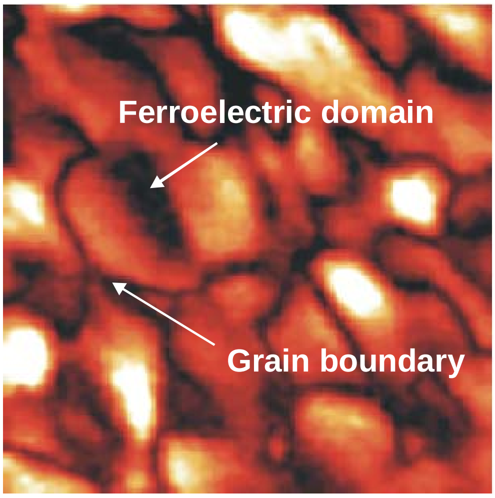

Fig.7-7b:The in situ acoustic image of the film by SNAM at f=89 kHz

Another ferroelectric BaBi$_4$Ti$_4$O$_{15}$ thin film (Max-Plank-Institut für Mikrostruckturphysik, Halle, Germany) is imaged by the SNAM. The film is 1 µm thick and the substrate material is the conductive LNO [32]. The typical results are shown in Fig.7-7. There is acoustic contrast on one grain whose boundary is shown by an arrow. The same contrast is also presented by other work with piezoelectric response mode of SNAM and the contrast is classified as domains on one grain of the film [32].

7.4 The image mode comparison of SNAM

To compare the image contrast of the set-up developed in this work with other SPM based techniques, the same structure of the same sample is studied by both the developed SNAM technique and the piezoresponse mode of SPM. As described in Chapter 5, although this mode of SPM has a complicated transmission function of the cantilever in SPM [84] and is not ideal to compare the contrast between different acoustic near-field techniques, this experimental set-up provides a better thermal dynamic image possibility than the SNAM set-up developed in this work, as the laser detection system, if the experiment time is not so long, will not be affected by the thermal conduction in the sample and thermal element. To evaluate both techniques, a comparison of contrast on the same structures with the same experiment environment between the developed SNAM technique and the piezoresponse mode is studied and only acoustic images are shown in Fig.7-8. The studied area is about the same as that shown in Fig.7-4. The grain boundary and ferroelectric domain structures are imaged in Fig.7-8 with the same contrast at a certain frequency (f=131.1 kHz).

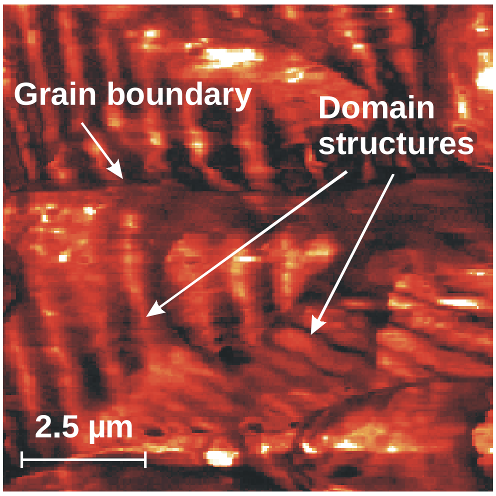

Fig.7-8a: acoustic image by SNAM with a transducer of the $BaTiO_3$ ceramics

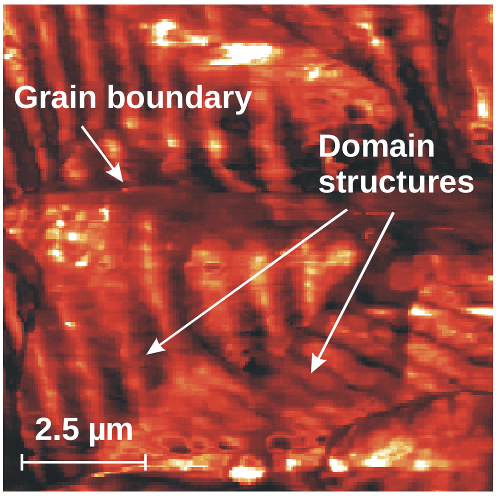

Fig.7-8b: acoustic image by piezoresponse mode at the identical area as Fig.7-8a

7.5 Dynamic study of ferroelectric domain structures

To study the temporal stability of domains of $BaTiO_3$, one $BaTiO_3$ ceramics sample (from Martin-Luther-Uiversität Halle-Wittenberg, Germany) was imaged by SNAM developed in this work in 1998 and the acoustic image is shown in Fig.7-9a [36]. After two years, the same structures at the same area were imaged once more and the acoustic image is shown in Fig.7-9b [37]. The grain boundary in both images can be seen clearly. The triangles in both images are used as a sign to identify the same structures. It is shown clearly that the domain structures have almost no change for two years. It implies also that the ferroelectric domains of the ceramics studied are very stable.

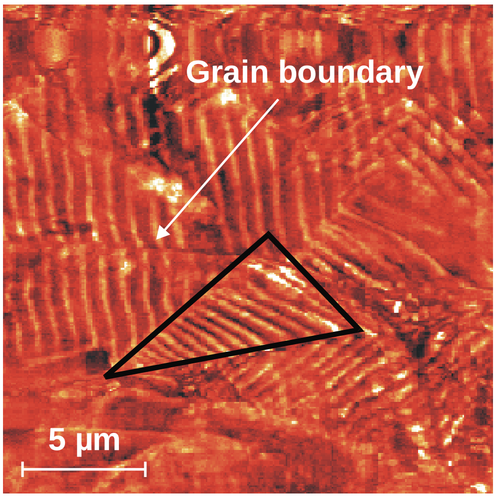

Fig.7-9a: ferroelectric domain structure imaged by SNAM in 1998

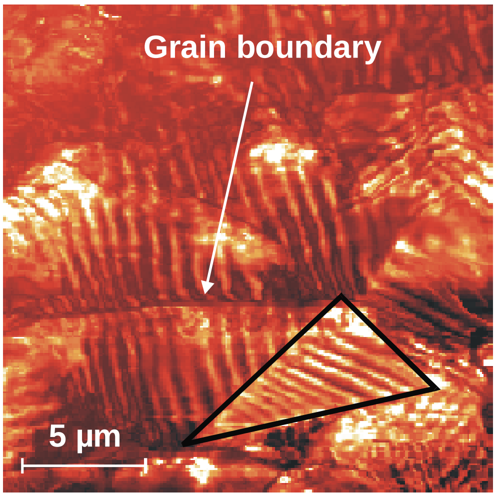

Fig.7-9b: The same structure imaged by SNAM in 2000

To study the thermal property of ferroelectric domains of the $BaTiO_3$ ceramics, the same sample is thermally heated over 130 °C, the Curie temperature of $BaTiO_3$, and then the sample is cooled down to room temperature. The ferroelectric domain structures at the identical area, as shown in Fig.7-9a and Fig.7-9b, was imaged by the developed SNAM system once more after the thermal treatment. The acoustic image is shown in Fig.7-10 [37]. By comparison of the Fig.7-10 and Fig.7-9, it is clear that some structures at certain places remained the same, as shown in the triangle. But some changed, as shown by arrows. It can be explained that the thermal treatment changed the internal energy of the ceramics. When the sample was heated over the Curie temperature, the symmetry of the sample was changed to cubic and the internal energy was changed. When the sample was cooled down from Curie temperature to room temperature, the ferroelectric polarization would change the polarization in such a way that the internal energy had a minimum under the existed thermal, elastic, and electric boundary conditions. The boundary conditions under which the sample was cooled down were different from those when the domain structures in Fig.7-9 had

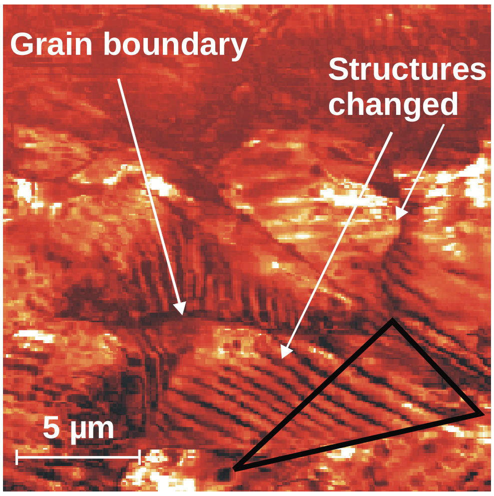

Fig.7-10: The structure at the same area after the thermal treatment

been established, so that some domain structures must change their distribution to ensure the internal energy had a minimum value. Therefore, some areas had new structures shown by arrows and some areas had no change of structures shown by the triangular in Fig.7-10.

To study ferroelectric domain structures near the Curie temperature, the same structures are imaged by dynamic set-up of SNAM developed from piezoresponse mode by the use of a thermal element and a temperature control unit. The experiment set-up is shown in Fig.5-8. The acoustic images at different temperatures are shown in Fig.7-11. The studied area is the same as that studied above. All the images in Fig.7-11 have the same dimension of 20 µm at the same area and the grain boundary, which is not changed during the thermal dynamic imaging, can be seen clearly from Fig.7-11b to Fig.7-11f. Therefore, the µ-bar to show the dimension of the images and the arrow to show the grain boundary are only noted in the first acoustic image Fig.7-11a.

When the sample was heated gradually from room temperature to Curie temperature of $BaTiO_3$ ceramics (130°C), the domain structures disappeared gradually, as shown from Fig.7-11a to Fig.7-11d. At the Curie temperature, ferroelectric domains disappeared totally, as shown in Fig.7-11d. When the same sample was cooled down gradually from Curie temperature to room temperature, ferroelectric domains appeared gradually, as shown in Fig.7-11e and Fig.7-11f. It must be noted that there is a contrast difference between the Fig.7-11a and Fig.7-11f at the same room temperature. The ferroelectric domains changed their polarization distribution if the temperature of the sample is changed. The same phenomenon is also shown in Fig.7-9b and Fig.7-10.

By the use of a bias voltage between the tip and the backside of the sample, the electric dynamic property of ferroelectric domains of the same structures are imaged by SNAM developed. The results are shown in Fig.7-12. The studied area is the same as that studied above. All the images in Fig.7-12 have the same dimension of 20 µm and the grain boundary was imaged clearly in all the images. Therefore, the µ-bar to show the dimension of the images and the arrow to show the grain boundary are only noted in Fig.7-12a as well. In Fig.7-12a, domain structures were imaged under 0V bias voltage by SNAM developed. Under 40V bias voltage, the same area was imaged by the same set-up and the acoustic image is shown in Fig.7-12b. Then the bias voltage was switched off and the same area was imaged immediately once more, as shown in Fig.7-12c.

It is clear that most of structures disappeared when the area was scanned by a dc bias voltage of 40V between the tip and the backside of the sample. After the dc bias voltage was removed, some ferroelectric structures appeared once more but with changed structures.

Because the ferroelectric structures at the top surface of ferroelectric $BaTiO_3$ materials, which are believed to be different from the bulk structures [1~4], are little documented in literatures, the phenomena could only be explained by the use of the theoretical model developed.

At first, it is necessary to note that a ceramics does not change its polarization totally in one direction even when the ceramics is under an electric field which is much greater than its coerce field. Some domains will change their polarization under the coerce field and some remain always in the same direction, as the polarization direction is decided from the minimum of the internal energy under the clamped conditions among different grains (see Chapter 2).

When the 40 V dc bias between the tip and the backside of the sample was applied, according to the calculation of the field intensity in Chapter 5, the field intensity has a value varied from 2000 kV/m at the surface to 50 kV/m at a depth of 6h=60 nm. Because the field intensity within this depth is greater than the ferroelectric coerce field intensity of the $BaTiO_3$ materials [from 50 kV/m to 200 kV/m], if the clamped conditions allowed, some domains would change polarization to the direction of the electric field within this depth. As a result, the periodical array of a- and c-domains in this area would be changed. The contrast, which comes from the integration between the polarization and the concentrated field, would be changed.

If the clamped condition of one area was so strong that the polarization of the domains at that area could not be changed even under the same coerce field, the contrast of the SNAM at that area would not change, so that the integration was the same as the integration without the dc bias field. The contrast in this area would not be changed.

Naturally, this electric field intensity changed the internal energy of the area, where the domains were changed. When the tip moved away from the area, the ferroelectric domain structures at the recent scanned area would change in such a way that the internal energy at the area would have a minimum under the new boundary conditions. These new boundary conditions, such as the elastic and electric fields from the neighboring area which was just being scanned, were naturally not the same as the boundary conditions when the domain structures in Fig.7-12a had been established. Therefore, the change of polarization of the ceramics would take place as soon as the tip moved away from the area studied. Finally, this change of ferroelectric domain structures was imaged clearly in Fig.7-12c when the dc bias voltage was switched off.

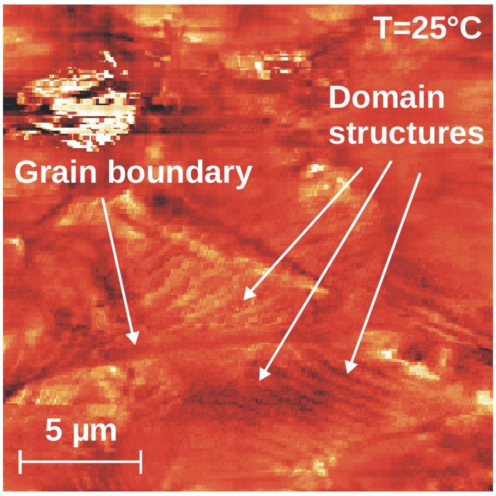

Fig.7-11a: Acoustic image of SNAM at room temperature (25°C)

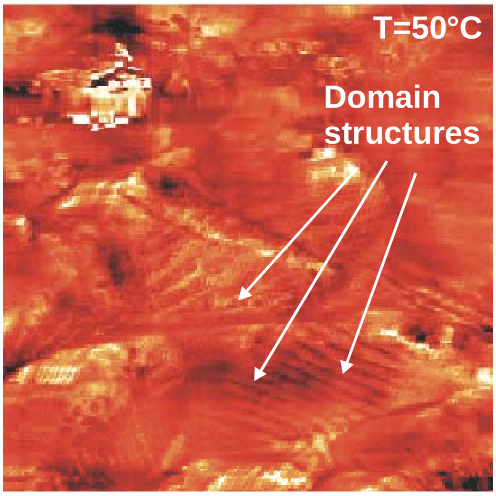

Fig.7-11b: Acoustic image of SNAM when temperature went up to 50°C

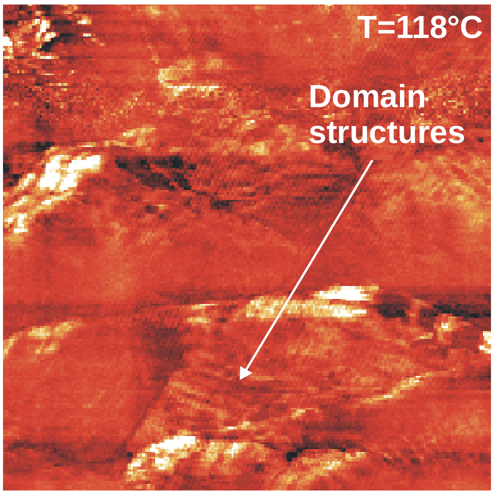

Fig.7-11c: Acoustic image of SNAM when temperature went up to 118°C

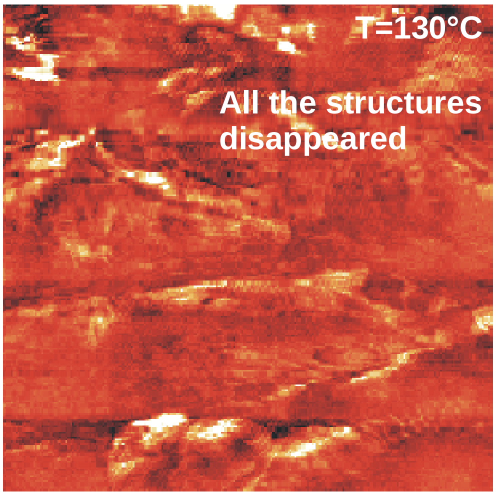

Fig.7-11d: Acoustic image of SNAM at temperature over Curie point

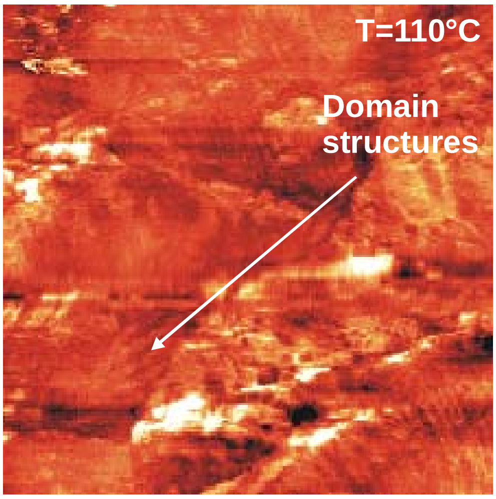

Fig.7-11e: Acoustic image of SNAM when temperature went down to 110°C

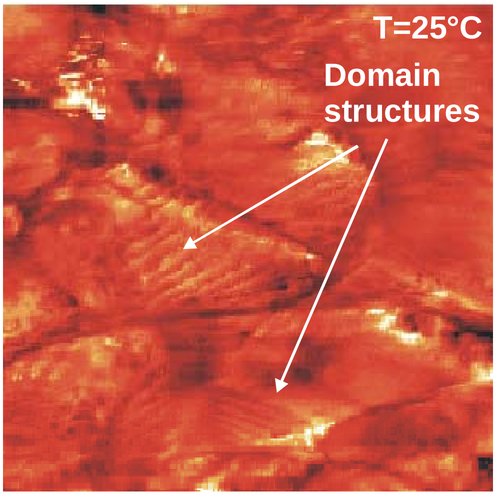

Fig.7-11f: Acoustic image of SNAM when temperature went back to 25°C

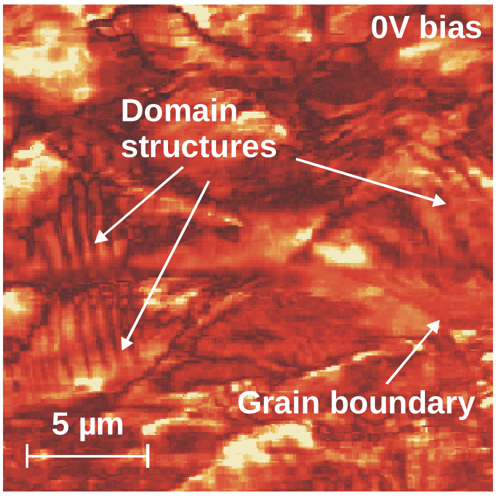

Fig.7-12a: The acoustic image of one structure imaged under 0 V bias voltage

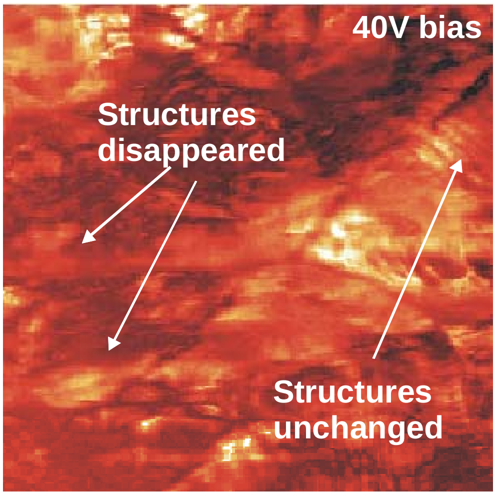

Fig.7-12b: The acoustic image of the same area imaged under 40 V bias

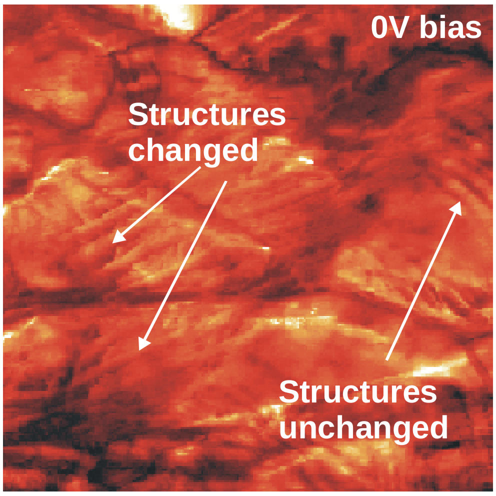

Fig.7-12: The acoustic image after the bias voltage was switched off

8 Discussion of both near-field acoustic techniques

8.1 Quality of imaging compared to other techniques

The SNAM and SEAM imaging techniques have many advantages over other techniques to image ferroelectric domains. The most exciting characteristics of both techniques are the nondestructive imaging of ferroelectric domains with no sample preparation. The easy development from commercial SPM or SEM systems is another advantage. SNAM has further advantages over SEAM in these respects, such as no vacuum system, better resolution down to nanometer, and flexibility of dynamic imaging of ferroelectric domains of materials. On the other hand, SEAM has such peculiarities as large imaging depth and broad imaging area which are also not so easy to obtain only by the use of SNAM. Therefore, both techniques will be applied complementarily to study ferroelectric materials in the future.

8.1.1 Speed of experiment

The imaging speed of SEAM is limited by the near-field establishing time in ferroelectric materials. As it is discussed in Chapter 4, the time required to established the electric field in near-field in SEAM depends on the charge accumulation in near-field and the properties of materials. typical values for semiconductor and ceramics are in the range of 10^{-4} second. To ensure good acoustic image of SEAM, the time at every pixel is usually chosen as 1 ms. For one typical image with 400X400 pixels, it would take about 1~2 minutes to take one image.

SNAM technique has to scan the tip (or sample) by a piezoelectric scanning unit. Unlike SEAM, it needs almost no delay time to establish the electric field in near-field. The imaging time of the system is mainly dependent on the scanning speed of SPM. In order to ensure a good topography, the scanning speed is usually slow, smaller than 1200 pixel/second. For an image of 400X400 pixels, it takes about 1~2 minutes to take a picture. It is clear that both techniques have almost the same image speed.

8.1.2 How quantitative

Generally speaking, the SEAM and SNAM are both scanning imaging techniques which record the relative variation among scanning pixels in a given scanned area. If physical properties of one scan pixel or one area can be determined quantitatively, the rest of scan pixels can hereafter be imaged quantitatively.

SEAM technique has a very complicated interaction on the surface of ferroelectric materials, when the primary electrons bombard the surface. Although much effort has been paid to analyze interactions of primary electrons bombarding on metal materials, semiconductors, and some dielectric materials, both experimental and theoretical work on ferroelectric materials are little documented in present literatures. A quantitative analysis requires the estimation of parameters of experimental environments and their errors. If some basic parameters of SEAM on ferroelectric materials, such as the accurate electric field intensity in near-field, the accurate penetration depth of PE, the calculable relationship of different imaging mechanisms and so on, are not quantitatively determined, the quantitative analysis of ferroelectric polarization by SEAM would be impossible. Unfortunately, these important factors have been sparsely documented in the present literatures. Therefore, the SEAM technique remains in principle a qualitative imaging technique up till today.

Whether the SNAM or the related techniques are quantitative tools, is still a recent study which is heavily debated today [31~33, 85]. To analyze the problem, it would be better to review some basic approximations which are often used in the present literatures to characterize ferroelectric materials by SNAM systems. Firstly, as discussed in Chapter 2, the piezoelectric constant of ferroelectric ceramics depends on spontaneous polarization only under the condition that external piezoelectric effect is neglected and polarization will not be affected during the imaging; Secondly, to determine the electric field in the sample, all the literatures assume that the sample is isotropic; Thirdly, only the main mode of the vibrations in near-field is calculated and the acoustic mode conversions and nonlinear effects in near-field are neglected; Finally, by detecting the near-field vibration through laser beam and photodiodes in piezoelectric response mode, there exists a very complicated vibration transmission function of the cantilever [84, 85] from which an accurate estimation of errors would be difficult. On the other hand, by detecting the near-field vibrations through a transducer, as it is done in this work, all the theoretical calculation must be under the approximation of acoustic plane wave. Possible errors incurred under so many approximations by the modeling of SNAM would be difficult to estimate at present as well. It would be necessary to say that under all the approximations above, the theoretical model developed for both SEAM and SNAM in this work can be used to calibrate the acoustic contrast or domain structures quantitatively.

8.2 Comparison of SEAM and developed SNAM system

8.2.1 Image comparison and analyses

To compare the image of two kinds of microscopy techniques, it is necessary to compare the properties at identical areas. As it is concerned with the nondestructive study of the ferroelectric domains, the domain structures should not be damaged during the change of

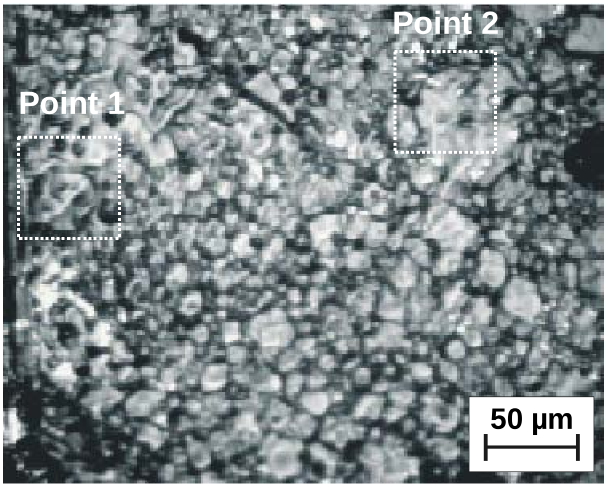

Fig.8-1: Optical image of one area of sample AC0

microscopes. The method is already described in Chapter 6. By the use of optical microscopy, one area of sample AC0, from the University of Halle, Germany, is imaged as a standard to compare topography, as shown in Fig.8-1.

The same area is imaged by SEAM, as shown in Fig.8-2.

From SEAM images of Fig.8-2, the contrast of domain structures are imaged only in acoustic images. The contrast in acoustic images has typical 90° striped structures with the width from 5 to 10 µm. By the comparison to the optical image Fig.8-1 in which the grain size are usually from 10 µm to 50 µm, the contrast from ferroelectric domains in acoustic images of SEAM has naturally no relationship with grain sizes.

After the ceramics was studied by SEAM, two typical coarse grains were chosen to be studied complementarily by SNAM. One grain, which has a diameter of 30 µm, is marked as point 1 in optical image Fig.8-1 and in SE images of Fig.8-2c and Fig.8-2e. The acoustic contrast of the grains by SEAM are marked as a white insert with dashed line in SEAM acoustic images Fig.8-2d and Fig.8-2f. The other grain, which has a diameter 60 µm, is marked as point 2 in optical image Fig.8-1 and in SE images of Fig.8-2c. The acoustic contrast of the grain by SEAM is marked as a white insert with dashed line in SEAM acoustic image Fig.8-2d.

Domain structures are shown clearly by the acoustic images of Fig.8-3 and Fig.8-4. The contrast from domain structures have widths from one hundred to several hundred nanometer. It has the same order of domain size which is calculated theoretically by other works [6~10].

Furthermore, it is shown in Fig.8-3f that some domains have correspondence of contrast, as shown at the lower part in Fig.8-3f. This can be explained as that the sample in this area has the α structure of domain structures of coarse grains in $BaTiO_3$ [6]. The same structures can also be seen clearly at the upper side in Fig.8-4f. Some domain structures such as those imaged in the upper part of Fig.8-3f, have no correspondence of contrast. This can be explained as the γ domain structures of ferroelectric domains discussed in Chapter 2.

It must be noted, If the acoustic images by SEAM in Fig.8-2 and the acoustic images by SNAM in Fig.8-3 and Fig.8-4 on the both grains are compared, it can be seen clearly that the acoustic contrasts on the same grains by both techniques are totally different.

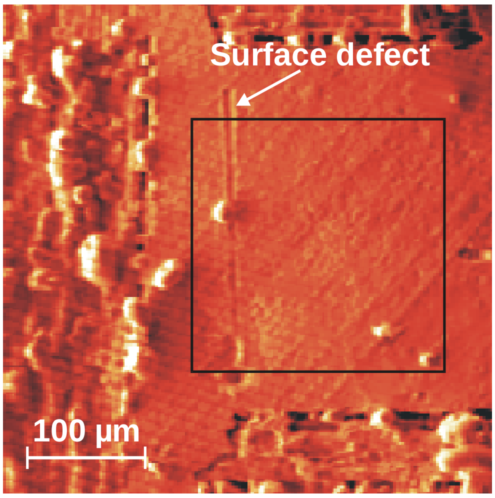

Fig.8-2a: SE image of the same sample as Fig.8-1

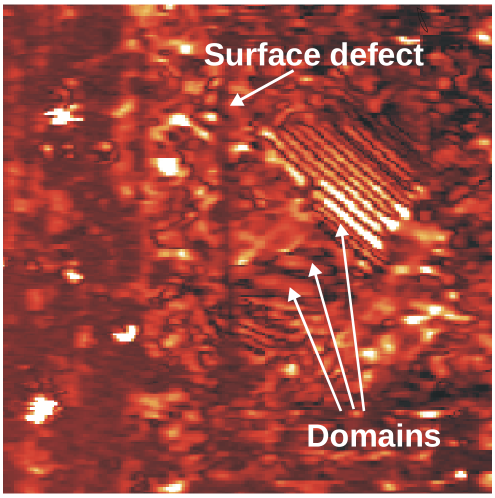

Fig.8-2b: SEAM *in situ* acoustic image of Fig.8-2a

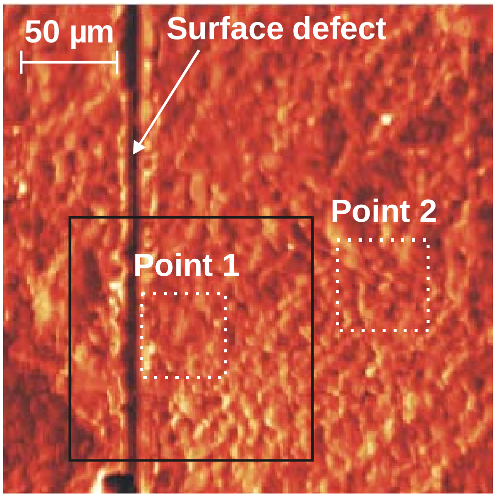

Fig.8-2c: SE image of the insert with black line in Fig.8-2a

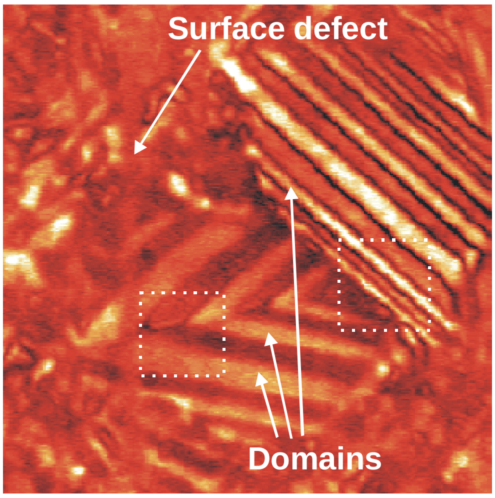

Fig.8-2d: SEAM *in situ* acoustic image of Fig.8-2c

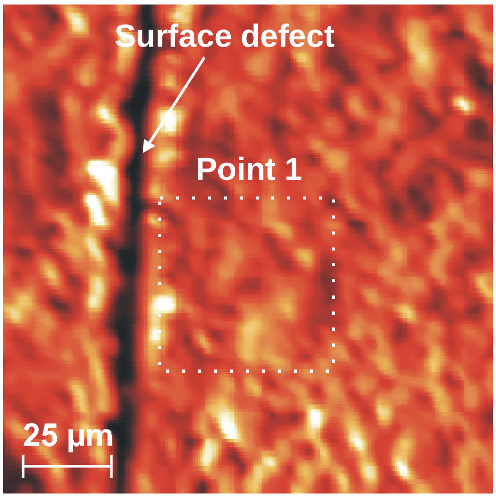

Fig.8-2e: SE image of the insert with black line in Fig.8-2c

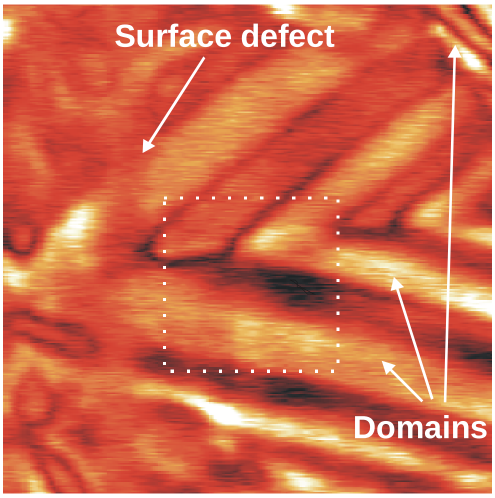

Fig.8-2f: SEAM *in situ* acoustic image of Fig.8-2e

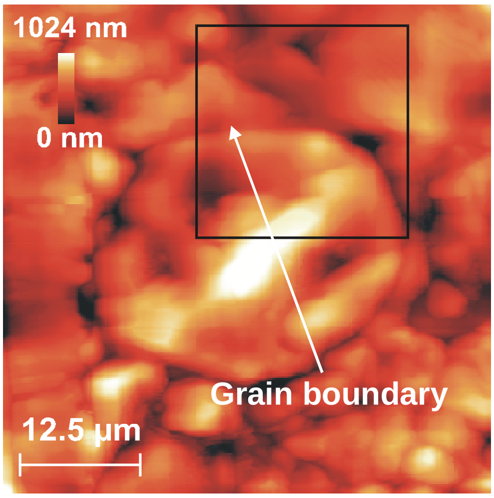

Fig.8-3a: Topography of point1 in Fig.8-1 by SPM

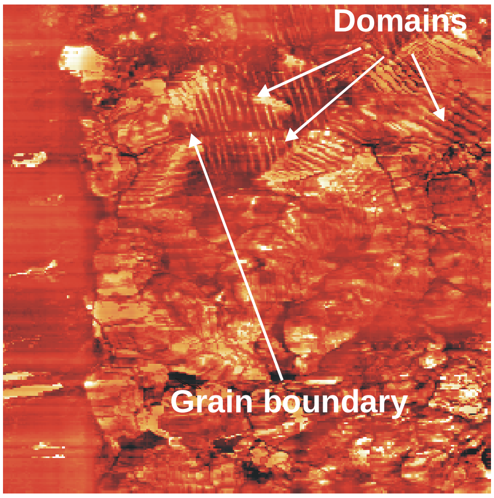

Fig.8-3b: SNAM *in situ* acoustic image of Fig.8-3a

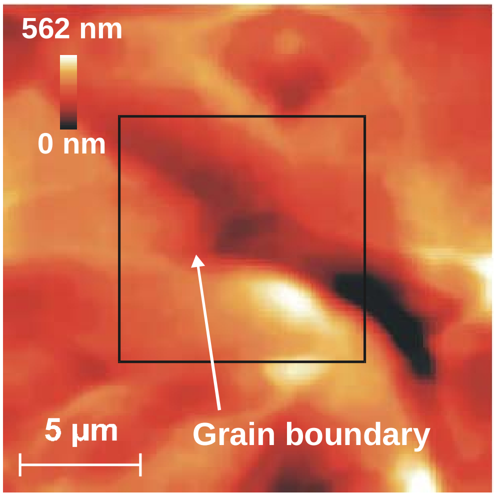

Fig.8-3c: Topography of the insert in Fig.8-3a by SPM

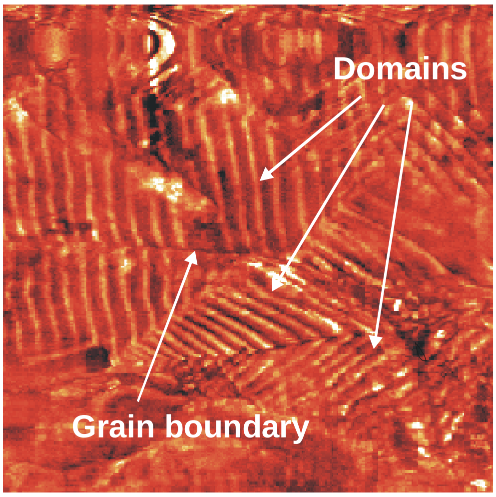

Fig.8-3d: SNAM *in situ* acoustic image of Fig.8-3c

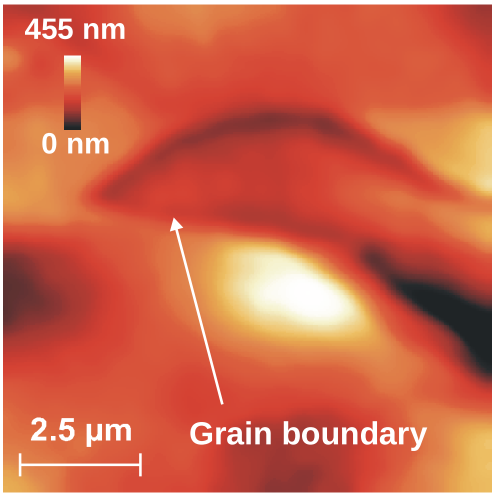

Fig.8-3e: Topography of the insert in Fig.8-3c by SPM

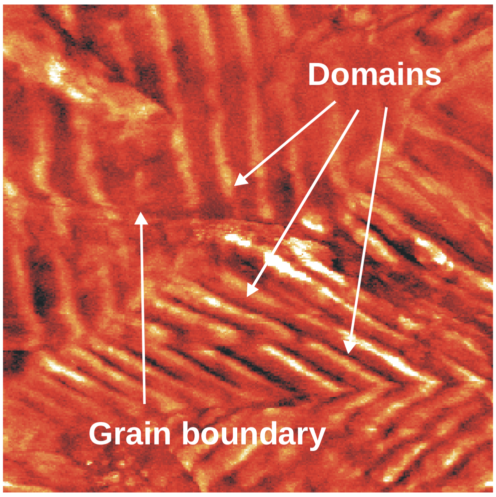

Fig.8-3f: SNAM *in situ* acoustic image of Fig.8-3e

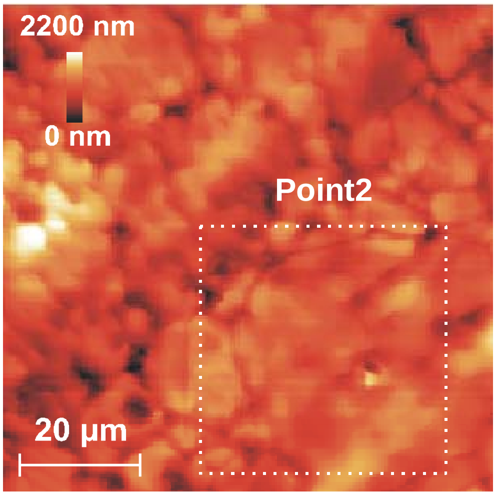

Fig.8-4a: Topography of the area near the point 2 in Fig.8-1 by SPM

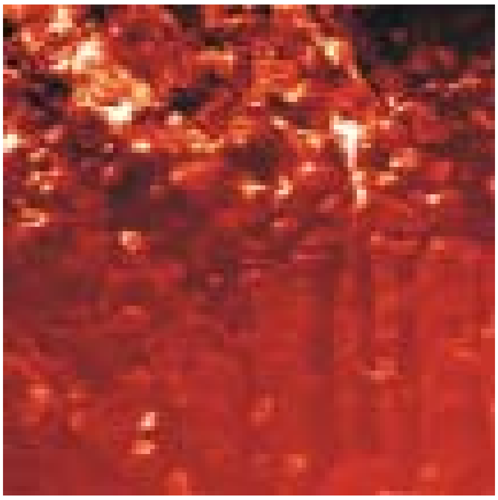

Fig.8-4b: SNAM *in situ* acoustic image of Fig.8-4a

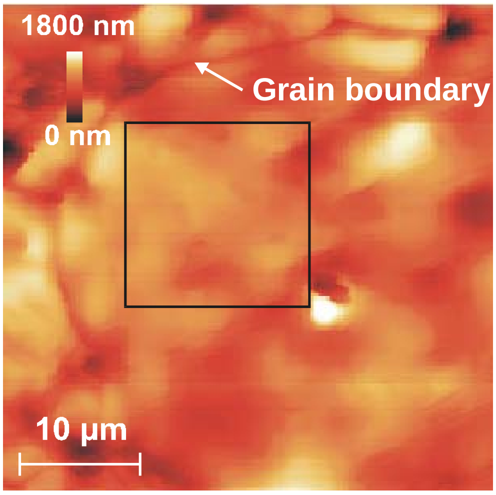

Fig.8-4c: Topography of the point 2 in Fig.8-4a by SPM

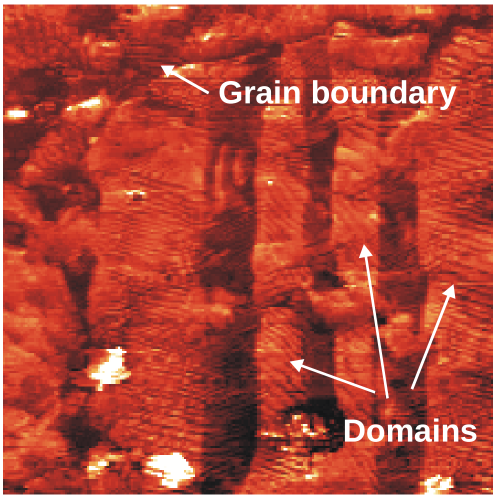

Fig.8-4d: SNAM *in situ* acoustic image of Fig.8-4c

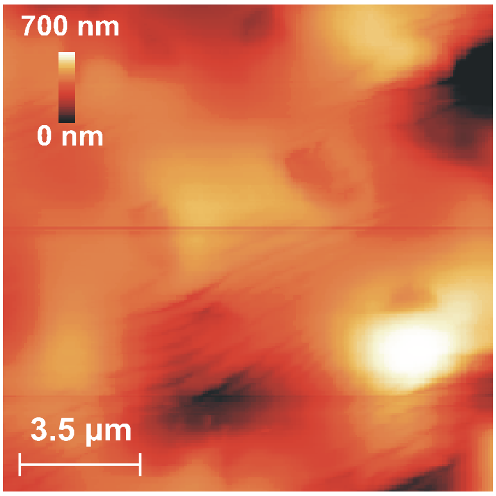

Fig.8-4e: Topography of the insert in Fig.8-4c by SPM

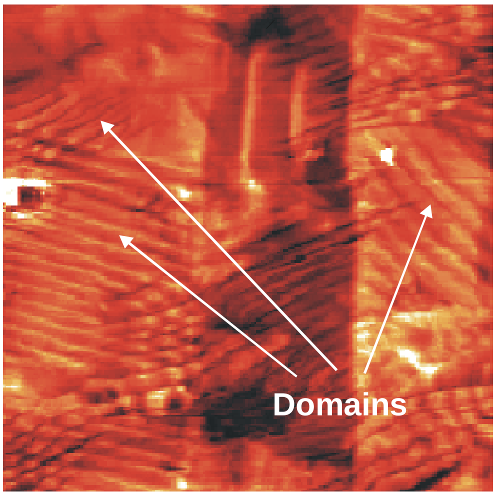

Fig.8-4f: SNAM *in situ* acoustic image of Fig.8-4e

8.2.2 Explanation of the results

The contrast difference of acoustic images by SEAM and SNAM at the identical areas (point 1 and point 2) can be explained as the depth difference of near-fields of both techniques. As it is explained in Chapter 4 and Chapter 5 theoretically, the contrast of both near-field acoustic imaging techniques (SEAM or SNAM) comes from interaction between the average piezoelectric effect in near-field and the electric field formed by injecting electrons (SEAM) or the concentrated field of the scanning tip (SNAM). As it is not well understood up to now how the domain wall movements contribute to the piezoelectric, elastic and dielectric properties of ferroelectric ceramics extrinsically [8, 11~13] and how many kinds of domain structures of $BaTiO_3$ ceramics exist totally [9, 10], an accurate theory of average piezoelectric effects in near-field area for both techniques on $BaTiO_3$ materials would be impossible. As a result, a clear explanation of contrast of both near-field acoustic methods seems also difficult at present. The following would be an explanation which bases solely on the present theory and experimental facts:

- The typical domain structures in ceramics have the typical width of several hundred nanometers for coarse grains, as predicated by present theories and experimental methods [9, 10];
- The electric field in the near-field is so weak that it produces only vibration through intrinsic converse piezoelectric effect and small movements of domain walls but no change of the whole domain structures [13];

By SEAM, the near-field dimension is almost 1-2 µm wide and 2-3 µm deep at 20 keV accelerating voltage for PE, and the interaction area is not homogeneous [57]. For the typical domain structures which are clear to us [9], such as shown in Chapter 2, the domain width is usually several hundred nanometer. Here, we would take a coarse grains of $BaTiO_3$ ceramics as an example. The typical domain structures have been studied [9, 10]. The domains have typically four structures, shown as structure 1-4 in Fig.8-5.

As shown in Chapter 4, the acoustic amplitude contrast of SEAM of every scan point comes from the average interaction between the electric field formed by injecting electrons and the average piezoelectric effect in the whole interaction area. For scan point N and any other scan points in area of structure 1, there is no difference of the average integration in near-field. That means that there is no contrast difference by SEAM in the area of structure 1. With the same argument, there is no contrast difference for any scan point M in the area of structure 2. Similarly, any scan point in the areas of structure 3 or 4 has no contrast difference with any other points in the same structure respectively.

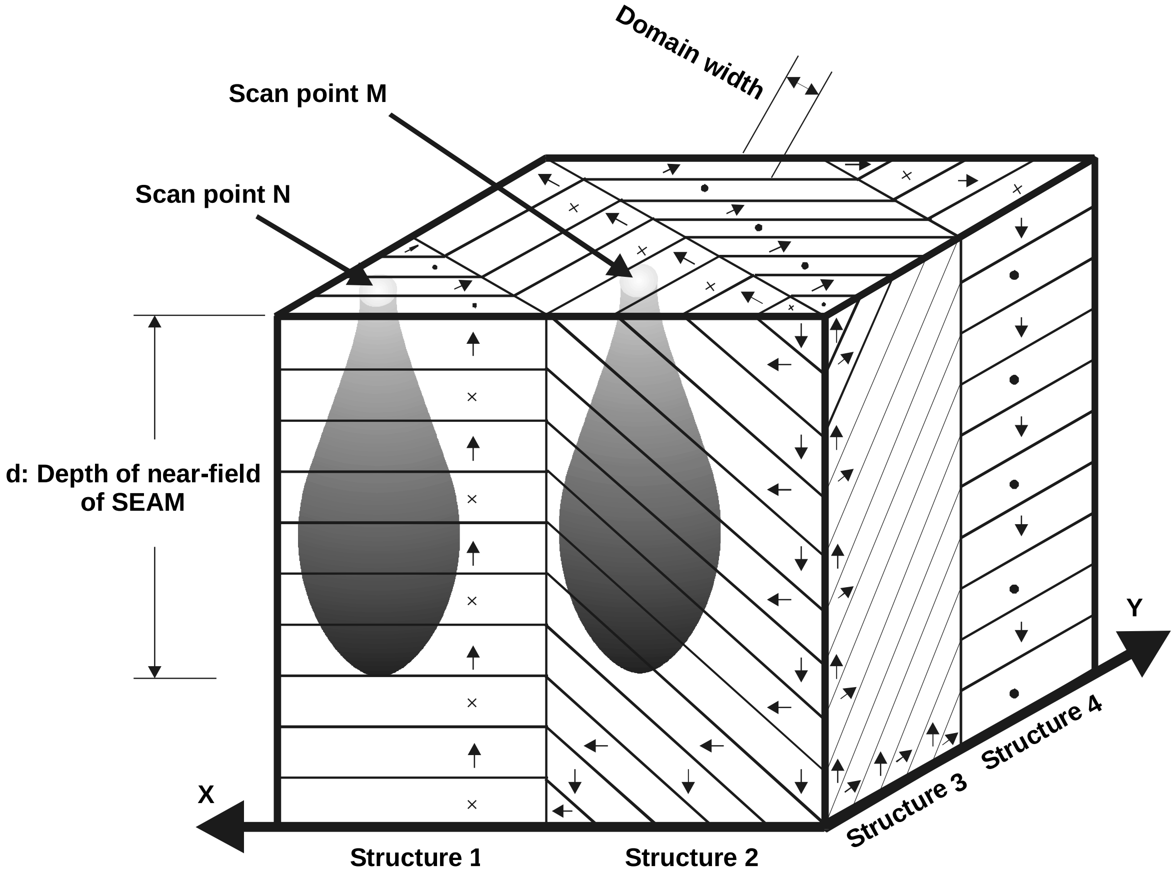

Fig:8-5: The contrast mechanism of SEAM on the ceramic sample

Furthermore, according to Eq.2-24 in Chapter 2, the piezoelectric effect of ferroelectric ceramics is dependent on the polarization and extrinsic effect. If the electric field in near-field area in SEAM is small enough, the extrinsic effects (mainly of domain wall movements) can be neglected [13]. Thus the piezoelectric effect in near-field area of SEAM is solely dependent on the spontaneous polarization. We can draw qualitatively the spontaneous polarization for structure 1-4 which contribute to acoustic longitudinal waves in z direction in near-field of SEAM system as Fig.8-6.

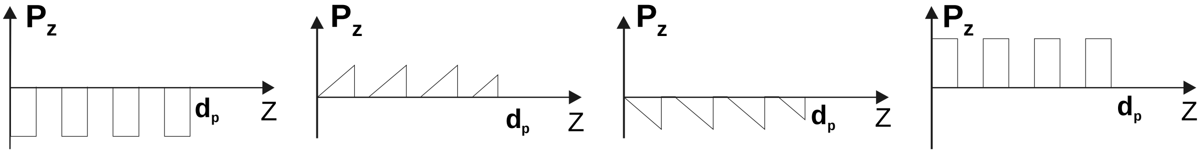

Fig.8-6a: Structure 1 Fig.8-6b: Structure 2 Fig.8-6c: Structure 3 Fig.8-6d: Structure 4

Because the output signal of transducer is the integration between the converse piezoelectric effect and the source electric field in near-field area according to Eq.3-38, after the linear amplification of the lock-in amplifier, the output signal of the lock-in amplifier is proportional to this integration. As only amplitude signal of the lock-in amplifier is used as the imaging signal of SEAM, the gray lever of the acoustic image of SEAM is naturally proportional to amplitude of this integration as well. As shown in Fig.8-6a and Fig.8-6d, the average polarization in structure 1 and structure 4 has the same value but only changes its sign. If the source electric field is kept the same during scanning, the amplitudes of the integration between the converse piezoelectric effect and the source electric field in these two areas have the same absolute value but only different signs. That means these two areas have the same gray lever in acoustic image of SEAM.

According to the same reasoning, there would be no contrast difference between structure 2 and structure 3 either.

At the base of reasoning above, there are only two structures, structure 1 and structure 2 shown in Fig.8-6a and Fig.8-6b above, in which the scanning pixels, such as the pixel M in structure 2 and pixel N in structure 1 shown in Fig.8-5, have possibly different contrast in acoustic image of SEAM. In other words, under the present knowledge of domain structures in ferroelectric $BaTiO_3$ ceramics, the acoustic image of SEAM would image only the difference between different laminated areas. The imaged ‘domain wall’ could be the wall between different 90° domain laminated structures of $BaTiO_3$ ceramics.

If the same structures are studied by SNAM technique, the contrast can be analyzed in the same way. Because of the form of the tip, most of the source electric field is concentrated just beneath the contact point under the tip, as it is discussed and calculated in Chapter 5 in this work, so that the near-field area of SNAM is as small as several hundred nanometer (see Eq.5-18 and Fig.5-5). Under the same week field approximations discussed above and according to Eq.5-20, the output signal of the transducer in SNAM is proportional to the integration between the converse piezoelectric effect and the source electric field in near-field area of every scan points of SNAM. After the linear amplification of the lock-in amplifier, the output signal of the lock-in amplifier is proportional to this integration as well. As only the amplitude signal of the lock-in amplifier is used as the imaging signal of SNAM, the gray lever of the acoustic image of SNAM is naturally proportional to the amplitude of this integration. Two scan points in area of structure 1 shown in Fig.8-7 are taken as an example. The scan point N has a polarization parallel to the source electric field. The converse piezoelectric effect in near-field in the direction of the field is non-zero. The integration between the converse piezoelectric effect and the field is non-zero too. The contrast in acoustic image of SNAM at this point has a non-zero gray lever.

On the other hand, the scan point M has the polarization perpendicular to the source electric field in near-field and the converse piezoelectric effect in near-field in the direction of the field would be zero. The integration between the converse piezoelectric effect and the field would be zero as well. This means that the contrast at this point in acoustic image of SNAM has a zero gray lever. As the point N and M are arbitrarily chosen in the area of structure 1, if the source electric field is kept the same during scanning, any scan point which has a polarization in the direction of the source electric field in structure 1 has the same non-zero gray lever in acoustic images of SNAM; Whereas any point which has a polarization perpendicular to the direction of the source electric field has the zero gray lever.

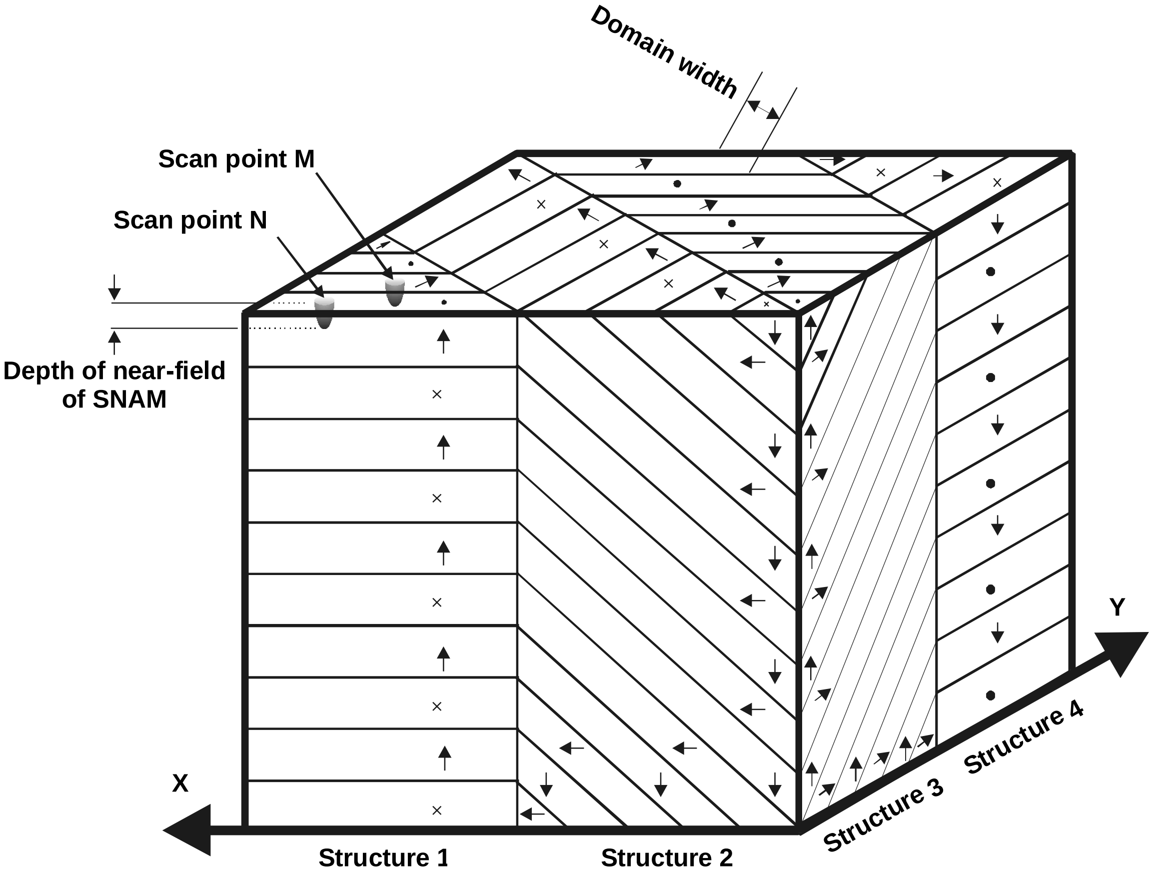

Fig.8-7: The contrast mechanism of SNAM system developed

In other words, the contrast of acoustic image of SNAM comes from difference of ferroelectric polarization directions of 90° domain structures. It can be seen easily that the reasoning is also valid in area of structure 2, 3, or 4. By comparison of Fig.8-5 and Fig.8-7, it is clear that the 90° degree domains will show different width and totally different contrast by SEAM and SNAM techniques.

9 Conclusions

Investigations of ferroelectric domain structures are essential for both fundamental and applied perspectives since they determine, to a large extend, the macroscopic response of ferroelectric materials. In microscopic range, they dominate the behavior of almost all ferroelectric devices in the microelectronic industry. The results presented in this work on ferroelectric $BaTiO_3$ materials show the fascinating world of this kind of materials. The dimension of the imaged ferroelectric domain structures by SNAM provides experimental evidence for the theory of these structures in coarse grained $BaTiO_3$ ceramics, which are only proved by destructive methods such as the chemical etching techniques before now.

Temporal behavior of ferroelectric domain structures at an identical area of $BaTiO_3$ ceramics has been imaged at submicrometer range for the first time. The domain structures of the ceramics remain unchanged for two years. It implies that ferroelectric polarization of this kind of ceramics is very stable and it would be an ideal medium for applications such as memory devices.

Thermal dynamical properties of ferroelectric domain structures at an identical area of $BaTiO_3$ ceramics are imaged by SNAM at submicrometer range. When the temperature of the ceramics is over Curie temperature, the domain structures disappear totally. The ferroelectric domains change their polarization distribution if the temperature of the sample changes. Electrical dynamical study of ferroelectric domains at an identical area of $BaTiO_3$ ceramics has also been studied. With a bias voltage, the change of the same structures are imaged clearly. Based on the developed theoretical model, the field intensity under the tip and the physical process of polarization change on the sample surface are analyzed. These dynamic investigations lays the foundations for future dynamic analysis of ferroelectric domains of other materials by SNAM.

The system developed for dynamic research of ferroelectric domain structures in this work can be easily modified from a commercial SPM system. For the further study of other ferroelectric materials and devices, this system is easy to use, with submicrometer or nanometer resolution, and high thermal and electric stability if simple control units are used. It presents an ideal tool for the non-destructive dynamic testing and modeling of both ferroelectric materials in material engineering and ferroelectric devices in microelectronic industry.

The explanation of the contrast from acoustic non-destructive imaging systems remains always a challenge for researchers in this area. The SNAM system developed by the use of an acoustic transducer provides a base for both theoretical and experimental complementary analyses of the acoustic contrast among different kinds of acoustic near-field systems. As an example, the complementary analysis of SEAM and SNAM reveals the acoustic contrast mechanisms of both near-field techniques. The different contrast which are revealed by complementary analysis at identical areas can be well-explained using the current theory for $BaTiO_3$ ceramics. The experimental methods developed for the complementary analysis can be further applied to analyze other properties of materials and devices among different microscopy systems.

The theoretical modeling of SNAM analysis, i.e. the Green´s function to determine the quasi-stationary fields in the system and the transmission line mode of acoustic longitudinal waves within the sample, is applied successfully for the first time to characterize electrical and mechanical field distributions of $BaTiO_3$ materials studied by SNAM. Based on the theoretical solutions presented in this work, other ferroelectric materials can be analyzed similarly.

Under the same theoretical approximations as those of SNAM system, the contrast of SEAM system on ferroelectric materials has been characterized by these theoretical techniques as well. Although only acoustic plane wave modes are analyzed, the simple solution reveals some basic behavior of SEAM system on ferroelectric materials. The modelling technique would be also applicable to other beam injecting acoustic imaging systems.

10 Future aspect

The characterization of ferroelectric materials at submicrometer or even in nanometer range, both in lateral direction and in depth profiling, is of vital importance for the development of future ferroelectric materials and integrated devices. Unfortunately, the present knowledge of ferroelectric domains at this resolution range is not enough to predict the so-called 'domain' influence on the materials. Whereas common methods have different limitations for this purpose, the non-destructive methods based on SPM provide a new breakthrough for this goal. Although much effort on this technique has been given and many results are presented for different ferroelectric materials by different techniques based on SPM, from our point of view, a clear relationship between these domain effects and properties of ferroelectric materials require further investigations.

The quantitative description of energy change of ferroelectric domains during switching processes is not well understood. As discussed in many literatures [1~13], this energy change is a process including thermal, electrical, and elastic energy. Although this work has shown some changes of domain structures by external thermal and electrical influences, the accurate relationship among the thermal, elastic, and electrical energy changes should be further investigated. To understand this process as accurately as possible, different non-destructive methods at this resolution range, such as thermal and acoustic near-field techniques, should be used complementarily.

The thermal behavior of ferroelectric domains of $BaTiO_3$ is another problem which needs further study as well. Although current literatures present many theoretical and experimental results on this effect [1~5], a quantitative study of thermal behavior of domain structures of $BaTiO_3$ at submicrometer or nanometer resolution is still not reached. Even though some thermal dynamic investigation has been presented in this work, a quantitative relationship between ferroelectric domain structures and the external thermal energy change has not been obtained yet. To achieve this goal, a complementary analysis on ferroelectric $BaTiO_3$ by thermal and acoustic near-field techniques would be ideal.

The metal-doped $BaTiO_3$ is widely used in industry for different purposes [86]. Although some work has been done to reveal the relationship among grain sizes, electrical, elastic, and piezoelectric properties, ferroelectric domain structures from doped $BaTiO_3$ materials are little studied. The theoretical relationship between grain sizes and ferroelectric domain structures for doped $BaTiO_3$ is not achieved either. The presented SEAM and SNAM techniques are the best non-destructive tools for experimental investigations and basis for the modeling and manufacturing of this kind of materials.

Ferroelectric thin films are used intensively in the micro-electronic industry and some properties of thin films are also intensively studied [4, 22, 31~35]. But, from our point of view, ferroelectric domain structures and their formation process under external influences needs to be studied further. Problems such as how the domains change their structures during switching processes, how much is the switching time of different structures, what are the main sources of the fatigue of the ferroelectric polarization and so on require further study. To answer all the questions, a thorough understanding and modeling of ferroelectric thin films, both experimentally and theoretically, would be necessary.

Although this work has presented a systematic theoretical method to study the electrical and acoustical field distributions from different sample structures in SNAM system, there is still a lot of work to do to characterize all the field components quantitatively. Whereas the electric field distributions in the system can be determined by the Green´s functions, the acoustic field solutions are only based on plane wave modes. For quantitative characterization of ferroelectric materials by SNAM, it is necessary to analyze the acoustic fields more accurately. The acoustic field mode conversion in near-field and the non-linear effects of ferroelectric materials should be further studied.

Recent literature [87] points out that modern chip industries face severe problems for modeling of devices and failure analysis as multilayered systems are used intensively in the nanometer regime. The characterization of electrical, thermal, and acoustical field distributions in these systems is of vital importance to develop new devices. As the structures of these devices have nanometer dimensions, some basic conditions for present phenomenological theories cannot be fulfilled any more. New basic theoretical backgrounds including a combination of quantum-mechanics and quantum-electronics for the characterization of these devices must be thoroughly developed. However, the systematic phenomenological methods are foundations for this future advancement.

11 Appendix

A1: Solution of one-dimensional piezoelectric stiffened plan wave in $BaTiO_3$ and PZT

The piezoelectric strain and stress relationships are:

$$x_I = s_{I,J}^{\vec{E}}\ X_J + \tilde{d}_{I,j}\ E_j \qquad \text{Eq.A-1}$$

$$D_i = d_{i,J}\ X_J + \varepsilon_{i,j}^{\overleftrightarrow{X}}\ E_j \qquad \text{Eq.A-2}$$

$$X_I = c_{I,J}^{\vec{E}}\ x_J - \tilde{e}_{I,j}\ E_j \qquad \text{Eq.A-3}$$

$$D_i = e_{i,J}\ x_J + \varepsilon_{i,j}^{\overleftrightarrow{x}}\ E_j \qquad \text{Eq.A-4}$$

To characterize the typical near-field acoustic system of present work on $BaTiO_{3,}$ it is necessary to discuss at first the coupling between electric and acoustic fields generally in both PZT transducer and $BaTiO_3$ sample in one dimension. The polarized PZT ceramics can be analyzed by a crystal lattice of 6mm and the crystal lattice of single $BaTiO_3$ with only c-monodomain is 4mm [53]. The piezoelectric tensor and dielectric tensor for both material systems have the same form but different values of components. This allows us to treat the coupling in transducer as well as in near-field theoretically together. Only if quantitative values of each material are concerned, actual values of the tensor components will be used respectively.

If z direction is chosen as the transmission direction, the differential $\frac{\partial}{\partial x}$ and $\frac{\partial}{\partial y}$ are equal to zero if the lateral dimension is unlimited. Only $\frac{\partial}{\partial z}$ is non-zero for every electric and mechanic field components.

From Maxwell equation Eq.3-1, if there are no conducting and source currents ($\vec{J}_c$ and $\vec{J}_s$) in a given material, electromagnetic fields and waves which transmit only in z direction will be described as [53]:

$$\nabla \times \vec{E} = \begin{pmatrix} 0 & -\frac{\partial}{\partial z} & \frac{\partial}{\partial y} \\ \frac{\partial}{\partial z} & 0 & -\frac{\partial}{\partial x} \\ -\frac{\partial}{\partial y} & \frac{\partial}{\partial x} & 0 \end{pmatrix} \times \begin{pmatrix} E_x \\ E_y \\ E_z \end{pmatrix} = -\mu_0 \frac{\partial \vec{H}}{\partial t},$$

or $$\begin{pmatrix} -\frac{\partial E_y}{\partial z} \\ \frac{\partial E_x}{\partial z} \\ 0 \end{pmatrix} = -\mu_0 \begin{pmatrix} \frac{\partial H_x}{\partial t} \\ \frac{\partial H_y}{\partial t} \\ \frac{\partial H_z}{\partial t} \end{pmatrix}$$ Eq.A-5

$$\nabla \times \vec{H} = \begin{pmatrix} 0 & -\frac{\partial}{\partial z} & \frac{\partial}{\partial y} \\ \frac{\partial}{\partial z} & 0 & -\frac{\partial}{\partial x} \\ -\frac{\partial}{\partial y} & \frac{\partial}{\partial x} & 0 \end{pmatrix} \times \begin{pmatrix} H_x \\ H_y \\ H_z \end{pmatrix} = \frac{\partial \vec{D}}{\partial t},$$

or $$\begin{pmatrix} -\frac{\partial H_y}{\partial z} \\ \frac{\partial H_x}{\partial z} \\ 0 \end{pmatrix} = \begin{pmatrix} \frac{\partial D_x}{\partial t} \\ \frac{\partial D_y}{\partial t} \\ \frac{\partial D_z}{\partial t} \end{pmatrix}$$ Eq.A-6

The equations above can be written as:

$$\mu_0 \frac{\partial H_x}{\partial t} = \frac{\partial E_y}{\partial z}, \quad \frac{\partial D_y}{\partial t} = \frac{\partial H_x}{\partial z}$$ Eq.A-7

$$-\mu_0 \frac{\partial H_y}{\partial t} = \frac{\partial E_x}{\partial z}, \quad \frac{\partial D_x}{\partial t} = -\frac{\partial H_y}{\partial z}$$ Eq.A-8

$$\frac{\partial D_z}{\partial t} = \frac{\partial H_z}{\partial t} = 0$$ Eq.A-9

Eq.A-7 and Eq.A-8 describe two electric magnetic waves and Eq.A-9 two quasi-stationary fields.

If the body torque is neglected under the small signal approximation, the basic acoustic equations in materials are:

$$\nabla \cdot \overleftrightarrow{X} = \rho \frac{\partial^2 \vec{u}}{\partial t^2} - \vec{F}$$ Eq.A-10

$$\overleftrightarrow{x} = \nabla_s \vec{u}$$ Eq.A-11

in which $\vec{x}$ and $\vec{X}$ are strain and stress in the material respectively, and ρ, $\vec{u}$, and $\vec{F}$ are density of the material, displacement field, and body force respectively.

The signs of $\nabla\cdot$ and ∇_s mean the followings:

$$\nabla\cdot\overleftrightarrow{X}=\begin{pmatrix}\frac{\partial}{\partial x} & 0 & 0 & 0 & \frac{\partial}{\partial z} & \frac{\partial}{\partial y}\\ 0 & \frac{\partial}{\partial y} & 0 & \frac{\partial}{\partial z} & 0 & \frac{\partial}{\partial x}\\ 0 & 0 & \frac{\partial}{\partial z} & \frac{\partial}{\partial y} & \frac{\partial}{\partial x} & 0\end{pmatrix}\overleftrightarrow{X} \qquad \text{Eq.A-12}$$

$$\overleftrightarrow{x}=\nabla_s\vec{u}=\begin{pmatrix}\frac{\partial}{\partial x} & 0 & 0\\ 0 & \frac{\partial}{\partial y} & 0\\ 0 & 0 & \frac{\partial}{\partial z}\\ 0 & \frac{\partial}{\partial z} & \frac{\partial}{\partial y}\\ \frac{\partial}{\partial z} & 0 & \frac{\partial}{\partial x}\\ \frac{\partial}{\partial y} & \frac{\partial}{\partial x} & 0\end{pmatrix}\begin{pmatrix}u_x\\ u_y\\ u_z\end{pmatrix} \qquad \text{Eq.A-13}$$

Here the Voigt´s notation for stress and strain tensors is used and the stress and strain tensors are written as:

$$\overleftrightarrow{X}=(X_1,X_2,X_3,X_4,X_5,X_6)$$

$$\overleftrightarrow{x}=(x_1,x_2,x_3,x_4,x_5,x_6)$$

If the velocity of a particle in solids is $\vec{v}=\vec{a}_x v_x+\vec{a}_y v_y+\vec{a}_z v_z$, it can be written as:

$$\vec{v}=\frac{\partial}{\partial t}\vec{u} \qquad \text{Eq.A-14}$$

If there is no body force, the acoustic equations Eq.A-10 and Eq.A-11 can be written by the use of particle velocity as:

$$\frac{\partial X_3}{\partial z}=\rho\frac{\partial v_z}{\partial t} \quad \text{and} \quad \frac{\partial v_z}{\partial z}=\frac{\partial x_3}{\partial t} \qquad \text{Eq.A-15}$$

$$\frac{\partial X_4}{\partial z}=\rho\frac{\partial v_y}{\partial t} \text{ and } \frac{\partial v_y}{\partial z}=\frac{\partial x_4}{\partial t} \qquad \text{Eq.A-16}$$

$$\frac{\partial X_5}{\partial z}=\rho\frac{\partial v_x}{\partial t} \text{ and } \frac{\partial v_x}{\partial z}=\frac{\partial x_5}{\partial t} \qquad \text{Eq.A-17}$$

Eq.A-15 describes one longitudinal acoustic plan wave; Eq.A-16 and Eq.A-17 describe two shear acoustic waves.

According to piezoelectric coupling equations Eq.A-1 to Eq.A-4 and piezoelectric tensor of $BaTiO_3$, the electric and acoustic coupling can be written as:

$$D_z=\varepsilon_{zz}^s E_z+e_{z3}x_3 \qquad \text{Eq.A-18}$$

$$D_y=\varepsilon_{yy}^s E_y+e_{x5}x_4 \qquad \text{Eq.A-19}$$

$$D_x=\varepsilon_{xx}^s E_x+e_{x5}x_5 \qquad \text{Eq.A-20}$$

$$X_3=c_{33}x_3-e_{z3}E_z \qquad \text{Eq.A-21}$$

$$X_4=c_{44}x_4-e_{x5}E_y \qquad \text{Eq.A-22}$$

$$X_5=c_{44}x_5-e_{x5}E_x \qquad \text{Eq.A-23}$$

From electromagnetic wave equations Eq.A-7 to Eq.A-9, acoustic equations Eq.A-15 to Eq.A-17, and electric and acoustic coupling Eq.A-18 to Eq.A-23, the general coupling of electric and mechanic field components in $BaTiO_3$ can be analyzed. The acoustic longitudinal wave described by Eq.A-15 will be studied with detail in the following.

According to Eq.A-9, the electric displacement D_z is a constant. For a harmonic study of fields, D_z can be treated as zero. From Eq.A-18, the quasi-static electric field [53] in z direction is:

$$E_z=-\left(\frac{e_{z3}}{\varepsilon_{zz}^s}\right)x_3 \qquad \text{Eq.A-24}$$

Form Eq.A-24 and Eq.A-21, the stress in z direction is:

$$X_3=(c_{33}+\frac{e_{z3}^2}{\varepsilon_{zz}^s})x_3 \qquad \text{Eq.A-25}$$

The constant $c_p=c_{33}+\frac{e_{z3}^2}{\varepsilon_{zz}^s}$ is the so-called piezoelectric stiffened stiffness. If Eq.A-25 is combined with Eq.A-15, the so-called piezoelectric stiffened wave equations for the stiffened longitudinal wave (v_z, X_3) are:

$$\frac{\partial X_3}{\partial z} = \rho \frac{\partial v_z}{\partial t} \qquad \text{Eq.A-26}$$

$$\frac{\partial v_z}{\partial z} = \frac{1}{c_p} \frac{\partial X_3}{\partial t} \qquad \text{Eq.A-27}$$

Eq.A-26 and Eq.A-27 describe a stiffened acoustic wave in $BaTiO_3$ single crystal without source. It can be rewritten as the wave equation:

$$\frac{\partial^2 v_z}{\partial z^2} - \frac{\rho}{c_p} \frac{\partial^2 v_z}{\partial t^2} = 0 \qquad \text{Eq.A-28}$$

The physical meaning of the equation above can be explained by piezoelectric theory as the stiffened effect [53]. It seems that this wave behaves as if the elastic stiffness c_{33} were increased to $c_p = c_{33} + \frac{e_{z3}^2}{\varepsilon_{z3}^s}$. The electric and acoustic coupling for this wave is the coupling of the quasi-static electric field and the acoustic longitudinal wave (v_z, X_3).

The coupling of longitudinal waves in PZT transducer is the same, if only the material constants in all the expressions above should be changed to material constants of PZT ceramics.

If there is a harmonic source electric field in z direction $\vec{E}_s = E_s \vec{a}_z$, the total electric field in z direction in the $BaTiO_3$ crystal studied can be written as:

$$E_{total} = E_z + E_s \qquad \text{Eq.A-29}$$

E_z is the coupled stiffened electric field in the crystal. Because only the harmonic stable state will be studied and the acoustic field (v_z, X_3) must satisfy the same stiffened condition, the coupled stiffened electric field in the crystal is the same as the field without source.

Form Eq.A-18 and Eq.A-21, the stress in the crystal with source:

$$X_3 = (c_{33} + \frac{e_{z3}^2}{\varepsilon_{z3}^s})\, x_3 - e_{z3} E_s \qquad \text{Eq.A-30}$$

in which the constant $c_p = c_{33} + \frac{e_{z3}^2}{\varepsilon_{z3}^s}$ is the piezoelectric stiffened stiffness.

Because of the source electric field E_s, the wave equations for acoustic longitudinal waves can be obtained in the same way:

$$\frac{\partial X_3}{\partial z} = \rho \frac{\partial v_z}{\partial t} \qquad \text{Eq.A-31}$$

$$\frac{\partial v_z}{\partial z} = \frac{1}{c_p}\frac{\partial X_3}{\partial t} + \frac{e_{z3}}{c_p}\frac{\partial E_s}{\partial t} \qquad \text{Eq.A-32}$$

Eq.A-31 and Eq.A-32 can also be written as the wave equation with source:

$$\frac{\partial^2 v_z}{\partial z^2} - \frac{\rho}{c_p}\frac{\partial^2 v_z}{\partial t^2} = \frac{e_{z3}}{c_p}\frac{\partial E_s}{\partial t} \qquad \text{Eq.A-33}$$

The same process can be applied to the other two coupled waves Eq.A-16 and Eq.A-17 in the crystal studied. The coupling equations are:

$$\frac{\partial^2 E_x}{\partial z^2} - \mu_0 \varepsilon_{xx}^s \frac{\partial^2 E_x}{\partial t^2} = \mu_0 e_{x5} \frac{\partial^2 v_x}{\partial t \partial z} \qquad \text{Eq.A-34}$$

$$\frac{\partial^2 E_y}{\partial z^2} - \mu_0 \varepsilon_{yy}^s \frac{\partial^2 E_y}{\partial t^2} = \mu_0 e_{x5} \frac{\partial^2 v_y}{\partial t \partial z} \; (\varepsilon_{yy}^s = \varepsilon_{xx}^s \text{ for BaTiO}_3) \qquad \text{Eq.A-35}$$

At the first sight, the coupling mechanism seems almost the same as the coupling discussed above. But a detailed discussion [53] shows that these kinds of coupling are much more complex than the stiffened electric and mechanic coupling. A detailed discussion is beyond the scope of the present work and some discussion can be found in other works [53, 54].

A2: Transmission line mode of acoustic waves in near-field

In near-field of piezoelectric materials, the electromagnetic and acoustic coupling phenomena are even more complicated than the coupling in the transducer, because the acoustic wave here is the piezoelectric acoustic wave with source electric field $\vec{E}_z = \vec{a}_z E_s$. Under the assumption described in Chapter 3, the acoustic transmission can be compared to the transmission of voltage waves in a transmission line with source [53].

If there are plane longitudinal harmonic acoustic waves (v_z^1, X_3^1) produced in the near-field in the crystal studied, the equations according to Eq.A-31 and Eq.A-32 are written as the followings:

$$\frac{\partial X_3^1}{\partial z} = \rho \frac{\partial v_z^1}{\partial t} \qquad \text{Eq.A-36}$$

$$\frac{\partial v_z^1}{\partial z} = \frac{1}{c_p}\frac{\partial X_3^1}{\partial t} + \frac{e_{z3}}{c_p}\frac{\partial E_s}{\partial t} \qquad \text{Eq.A-37}$$

Here, the suffix ‘1’ at the top right corner indicates the near-field area in the sample.

As a comparison, the equations of transmission line with sources V_s and I_s will be discussed:

$$\frac{\partial V(z,t)}{\partial z} = -L\frac{\partial I(z,t)}{\partial t} + V_s + RI(z,t) \qquad \text{Eq.A-38}$$

$$\frac{\partial I(z,t)}{\partial z} = -C\frac{\partial V(z,t)}{\partial t} + I_s + GV(z,t) \qquad \text{Eq.A-39}$$

Here $(V(z,t), I(z,t))$ is a solution of a voltage or current wave of a one-dimensional transmission line and has the form:

$$V(z,t) = V_m e^{j(\omega t - kz)} \qquad \text{Eq.A-40}$$

$$I(z,t) = I_m e^{j(\omega t - kz)} \qquad \text{Eq.A-41}$$

where V_m and I_m are amplitudes of the voltage and current wave which are decided by the source and boundary conditions.

In the case of a transmission line without loss, the equations can be written as:

$$\frac{\partial V(z,t)}{\partial z} = -L\frac{\partial I(z,t)}{\partial t} + V_s \qquad \text{Eq.A-42}$$

$$\frac{\partial I(z,t)}{\partial z} = -C\frac{\partial V(z,t)}{\partial t} + I_s \qquad \text{Eq.A-43}$$

If the one-dimensional transmission line with a source limited in the area $z_1 < z < z_2$, a general solution of the equations Eq.A-42 and Eq.A-43 above is:

$$V(z,t) = (a^+(z) + a^-(z))/2 \qquad \text{Eq.A-44}$$

$$I(z,t) = (a^+(z) - a^-(z))/2Z_0 \qquad \text{Eq.A-45}$$

$$a^+(z) = e^{-jkz}\int_{z_1}^{z}(V_s + Z_0 I_s)e^{jk\zeta}d\zeta + a^+(Z_1)e^{-jk(z-z_1)} \quad (z > z_1) \qquad \text{Eq.A-46}$$

$$a^-(z) = -e^{jkz}\int_{z}^{z_2}(V_s - Z_0 I_s)e^{-jk\zeta}d\zeta + a^-(Z_2)e^{jk(z-z_2)} \quad (z < z_2) \qquad \text{Eq.A-47}$$

where $R_T = \sqrt{\frac{L}{C}}$ is the characteristic resistance of voltage wave of transmission line.

By comparison of Eq.A-42 and Eq.A-43 with Eq.A-36 and Eq.A-37, if the following comparison is made:

$V(z,t) = -X_3$: the voltage wave is compared to negative stress in z direction of the longitudinal wave;

$I(z,t) = v_z$: the current wave is compared to velocity of the particle;

$L = \rho$: the inductance is compared to density of the sample;

$C = 1/c_p = 1/(c_{33} + e_{z3}^2/\varepsilon_{zz})$: the capacitance is compared to reciprocal of the stiffened elastic stiffness;

$I_s = \frac{e_{z3}}{c_p}\frac{\partial E_s}{\partial t}$: the current source is compared to the time differential of source electric field;

Eq.A-36 and Eq.A-37 will have the same solution as that of Eq.A-42 and Eq.A-43.

For the near-field system shown in Fig.5-1 with an electric field source in near-field, the stable harmonic solutions of the longitudinal wave in near-field can be written from above comparison as:

$$X_3^1 = -(a^{1+} + a^{1-})e^{j\omega t}/2 \qquad \text{Eq.A-48}$$

$$v_z^1 = (a^{1+} - a^{1-})e^{j\omega t}/2Z_0 \qquad \text{Eq.A-49}$$

$$a^{1+} = a_s^{1+}(z)e^{-jkz} + a^{1+}(0)e^{-jkz},$$

in which a_s^{1+} (z)= $\int_0^z (Z_0 \frac{e_{z3}}{c_p}\frac{\partial E_s}{\partial t})e^{jk\zeta}d\zeta$ $(0 \le z \le d)$ Eq.A-50

$$a^{1-} = a_s^{1-}(z)e^{jkz} + a^{1-}(d)e^{jk(z-d)},$$

in which a_s^{1-} (z)= $\int_z^d (Z_0 \frac{e_{e3}}{c_p}\frac{\partial E_s}{\partial t})e^{-jk\zeta}d\zeta$ $(0 \le z \le d)$ Eq.A-51

Here a_s^{1+} (z) and a_s^{1-} (z) are terms resulted from source in near-field. $Z_0 = \sqrt{\rho c_p}$ is the acoustic characteristic resistance of wave (v_z^1, X_3^1) in near-field and $a^{1+}(0)$ and $a^{1-}(d)$ are constants which can be determined by boundary conditions in Fig.5-1.

The acoustic waves outside the source area can be compared to the transmission line mode without source. The acoustic wave outside the near-field but still in the sample is governed only by the wave equations without source Eq.A-26 and Eq.A-27, and the solution can be written as (v^2, X_3^2):

$$X_3^2 = -(a^{2+} + a_2^{2-})e^{j\omega t}/2 \qquad \text{Eq.A-52}$$

$$v_z^2 = (a^{2+} - a^{2-})e^{j\omega t}/2Z_2 \qquad \text{Eq.A-53}$$

$$a^{2+} = a^{2+}(d)e^{-jk_2(z-d)}$$ Eq.A-54

$$a^{2-} = a^{2-}(d)e^{jk_2(z-d)}$$ Eq.A-55

Where $a^{2+}(d)$ and $a^{2-}(d)$ are constants which can be decided by the boundary condition of the system, ω the angular frequency, and k_2 acoustic longitudinal wave number in z direction in the sample outside the near-field. It is clear that the wave number and acoustic characteristic resistance inside and outside the near-field in the sample are the same, that is $k = k_2$ and $Z_0 = Z_2$. The suffix '2' at the top right corner indicates the area outside the near-field but still in the sample.

The final solution of the acoustic waves can be obtained by matching of boundary conditions in different areas. The acoustic boundary conditions for the typical system shown in Fig.3-1 are generally the same.

$X_3^1 = 0$ if z = 0; Eq.A-56

$X_3^2 = X_3^1$ if z = d; Eq.A-57

$v_z^2 = v_z^1$ if z = d; Eq.A-58

$X_3^3 = X_3^2$ if z = D_1 Eq.A-59

$v_z^3 = v_z^2$ if z = D_1 Eq.A-60

$a^{3-}(D_1) = Ra^{3+}(D_1)e^{-2jk_3D_2}$ if z = $D_1 + D_2$ Eq.A-61

here R is the acoustic reflect constant of the longitudinal wave at the interface between PZT transducer and the copper electrode. The backside of copper electrode is well matched acoustically so that there is no more reflection after the copper electrode.

Although the SNAM based on SPM technique has a constant force of the tip at z =0, for the discussion of harmonic solutions of acoustic waves, it plays no role for the harmonic solutions. At this base, a generally discussion of solutions of different scanning near-field acoustic microscopy systems is possible.

At boundary z=0, there is only one boundary condition Eq.A-56 for X_3^1,

$$a_s^{1+}(0) + a^{1+}(0) + a_s^{1-}(0) + a^{1-}(d)e^{-jkd} = 0$$

$$a_s^{1+}(0) = 0$$

$$a^{1+}(0) + a_s^{1-}(0) + a^{1-}(d)e^{-jkd} = 0$$ Eq.A-62

At the boundary z = d, there are boundary conditions Eq.A-57 and Eq.A-58 for both (v_z^1, X_3^1) and (v^2, X_3^2):

$$a_s^{1+}(d)e^{-jkd}+a^{1+}(0)e^{-jkd}+a_s^{1-}(d)e^{jkd}+a^{1-}(d)=a^{2+}(d)+a^{2-}(d)$$

$$a_s^{1-}(d)=0$$

$$a_s^{1+}(d)\ e^{-jkd}+a^{1+}(0)e^{-jkd}+a^{1-}(d)=a^{2+}(d)+a^{2-}(d) \qquad \text{Eq.A-63}$$

$$\frac{1}{Z_0}\{[a_s^{1+}(d)e^{-jkd}+a^{1+}(0)e^{-jkd}]-[a_s^{1-}(d)e^{jkd}+a^{1-}(d)]\}=\frac{1}{Z_0}\{a^{2+}(d)-a^{2-}(d)\}$$

$$a_s^{1+}(d)e^{-jkd}+a^{1+}(0)e^{-jkd}-a^{1-}(d)=a^{2+}(d)-a^{2-}(d) \qquad \text{Eq.A-64}$$

At boundary z=D_1, the boundary conditions Eq.A-59 and Eq.A-60 are

$$a^{3+}(D_1)\{1+Re^{-2jk_3D_2}\}=a^{2+}(d)e^{-jk(D_1-d)}+a^{2-}(d)e^{jk(D_1-d)} \qquad \text{Eq.A-65}$$

$$\frac{Z_0}{Z_3}a^{3+}(D_1)\{1-Re^{-2jk_3D_2}\}=a^{2+}(d)e^{-jk(D_1-d)}-a^{2-}(d)e^{jk(D_1-d)} \qquad \text{Eq.A-66}$$

If the source field in near-field is given, $a_s^{1+}(d)$ and $a_s^{1-}(0)$ are two source integration terms in near-field and are given from Eq.A-50 and Eq.A-51 respectively.

There are six constants $a^{1+}(0)$, $a^{1-}(d)$, $a^{2+}(d)$, $a^{2-}(d)$, $a^{3+}(D_1)$, and $a^{3-}(D_1)$. There are six independent linear equations from Eq.A-61 to Eq.A-66. There is only one single solution for all the constants. All the constants can be written as the functions of $a_s^{1+}(d)$ and $a_s^{1-}(0)$.

Let $\alpha_1=\frac{1-e^{-2jkD_1}}{1+e^{-2jkD_1}}$, $\alpha_2=\frac{1-\mathrm{Re}^{-2jk_3D_2}}{1+\mathrm{Re}^{-2jk_3D_2}}$, The final expression of $a^{3+}(D_1)$ can be calculated as the following:

From Eq.A-59: a_s^{1+} (z)=$\int_0^z(Z_0\frac{e_{z3}}{c_p}\frac{\partial E_s}{\partial t})e^{jk\zeta}d\zeta$ (0 ≤ z ≤ d),

we can get the expression of $a_s^{1+}(d)$:

$$a_s^{1+}(d)=\int_0^d(Z_0\frac{e_{z3}}{c_p}\frac{\partial E_s}{\partial t})e^{jk\zeta}d\zeta$$

From Eq.A-60, a_s^{1-} (z)=$\int_z^d (Z_0 \frac{e_{z3}}{c_p}\frac{\partial E_s}{\partial t})e^{-jk\zeta}d\zeta$ $(0 \le z \le d)$,

we can get the expression of $a_s^{1-}(0)$:

$$a_s^{1-}(0) = \int_0^d (Z_0 \frac{e_{z3}}{c_p}\frac{\partial E_s}{\partial t})e^{-jk\zeta}d\zeta .$$

If the source field is given, the term $a_s^{1+}(d)$ and $a_s^{1-}(0)$ are obtained.

From Eq.A-71, we can get the term $a^{1+}(0)$:

$$a^{1+}(0) = -[a_s^{1-}(0) + a^{1-}(d)e^{-jkd}]$$

If we add and subtract Eq.A-72 with Eq.A-73, we can get the term $a^{2+}(d)$ and $a^{2-}(d)$:

$$a^{2+}(d) = a_s^{1+}(d)\ e^{-jkd} + a^{1+}(0)e^{-jkd}$$

$$a^{2-}(d) = a^{1-}(d)$$

If we put the term $a^{1+}(0)$ into the term $a^{2+}(d)$ above, we get the following expression:

$$a^{2+}(d) + a^{2-}(d)\ e^{-2jkd} = [\ a_s^{1+}(d) - a_s^{1-}(0)\ ]\ e^{-jkd}$$

The term at the right side of the equation above is the source integration in near-field.

If we add and subtract Eq.A-74 with Eq.A-75, we can get the following expression:

$$a^{3+}(D_1)\ \{[1 + Re^{-2jk_3D_2}] + \beta_a\ [1 - Re^{-2jk_3D_2}]\} = 2\,a^{2+}(d)\ e^{-jk(D_1-d)}$$

$$a^{3+}(D_1)\ \{[1 + Re^{-2jk_3D_2}] - \beta_a\ [1 - Re^{-2jk_3D_2}]\} = 2\,a^{2-}(d)\ e^{jk(D_1-d)}$$

We can eliminate the $a^{2+}(d)$ and $a^{2-}(d)$ terms in the equations above and get the relationship between the term $a^{3+}(D_1)$ and the source term:

$$a^{3+}(D_1) = \frac{1}{(1+e^{-2jkD_1})(1+\mathrm{Re}^{-2jk_3D_2})}\ \frac{2[a_s^{1+}(d) - a_s^{1-}(0)]e^{-jkD_1}}{1+\alpha_1\alpha_2\beta_a}\ e^{-jkD_1}$$

Eq.A-67

Here $\alpha_1 = \frac{1-e^{-2jkD_1}}{1+e^{-2jkD_1}}$, $\alpha_2 = \frac{1-\mathrm{Re}^{-2jk_3D_2}}{1+\mathrm{Re}^{-2jk_3D_2}}$, and $\beta_a = \frac{Z_0}{Z_3} = \frac{Z_2}{Z_3}$.

Eq.A-67 can be simplified as the followings:

$$2[a_s^{1+}(d)-a_s^{1-}(0)]e^{-jkD_1}=4Z_0\frac{e_{z3}}{c_p}e^{-jkD_1}\int_0^d\frac{\partial E_s}{\partial t}\frac{e^{jk\zeta}-e^{-jk\zeta}}{2}d\zeta$$

$$=4\mathrm{j}\,Z_0\frac{e_{z3}}{c_p}e^{-jkD_1}\int_0^d\frac{\partial E_s}{\partial t}\frac{e^{jk\zeta}-e^{-jk\zeta}}{2j}d\zeta=4\mathrm{j}\,Z_0\frac{e_{z3}}{c_p}e^{-jkD_1}\int_0^d\frac{\partial E_s}{\partial t}\sin(k\zeta)d\zeta$$

$$a^{3+}(D_1)=\frac{1}{(1+e^{-2jkD_1})(1+\mathrm{R}e^{-2jk_3D_2})}\,\frac{4jZ_0\frac{e_{z3}}{c_p}\int_0^d\frac{\partial E_s}{\partial t}\sin(k\zeta)d\zeta}{1+\alpha_1\alpha_2\beta_a}$$

The output signal of the transducer under the open circuit condition is:

$$V_{output}=2(\frac{e_{z3}}{c_p})(\int_0^d\frac{\partial E_s}{\partial t}\sin(k\zeta)d\zeta)\left(\frac{e_{z3}^{PZT}}{\varepsilon_{zz}^{PZT}}\right)(\frac{1}{\omega})(\frac{1-e^{-jk_3D_2}}{1+e^{-2jkD_1}})(\frac{\beta_a e^{-jkD_1}}{1+\alpha_1\alpha_2\beta_a})$$

Eq.A-68

A3: Solution of SEAM

A3.1 The acoustic boundary condition of SEAM can be written as:

$X_3^1=0$ if z = 0; Eq.A-69

$X_3^2=X_3^1$ if z = d; Eq.A-70

$v_z^2=v_z^1$ if z = d; Eq.A-71

$X_3^3=X_3^2$ if z = D_1 Eq.A-72

$v_z^3=v_z^2$ if z = D_1 Eq.A-73

$a^{3-}(D_1)=Ra^{3+}(D_1)e^{-2jk_3D_2}$ if z = D_1+D_2 Eq.A-74

A3.2 The source electric field in the near-field of SEAM and output signal of transducer

The source electric field in the near-field of SEAM can be obtained by using the image charge and solving the Possion´s equation at the given electric boundary conditions in the sample. Based on the assumption in Chapter 4.1, the electric field under every scanning point can be written as [74]:

$E_s=A'(z-d)e^{j\omega t}$ (0 <z<d , $x^2+y^2\le a^2$)

$E_s=0$ (z >d and z<0, $x^2+y^2\ge a^2$) Eq.A-75

here $A'=\frac{(1-\eta_E)I_0}{\pi a^2\varepsilon_{zz}d}e^{-\tau_e}$

in which η_E is the backscattering constant, I_0 the beam current, τ_e the charge accumulation time, a is the radius of the primary electron beam.

$$\frac{e_{z3}}{c_p}\frac{\partial E_s}{\partial t} = A(z-d)\; e^{j\omega t}, \text{ and } A = j\omega\frac{e_{z3}}{c_p}A' = j\omega\frac{e_{z3}}{c_p}\frac{(1-\eta_E)I_0}{\pi a^2\varepsilon_{zz}d}e^{-\tau_e}$$

Eq.A-76

The source term in near-field of SEAM is:

$$\frac{e_{z3}}{c_p}\int_0^d \frac{\partial E_s}{\partial t}\sin(k\zeta)d\zeta = \mathrm{A}\frac{1}{k^2}[\sin(kd) - kd]$$

The output signal of PZT transducer under open circuit condition is:

$$V_{output} = 2\mathrm{A}\frac{1}{k^2}[\sin(kd)-kd]\left(\frac{e_{z3}^{PZT}}{\varepsilon_{zz}^{PZT}}\right)\left(\frac{1}{\omega}\right)\left(\frac{1-e^{-jk_3D_2}}{1+e^{-2jkD_1}}\right)\left(\frac{\beta_a}{1+\alpha_1\alpha_2\beta_a}\right)e^{-jkD_1}$$

$$= 2j\frac{e_{z3}}{c_p}\frac{(1-\eta_E)I_0}{\pi a^2\varepsilon_{zz}^{s}d}e^{-\tau_e}\frac{1}{k^2}[\sin(kd)-kd]\left(\frac{e_{z3}^{PZT}}{\varepsilon_{zz}^{PZT}}\right)\left(\frac{1-e^{-jk_3D_2}}{1+e^{-2jkD_1}}\right)\left(\frac{\beta_a}{1+\alpha_1\alpha_2\beta_a}\right)e^{-jkD_1}$$

$$= 2j\frac{e_{z3}}{\rho\varepsilon_{zz}^{s}}\frac{(1-\eta_E)I_0}{\pi a^2 d}e^{-\tau_e}\left(\frac{e_{z3}^{PZT}}{\varepsilon_{zz}^{PZT}}\right)\left(\frac{\sin(kd)-kd}{\omega^2}\right)\left(\frac{1-e^{-jk_3D_2}}{1+e^{-2jkD_1}}\right)\left(\frac{\beta_a e^{-jkD_1}}{1+\alpha_1\alpha_2\beta_a}\right)$$

Eq.A-77

in which ρ is the density of BaTiO3 material, $\alpha_1 = \frac{1-e^{-2jkD_1}}{1+e^{-2jkD_1}}$, $\alpha_2 = \frac{1-\mathrm{Re}^{-2jk_3D_2}}{1+\mathrm{Re}^{-2jk_3D_2}}$ and $\beta_a = \frac{Z_0}{Z_3}$.

A4: Solution of SNAM developed from SPM

A4.1 The acoustic boundary conditions of the system

The boundary conditions for SNAM developed in this work are almost the same as those of SEAM system. The only difference is at z=0 plane. The actual acoustic boundary conditions are:

$X_3^1 = F_{tip}$ if z = 0; Eq.A-78

$X_3^2 = X_3^1$ if z = d; Eq.A-79

$v_z^2 = v_z^1$ if z = d; Eq.A-80

$X_3^3 = X_3^2$ if z $= D_1$ Eq.A-81

$v_z^3 = v_z^2$ if z $= D_1$ Eq.A-82

$a^{3-}(D_1) = Ra^{3+}(D_1)e^{-2jk_3D_2}$ if z $= D_1 + D_2$ Eq.A-83

here R has the same meaning as that discussed before. The contact force F_{tip} is kept constant by the feedback control unit of SPM and has a typical value from several nN to several mN. It is actually a constant force which acted on the z =0 boundary of the near-field. For the harmonic solutions of near-field acoustics, it plays no role in the solution, as the time differential is zero.

A4.2 Green´s function of the model

The electric field distribution of the system can be obtained by solving the Poisson´s equation with a point charge under the given electric field boundary condition of the simplified model shown in Fig.5-1.

If the potential in the region -∞<z<0 is V0 and in the region 0<z<D_1 is V1, the electric field boundary condition can be written as:

At z = 0:

$$\mathrm{V0}=\mathrm{V1} \qquad \text{Eq.A-84}$$

$$\frac{\partial\,\mathrm{V0}}{\partial\,\mathrm{z}} = \frac{\partial\,\mathrm{V1}}{\partial\,\mathrm{z}} \qquad \text{Eq.A-85}$$

At z = D_1:

$$\mathrm{V1}=0 \qquad \text{Eq.A-86}$$

The field distribution of a point charge at (0,0,-h) in cylindrical coordinate system can be obtained as [80~82]:

$$\mathrm{V}=\frac{q}{4\pi\varepsilon_0}\int_0^\infty J_0(\beta r)e^{-\beta|z+h|}d\beta \qquad \text{Eq.A-87}$$

Here the $J_0(\beta r)$ is the Bessel´s function of zero order. β is the spatial periodical constant in z direction. The potential V is also called the Green´s function of a point charge in cylindrical coordinate system. The Green´s function for the simplified SNAM system can be written as:

In the region -∞<z<0;

$$\mathrm{V0}=\frac{q}{4\pi\varepsilon_0}\left[\int_0^\infty J_0(\beta r)e^{-\beta|z+h|}d\beta + \int_0^\infty A(\beta)J_0(\beta r)e^{\beta z}d\beta\right] \qquad \text{Eq.A-88}$$

In the region 0<z<D_1;

$$V1=\frac{q}{4\pi\varepsilon_0}\left[\int_0^\infty B(\beta)J_0(\beta r)e^{-\beta z}d\beta+\int_0^\infty C(\beta)J_0(\beta r)e^{\beta z}d\beta\right] \qquad \text{Eq.A-89}$$

In Eq.A-88 and Eq.A-89, $A(\beta)$, $B(\beta)$, and $C(\beta)$ are constants which are only dependent on the system geometry and variable β. These constants can be solved by the three independent equations from electric boundary conditions Eq.A-84, Eq.A-85, and Eq.A-86. The constants are solved in the following way.

According to Eq.A-84 and Eq.A-85:

At z =0:

$$e^{-\beta h}+A(\beta)=B(\beta)+C(\beta) \qquad \text{Eq.A-90}$$

$$-e^{-\beta h}+A(\beta)=[-B(\beta)+C(\beta)]\varepsilon_{r1} \qquad \text{Eq.A-91}$$

According to Eq.A-86, at z = D_1:

$$B(\beta)\ e^{-\beta D_1}+C(\beta)\ e^{\beta D_1}=0 \qquad \text{Eq.A-92}$$

If we let $\eta_1=\frac{(\varepsilon_{r1}-1)}{(\varepsilon_{r1}+1)}$, the constants $A(\beta)$, $B(\beta)$, and $C(\beta)$ can be obtained by solving Eq.A-90, Eq.A-91, and Eq.A-92. The constants are:

$$A(\beta)=-\eta_1\ e^{-\beta h}\ \frac{1}{1+\eta_1 e^{-2\beta D_1}}-e^{-\beta(2D_1+h)}\ \frac{1}{1+\eta_1 e^{-2\beta D_1}} \qquad \text{Eq.A-93}$$

$$B(\beta)=\frac{2e^{-\beta h}}{(\varepsilon_{r1}+1)}\ \frac{1}{1+\eta_1 e^{-2\beta D_1}} \qquad \text{Eq.A-94}$$

$$C(\beta)=-e^{-2\beta D_1}\ \frac{2e^{-\beta h}}{(\varepsilon_{r1}+1)}\ \frac{1}{1+\eta_1 e^{-2\beta D_1}} \qquad \text{Eq.A-95}$$

The Green functions for the system shown in Fig.5-1 are obtained according to Eq.A-88 and Eq.A-89 if all the constants are known.

To see the physical meanings of the Green´s function more clearly, we can discuss the Green´s function in the following way.

The Green´s function in region $-\infty<z<0$, according to Eq.A-88:

$$V0=\frac{q}{4\pi\varepsilon_0}\int_0^\infty J_0(\beta r)e^{-\beta|z+h|}d\beta+\frac{q}{4\pi\varepsilon_0}\int_0^\infty A(\beta)J_0(\beta r)e^{\beta z}d\beta$$

The first term of V0 is the potential of a point charge q at (0, 0, -h).

The second term of V0 is further composed of two terms:

The first part of $\frac{q}{4\pi\varepsilon_0}\int_0^\infty A(\beta)J_0(\beta r)e^{\beta z}d\beta$ is:

$$\frac{q}{4\pi\varepsilon_0}\int_0^\infty (-\eta_1)\, e^{-2\beta h}\,\frac{1}{1+\eta_1 e^{-2\beta D_1}}\,J_0(\beta r)e^{\beta z}d\beta$$

According Taylor series $\frac{1}{1\pm x}=1\mp x\mp x^2\mp x^3\mp ...,$ Eq.A-96

The term $\frac{1}{1+\eta_1 e^{-2\beta D_1}}$ can be expanded into Taylor series [88]:

$$\frac{1}{1+\eta_1 e^{-2\beta D_1}}=[1-\eta_1\, e^{-2\beta D_1}-(\eta_1\, e^{-2\beta D_1})^2-(\eta_1\, e^{-2\beta D_1})^3...] \tag{Eq.A-97}$$

Then, the first part of $\frac{q}{4\pi\varepsilon_0}\int_0^\infty A(\beta)J_0(\beta r)e^{\beta z}d\beta$ is:

$$\frac{q}{4\pi\varepsilon_0}\int_0^\infty (-\eta_1)\, e^{-2\beta h}\,\frac{1}{1+\eta_1 e^{-2\beta D_1}}\,J_0(\beta r)e^{\beta z}d\beta$$

$$=\frac{q}{4\pi\varepsilon_0}\int_0^\infty (-\eta_1)\,J_0(\beta r)\,e^{\beta(z-h)}d\beta+\frac{q}{4\pi\varepsilon_0}\int_0^\infty \eta_1^2\,J_0(\beta r)e^{\beta[z-(2D_1+h)]}d\beta$$

$$+\frac{q}{4\pi\varepsilon_0}\int_0^\infty (\eta_1^3\, e^{-\beta(4D_1+h)}+...)\,J_0(\beta r)e^{\beta z}d\beta \tag{Eq.A-98}$$

The terms at the right side of Eq.A-98 can be treated as image charges $Q_{m0}=-\eta_1$ q, $Q_{m1}=\eta_1^2$ q , ... at the position of (h, 2D$_1$+h, 4D$_1$+h,...) at z axis.

The second part of $\frac{q}{4\pi\varepsilon_0}\int_0^\infty A(\beta)J_0(\beta r)e^{\beta z}d\beta$ is:

$$\frac{q}{4\pi\varepsilon_0}\int_0^\infty (-1)\, e^{-\beta(2D_1+h)}\,\frac{1}{1+\eta_1 e^{-2\beta D_1}}\,J_0(\beta r)e^{\beta z}d\beta$$

According to Eq.A-97, it can be written as the following:

$$=\frac{q}{4\pi\varepsilon_0}\int_0^\infty (-1)\,J_0(\beta r)e^{\beta[z-(2D_1+h)]}d\beta+\frac{q}{4\pi\varepsilon_0}\int_0^\infty \eta_1\,J_0(\beta r)e^{\beta[z-(4D_1+h)]}d\beta$$

$$+\frac{q}{4\pi\varepsilon_0}\int_0^\infty [\eta_1^2\, e^{-\beta(6D_1+h)}+...]\,J_0(\beta r)e^{\beta z}d\beta \tag{Eq.A-99}$$

In the same way, terms at the right side of Eq.A-99 can be treated as the image charges Q_{n0} = -q, $Q_{n1} = \eta_1$ q ..., at the position of (2D$_1$+h, 4D$_1$+h,...) at z axis. The distribution of image charges for the Green´s function of V0 is shown in Fig.5-2.

The Green´s function V1 in the region 0<z<D$_1$ according to Eq.A-89 is:

$$\mathrm{V1} = \frac{q}{4\pi\varepsilon_0}\int_0^\infty B(\beta)J_0(\beta r)e^{-\beta z}d\beta + \frac{q}{4\pi\varepsilon_0}\int_0^\infty C(\beta)J_0(\beta r)e^{\beta z}d\beta$$

From Eq.A-97, the first term of V1 can be written as:

$$\frac{q}{4\pi\varepsilon_0}\int_0^\infty B(\beta)J_0(\beta r)e^{-\beta z}d\beta = \frac{q}{4\pi\varepsilon_0}\frac{2}{(\varepsilon_{r1}+1)}\int_0^\infty J_0(\beta r)e^{-\beta(z+h)}d\beta -$$

$$\frac{q}{4\pi\varepsilon_0}\frac{2}{(\varepsilon_{r1}+1)}\eta_1\int_0^\infty J_0(\beta r)e^{-\beta[z+(2D_1+h)]}d\beta -$$

$$\frac{q}{4\pi\varepsilon_0}\frac{2}{(\varepsilon_{r1}+1)}\int_0^\infty [e^{-2\beta h}\,(\eta_1\,e^{-2\beta D_1})^2\text{ -...}]\,J_0(\beta r)e^{-\beta z}d\beta \qquad \text{Eq.A-100}$$

The image charges are $Q_{i0} = \frac{2}{(\varepsilon_{r1}+1)}$q, $Q_{i1} = -\frac{2}{(\varepsilon_{r1}+1)}\eta_1$q, ... at the position of (-h, -(h+2D$_1$), ...) at z axis.

From Eq.A-97, the second term of V1 can be written as:

$$\frac{q}{4\pi\varepsilon_0}\int_0^\infty C(\beta)J_0(\beta r)e^{\beta z}d\beta = \frac{q}{4\pi\varepsilon_0}(-1)\frac{2}{(\varepsilon_{r1}+1)}\int_0^\infty J_0(\beta r)e^{\beta[z-(h+2D_1)]}d\beta +$$

$$\frac{q}{4\pi\varepsilon_0}\frac{2}{(\varepsilon_{r1}+1)}\eta_1\int_0^\infty J_0(\beta r)e^{\beta[z-(h+4D_1)}d\beta +$$

$$\frac{q}{4\pi\varepsilon_0}\int_0^\infty [e^{-\beta(h+2D_1)}(\eta_1\,e^{-2\beta D_1})^2\text{+...}]\,J_0(\beta r)e^{\beta z}d\beta \qquad \text{Eq.A-101}$$

The image charges are $Q_{j0} = -\frac{2}{(\varepsilon_{r1}+1)}$q, $Q_{j1} = \frac{2}{(\varepsilon_{r1}+1)}\eta_1$q, ... at the position of (2D$_1$+h, 4D$_1$+h, ...) at z axis. The distribution of image charges for the Green´s function of V1 is shown in Fig.5-3.

A5: Material constants of PZT and BaTiO$_3$

The elastic tensor of BaTiO$_3$ single crystal with a monodomain:

$$\overleftrightarrow{s}=\begin{pmatrix} s_{11} & s_{12} & s_{13} & 0 & 0 & 0 \\ s_{12} & s_{11} & s_{13} & 0 & 0 & 0 \\ s_{13} & s_{13} & s_{33} & 0 & 0 & 0 \\ 0 & 0 & 0 & s_{44} & 0 & 0 \\ 0 & 0 & 0 & 0 & s_{44} & 0 \\ 0 & 0 & 0 & 0 & 0 & s_{66} \end{pmatrix}$$

s_{11} = 8.05 x 10^{-12} m^2/N, s_{12} = -2.35 x 10^{-12} m^2/N, s_{13} = -5.24 x 10^{-12} m^2/N,

s_{33} = 15.7 x 10^{-12} m^2/N, s_{44} = 18.4 x 10^{-12} m^2/N, s_{66} = 8.84 x 10^{-12} m^2/N

$$\overleftrightarrow{c}=\begin{pmatrix} c_{11} & c_{12} & c_{13} & 0 & 0 & 0 \\ c_{12} & c_{11} & c_{13} & 0 & 0 & 0 \\ c_{13} & c_{13} & c_{33} & 0 & 0 & 0 \\ 0 & 0 & 0 & c_{44} & 0 & 0 \\ 0 & 0 & 0 & 0 & c_{55} & 0 \\ 0 & 0 & 0 & 0 & 0 & c_{66} \end{pmatrix}$$

c_{11} =27.5 x 10^{10} N/m^2, c_{12} =17.9 x 10^{10} N/m^2, c_{13} =15.1 x 10^{10} N/m^2

c_{33} =16.5 x 10^{10} N/m^2, $c_{44} = c_{55}$ =5.43 x 10^{10} N/m^2, c_{66} =11.3 x 10^{10} N/m^2

If only the elastic or piezoelectric properties of polarized $BaTiO_3$ ceramics are studied, the polarized $BaTiO_3$ ceramics can be described as material with 6mm crystal lattice and the elastic tensor is:

$$\overleftrightarrow{c}=\begin{pmatrix} c_{11} & c_{12} & c_{13} & 0 & 0 & 0 \\ c_{12} & c_{11} & c_{13} & 0 & 0 & 0 \\ c_{13} & c_{13} & c_{33} & 0 & 0 & 0 \\ 0 & 0 & 0 & c_{44} & 0 & 0 \\ 0 & 0 & 0 & 0 & c_{55} & 0 \\ 0 & 0 & 0 & 0 & 0 & c_{66} \end{pmatrix}$$

c_{11} =15.0x$10^{10}$$N/m^2$, c_{12} =6.6x$10^{10}$$N/m^2$, c_{13} =6.6x$10^{10}$$N/m^2$, c_{33} =14.6x$10^{10}$$N/m^2$,

c_{44} =4.4x$10^{10}$$N/m^2$

The elastic stiffness tensor of PZT ceramics has the same form as that of $BaTiO_3$ ceramics. The values of tensor components of PZT ceramics are:

c_{11} =12.6x$10^{10}$$N/m^2$, c_{12} =7.95x$10^{10}$$N/m^2$, c_{13} =8.41x$10^{10}$$N/m^2$, c_{33} =11.7x$10^{10}$$N/m^2$,

c_{44}=2.3x10^{10}N/m^2

The piezoelectric tensor of BaTiO$_3$ for both single crystal and ceramics

$$\vec{d} = \begin{pmatrix} 0 & 0 & 0 & 0 & d_{x5} & 0 \\ 0 & 0 & 0 & d_{x5} & 0 & 0 \\ d_{z1} & d_{z1} & d_{z3} & 0 & 0 & 0 \end{pmatrix}$$

d_{z1}= -34.5 x 10^{-12} C/N, d_{z3}= 85.6 x 10^{-12} C/N, d_{x5}= 392 x 10^{-12} C/N

$$\vec{e} = \begin{pmatrix} 0 & 0 & 0 & 0 & e_{x5} & 0 \\ 0 & 0 & 0 & e_{x5} & 0 & 0 \\ e_{z1} & e_{z1} & e_{z3} & 0 & 0 & 0 \end{pmatrix}$$

e_{z1}= -2.74 C/m^2, e_{z3}= 3.70 C/ m^2, e_{x5} = 21.3 C/ m^2

The piezoelectric tensor of PZT ceramics has the same form. The component values:

d_{z1}^{PZT} = -274 x 10^{-12} C/N, d_{z3}^{PZT} = 593 x 10^{-12} C/N, d_{x5}^{PZT} = 741 x 10^{-12} C/N

e_{z1}^{PTT} = -6.5 C/m^2, e_{z3}^{PTT} =9 C/ m^2, e_{x5}^{PTT} = 9.8 C/ m^2

The dielectric tensor of BaTiO$_3$ materials is:

$$\vec{\varepsilon}^{X} = \begin{pmatrix} \varepsilon_{xx}^{X} & 0 & 0 \\ 0 & \varepsilon_{xx}^{X} & 0 \\ 0 & 0 & \varepsilon_{zz}^{X} \end{pmatrix}, \ \varepsilon_{xx}^{X} = 2920\,\varepsilon_0, \ \varepsilon_{zz}^{X} = 168\,\varepsilon_0$$

here the X at the top right corner denotes the dielectric tensor under constant stress.

$$\vec{\varepsilon}^{x} = \begin{pmatrix} \varepsilon_{xx}^{x} & 0 & 0 \\ 0 & \varepsilon_{xx}^{x} & 0 \\ 0 & 0 & \varepsilon_{zz}^{x} \end{pmatrix},$$

Here the x at the top right corner denotes the dielectric tensor under constant strain.

The dielectric tensor of PZT ceramics has the same form as that of BaTiO$_3$ ceramics but different values of tensor components. The correspondent values are:

$\varepsilon_{xx}^{PZT,X}$ =3130 ε_0, $\varepsilon_{zz}^{PZT,X}$ =3400 ε_0

$\varepsilon_{xx}^{PZT,x}$ =1700 ε_0, $\varepsilon_{zz}^{PZT,x}$ =1470 ε_0

12 Reference

1. T. Mitsui, I. Tatsuzaki, E, Nakamura: An introduction to the physics of ferroelectrics. Gordon and Breach Science Publishers, Ltd. 1976
2. F. Jona: Ferroelectric Crystals, Pergamon Press 1992
3. M. E. Lines and A. M. Glass: Principles and applications of ferroelectrics and related materials. Oxford University Press 1996
4. C. Paz de Araujo, J. F. Scott, and G. W. Taylor, Ferroelectric thin films: synthesis and basic properties, Gordon and Breach Science Publishers, Ltd. 1996
5. D. Damjanovic: Ferro, dielectric, piezoelectric properties of ferroelectric thin films and ceramics, Rep. Prog. Phys. **61** (1998), 1267-1324
6. G. Arlt and P. Sasko: Domain configuration and equilibrium size of domains in $BaTiO_3$ ceramics, J. Appl. Phys. **51** (1980) No.9, 4956-4960
7. G. Arlt: The role of domain walls on the dielectric, elastic and piezoelectric properties of ferroelectrtic ceramics, Ferroelectrics **76** (1987), 451-358
8. G. Arlt: The influence of microstructure on the properties of ferroelectric ceramics, Ferroelectrics, **104** (1990), 217-227
9. G. Arlt: Twinning of ferroelectric and ferroelastic ceramics: stress relief, J. Mat. Sci. **25** (1990), 2655-2666
10. N. A. Pertsev and G. Arlt: Theory of the banded domain structure in coarse-grained ferroelectric ceramics, Ferroelectrics, **132** (1992), 27-40
11. Q. M. Zhang, H. Wang, N. Kim, and L. E. Cross: Direct evaluation of domain-wall and intrinsic contributions to the dielectric and piezoelectric response and their temperature dependence on lead zirconate-titanate ceramics, J. Appl. Phys. **75** (1994) No. 1, 454-459
12. M. Demartin, and D. Damjanovic: Dependence of the direct piezoelectric effect in coarse and fine grain batium titanate ceramics on dynamic and static pressure, Appl. Phys. Lett. **68** (1996) No. 21, 3046-3048
13. D. Damjanovic: Stress and frequency dependence of the direct piezoelectric effect in ferroelectric ceramics, J. Appl. Phys. **82** (1997), 1788-1797
14. G. Y. Robinson and R. M . White, Scanning electron microscopy of ferroelectric domains in Barium Titanate, Appl. Phys. Lett. **10** (1967), 320-323

---

15. N. Kultscher and L. J. Balk, Signal generation and contrast mechanisms in scanning electron acoustic microscopy, Scanning Electron Microscopy, **1**, (1986), 33-43

16. B. Y. Zhang, F. M. Jiang, Q. R. Yin, Electron acoustic microscopy of $BaTiO_3$ single crystal, J. Appl. Phys., **80**(3) (1996), 1916-1918

17. T. Malis and H. Gleiter, Investigation of the structure of ferroelectric domain boundaries by transmission electron microscopy, Journal of Applied Physics, **47**(12), (1976), 5195-5200

18. G. Binnig, C. F. Quate, and Ch. Gerber, Atomic Force Microscope, Physical Review Letters, **56**(9), (1986), 930-933

19. F. Saurenbach and B. D. Terris: Imaging of ferroelectric domain walls by force microscopy, Applied Physics Letters, **56**(17), (1990), 1703-1705

20. R. Lüthi, H. Haefke, K.-P. Meyer, E. Meyer, L. Howald, and H.-J. Güntherodt: Surface and domain structures of ferroelectric crystals studied with scanning force microscopy, Journal of Applied Physics, **74**(12), (1993), 7461-7471

21. M.-K. Bae, T. Horiuchi, K. Hara, Y. Ishibashi, and K. Matsushige: Direct observation of domain structures in Triglycine Sulfate by atomic force microscope, Jpn. J. Appl. Phys., **33**, (1994), 1390-1393

22. K. Franke, J. Besold, W. Haessler, and C. Seegebarth; Modification and detection of domains on ferroelectric PZT films by scanning force microscopy, Surface Science Letters, **302**, (1994), L283-L288

23. S.-I. Hamazaki, F. Shimizu, S. Kojima, and M. Takashige: AFM observation of 90° domains of $BaTiO_3$ butterfly crystals, Journal of the Physical Society of Japan, **64**(10), (1995), 3660-3663

24. L. M. Eng, M. Friedrich , J. Fouisek, and P. Günter: Deconvolution of topographic and ferroelectric contrast by noncontact and friction force microscopy, J. Vac. Sci. Technol. **B14**(2), (1996), 1191-1196

25. A. Gruverman, J. Hatano, and H. Tokumoto: Scanning force microscopy studies of domain structure in $BaTiO_3$ Single Crystal, Jpn. J. Appl. Phys., **36**, (1997), 2207-2211

26. S. Balakumar, J. B. Xu, J. X. Ma, S. Ganesamoorthy, and I. H. Wilson: Surface morphology of ferroelectric domains in $BaTiO_3$ Single Crystals: an atomic force microscope study, Jpn. J. Appl. Phys., **36**, (1997), 5566-5569

27. G. K. H. Pang and K. Z. Baba-Kishi: Characterization of butterfly single crystals of $BaTiO_3$ by atomic force, optical and scanning electron microscopy techniques: J. Phys. D: Appl. Phys., **31**, (1998), 2846-2853

28. S. Tsunekawa, T. Fukuda, T. Ozaki, Y. Yoneda, T. Okabe, and H. Terauchi: Study on ferroelectric domains in $BaTiO_3$ crystalline films and bulk crystals by atomic force and scanning electron microscopies, Journal of Applied Physics, **84**(2), (1998), 999-1002

29. S. V. Kalinin and D. A. Bonnell: Effect of phase transition on the surface potential of the $BaTiO_3$(100) surface by variable temperature scanning surface potential microscopy, Journal of Applied Physics, **87**(8), 2000

30. U. Rabe, S. Amelio, E. Kester, V. Scherer, S. Hirsekorn, and W. Arnold: Quantitative determination of contact stiffness using atomic force acoustic microscopy, Ultrasonics, **38**, (2000), 430-437

31. L. M. Eng, M. Bammerlin, Ch. Loppacher, M. Guggisberg, R, Bennewitz, R. Lüthi, E. Meyer, Th. Huser, H. Heinzelmann, and H.-J. Güntherodt: Ferroelectric domain characterisation and manipulation: a challenge for scanning probe microscopy, Ferroelectrics, **222**, (1999), 153-162

32. C. Harnagea, A. Pignolet, M. Alexe, K. M. Satyalakshmi, D. Hesse, and U. Gösele: Nanoscale switching and domain structure of ferroelectric $BaBi_4Ti_4O_{15}$ thin films, Jpn. J. Appl. Phys., **38**, (1999), L1251-L1257

33. C. Durkan, M.E. Welland, D. P. Chu, and P, Migliorato: Probing domains at the nanometer scale in piezoelectric thin films, Physical Review B, **60**(23), 1999, 16198-16204

34. B. Y. Zhang, X. X. Liu, Q. R. Yin, and L. J. Balk: Scanning near field acoustic microscopies for the evaluation of polycrystalline materials, Acoustical Imaging, **23**, (1997) 19-24

35. X. X. Liu, L. J. Balk, H.-P. Abicht, A. Eckau, and Q. R. Yin: Scanning acoustic microscopes for the investigation of ferroelectric properties of ferroelectric materials, Solid State Phenomena, **63-64**, (1998), 361-368

36. X. X. Liu and L. J. Balk: Scanning Acoustic Microscopes for the Investigation of Ferroelectrical Materials, presented at the "3rd Conference on Development and Technological Application of Scanning Probe Methods" (SXM3), (14.-17.9.1998, Basel,

Schweiz)

37. X. X. Liu, R. Heiderhoff, H.-P. Abicht, and L. J. Balk: Characterization of ferroelectric domains by the use of scanning near-field acoustic microscopies, Analytical Science, accepted for publication

38. X. X. Liu, B. Y. Zhang, Q. R. Yin, and L. J. Balk: Scanning electron acoustic microscopy for the evaluation of domain structures in BaTiO3 single crystal and ceramics, Journal of Material Science, **33** (1998) 4543-4549

39. J. F. Nye: Physical of crystals, Oxford University Press.

40. A. F. Devonshire, Theory of Barium Titanate - Part 1, Phil. Mag. **40** (1949) 1040-1063

41. V. A. Zhirnov: Sov. Phys. JETP **35** (1959), 1175-1180

42. E. V. Chenski: Sov. Phys.-Solid St. **14** (1973), 1940-1950

43. J. Bouillot and R. Machel: Proc. Europ. Mtg on Ferroelectricity, Saarbrücken, Wiss. Verlags, Stuttgart 1969, 111-119

44. J. C. Burfoot and G. W. Taylor: Polar dielectrics and their applications, 1979 Macmillan Press Ltd.

45. V. Holy U. Pietsch, and T. Baumbach: High resolution X-ray scattering from thin films and multilayers, Springer Verlag, 1999

46. B. M. Park, S. J. Chung, H. S. Kim, W. Si, and M. Dudley, Synchrotron white-beam X-ray topography of ferroelectric domains in a $BaTiO_3$ single crystal, Philosophical Magzine A, **75** (3), 1997, 611-620

47. C. L. Jia, K. Urban, M. Mertin, S. Hoffmann, and R. Wasser, The structure and formation of nanotwins in $BaTiO_3$ thin films, Philosophical Magazine A, **77**(4) (1998), 923-939

48. I. T. Kim, J. W. Jang, H. J. Youn, C. H. Kim, and K. S. Hong, 180° ferroelectric domains in polycrystalline $BaTiO_3$ thin films, Appl. Phys. Lett. **72**(3) (1998), 308-310

49. R. C. Miller: Optical Harmonic Generation in Single Crystal BaTiO[sub3], Phys. Rev. **134** (1964), A1313-A1318

50. M. Flörsheimer, R. Paschotta, U. Kubitscheck, Ch. Brillert, D. Hofmann, L. Heuer, G. Schreiber, C. Verbeek, W. Sohler, and H. Fucks: Second-harmonic imaging of ferroelectric domains in $LiNbO_3$ with micron resolution in lateral and axial directions, Appl. Phys. B **67** (1998) 593-599

51. I. I. Smolyaninov and C.C. Davis: Near-field optical study of photorefractive surface waves in $BaTiO_3$, Optics Letters, **24** No.19, (1999), 13671369

52. S. N. Zhu and W. Cao, Imaging of ferroelectric domains in $LiTiO_3$ by environment scanning electron microscopy, Ferroelectrics, **222** (1999), 257-262

53. B. A. Auld: Acoustic fields and waves in solids, John Wiley & Sons, Inc. 1973

54. S. W. Meeks and B. A. Auld: Optical and acoustic device applications of ferroelastic crystals, Advances in electronics and electron physics, **71** (1998) 250-355

55. E. Brandis and A. Rosencwaig, Thermal-wave microscopy with electron beams, Applied Physics Letters, **37**, (1980), 98-100

56. G. S. Cargill, Nature, **286**, (1980), 691-695

57. L. J. Balk: Advances in Electronics and Electronic Physics, **71**, (1988) 1-73

58. J. Cantrell and M. Qian, Piezoelectric detection of signals in scanning electron acoustic microscopy, Materials Science and Engineering, **A122** (1989) 47-52

59. L. J. Balk: Scanning Acoustic Microscopy, Analysis of Microelectronic Materials and Devices, Ed. by M. Grasserbauer and H. W. Werner, John Wiley & Sons Ltd. (1991) 742-769

60. B. Y. Zhang and Q. R. Yin: Piezoelectric coupling effect of ferroelectrics in scanning electron acoustic imaging, Progress in natural science **6**(supplement), 1996, S-123~S-126

61. S. W. Fu, S. Y. Zhang, Z.S. Wu, L. B. Luo, Z. Zhang, and H. I Chen, Photoacoustic investigation of chemical reactions by piezoelectric cylindrical tube transducer, Progress in natural science **6**(supplement), 1996, S-54~S-57

62. F. G. Satkiewicz, J. C. Murphy and L. C. Aamodt: in Techical digest of the Fourth International Topical Meeting on Photoacoustic, Thermal, and Related Science (Montreal, 1985)

63. D. N. Rose, H. R. Turner, K. Legg: in Techical digest of the Fourth International Topical Meeting on Photoacoustic, Thermal, and Related Science (Montreal, 1985)

64. P. Günther, U. Ch. Fischer, and K. Dransfeld: Scanning near-field acoustic microscopy, Applied Physics, **B48**, (1989), 89-92

65. U. Rabe and W. Arnold: Acoustic Microscopy by atomic force microscopy, Applied Physics Letters, **64**(12), (1994), 1493-1495

66. M. Maywald, G. Brockt, and L. J. Balk: Scanning Probe Acoustic Microscopy, Inst. of Phys. Conf. Ser. No. 146 (1995) 667-670

67. U. Grunewald, K. Bartzke, T. Antrack, Application of the needle sensor for microstructure measurements and atomic force microscopy, Thin Solid Films, **264**, (1995), 169-171

68. A. Michels, F. Meinen, T. Murdfield, W. Göhde, U. C. Fischer, E. Beckmann, and H. Fuchs: 1 MHz quartz length extension resonator as a probe for scanning near-field acoustic microscopy, Thin Solid Films, **264**, (1995), 172-175

69. T. Hesjedal, E. Chilla, and H. J. Fröhlich: Scanning acoustic force microscope investigations of surface acoustic waves, Surface and Interface Analysis, **25**, (1997), 569-572

70. R. M. Cramer, V. Biletzki, P. Lepidis, L. J. Balk: Subsurface analyses of defects in integrated devices by scanning probe acoustic microscopy, Microelectronics Reliability **39** (1999) 947-950

71. F. Ohuchi, D. E. Clark, L. L. Hench: Effect of crystallization on the Auger electron signal decay in an Li2Ox 2 SiO2 glass and glass-ceramic, J. Am. Ceram. Soc., **62** (1979), 500-503

72. F. Ohuchi and P. H. Holloway. General model of sodium desorption and diffusion during electron bombardment of glass. Journal of Vacuum Science and Technology, **20** (1982), 863-867

73. L. Reimer: Scanning Electron Microscopy, Springe-Verlag, 1985

74. J. Cazaux: Some considerations on the electric field induced in insulators by electron bombardment, Journal of Applied Physics, **59**(5), 1986, 1418-1430

75. S. G. Qian, S. Y. Zhang, J. C. Cheng, and Z. Q. Wang, Three dimensional theory of scanning electron-acoustic imaging, **6**(supplement), 1996, S-127~S-130

76. Valvo: Piezooxide (PXE), Photo Copie Gmbh, Hamburg, (1984)

77. C. Durkan and M. E. Welland: Investigations into local ferroelectric properties by atomic force microscopy, Ultramicroscopy, **82**, (2000), 141-148

78. C. H. Ahn, T. Tybell, L. Antognazza, K. Char, R. H. Hammond, M. R. Beasley, Ø. Fischer, and J.-M. Triscone: Local, nonvolatile electronic writing of epitaxial Pb(Zr0.52Ti0.48)O3/SrRuO3 heterostructures, Science **276**, (1997), 1100-1103

79. S. Belaidi, P. Girard, and G. Leveque: Electrostatic forces acting on the tip in atomic force microscopy: Modulization and comparison with analytic expressions, Journal of applied Physics, **81**(3), 1997, 1023-1030

80. J. A. Stratton: Electromagnetic theory, McGraw-Hill Book company, Inc. 1941

81. W. R. Smythe: Static and dynamic electricity, McGraw-Hill Book company, Inc. 1968

82. V. W. Hansen: Numerical solution of antennas in layered media, John Wiley & Sons Inc. 1989

83. Nanosensors Dr. Olaf Wolter GmbH, Wetzlar-Blankenfeld, Germany

84. S. Hirsekorn, U. Rabe, and W. Arnold: Theoretical description of the transfer of vibration from a sample to the cantilever of an atomic force microscope, Nanotechnology, **8** (1997), 57-66

85. U. Rabe, S. A. Melio, E. Kester, V. Scherer, S. Hirsekorn, W. Arnold: Quantitative determination of contact stiffness using atomic force acoustic microscopy, Ultrasonic **38** (2000), 430-437

86. H. T. Langhammer, T. Müller, A. Polity, K.-H. Felgner, and H.-P. Abicht: On the crystal and defect structure of Manganese-doped barium titanate ceramics, Materials Letters, **26**, 1996, 205-210

87. National technology roadmap for semiconductors, Austin: SEMATECH Inc. 1997

88. I. N. Bronstein and K. A. Semendjajew: Taschenbuch der Mathematik, 1991

89. Q. R. Yin, J. Liao, B. Y. Zhang, Y. Yang, and F. M .Jiang, Electron acoustic imaging of ferroelectric domain and mechanism analysis on $BaTiO_3$ ceramics, Ferroelectrics **231** (1999), 11-18

Publications and presentations

Parts of this work have been published in international journals or presented at the international conference, scientific seminars, and invited scientific talks. The following is a list of the publications and presentations of the author in recent years.

1. B. Y. Zhang, X. X. Liu, Q. R. Yin, and L. J. Balk,: Scanning near field acoustic microscopies for the evaluation of polycrystalline materials, Acoustical Imaging, **23**, (1997) 19-24
2. X. X. Liu, L. J. Balk, H.-P. Abicht, A. Eckau, and Q. R. Yin: Scanning acoustic microscopes for the investigation of ferroelectric properties of ferroelectric materials, Solid State Phenomena, **63-64**, (1998), 361-368
3. X. X. Liu, B. Y. Zhang, Q. R. Yin, and L. J. Balk: Scanning electron acoustic microscopy for the evaluation of domain structures in BaTiO3 single crystal and ceramics, Journal of Material Science, **33** (1998) 4543-4549
4. X. X. Liu, R. Heiderhoff, H.-P. Abicht, and L. J. Balk: Characterization of ferroelectric domains by the use of scanning near-field acoustic microscopies, Analytical Science, Vol.17, Special Issue No.107 2001
5. X. X. Liu, R. Heiderhoff, H.-P. Abicht, and L. J. Balk: "Dynamic characterization of ferroelectric domains of $BaTiO_3$ by the use of scanning near-field acoustic microscopy", accepted for presentation at "International Conference on Materials for Advanced Technologies" (ICMAT 2001, 1.-6.7.2001, Singapore), to be published in Materials Chemistry and Physics

Presentations

6. L. J. Balk, G. Fiege, and X. X. Liu: Imaging of Thermal and Mechanical Structures by Scanning Force Microscopy, Invited Talk at "SPMM'97, International Conference on Scanning Probe Microscopy as a Microsystem" (5.-7.6.1997, Wroclaw, Poland)
7. X. X. Liu and L. J. Balk: Scanning acoustic microscopes for the investigation of ferroelectric material, presented at "3rd Conference on Development and Technological Application of Scanning Probe Methods (SXM3)", from Sep. 14 to 17, 1998.
8. X. X. Liu: Characterization of ferroelectric domains by the use of scanning near-field acoustic microscopy, Presented on Jan. 17, 2000, in Fachbereich Elektrotechnik und Informationstechnik, BUGH Wuppertal

9. X. X. Liu: Characterization of ferroelectric domains by the use of scanning near-field acoustic microscopy, Presented on Feb. 4, 2000, in Fachbereich Physik, Martin-Luther-Universität Halle-Wittenberg
10. X. X. Liu: Characterization of ferroelectric domains by the use of scanning near-field acoustic microscopy, Presented on Feb. 5, 2000, in Bundesanstalt für Materialsforschung und –Prüfung, Berlin
11. X. X. Liu: Characterization of ferroelectric domains by the use of scanning near-field acoustic microscopy, Presented on Jul. 15, 2000, in Department of Electrical Engineering and Information, National University of Singapore
12. X. X. Liu: Characterization of ferroelectric domains by the use of scanning near-field acoustic microscopy, Presented on Jul. 21, 2000, in Shanghai Institute of Ceramics, Chinese Academy of Science